REPUBLIQUE ALGERIENNE DEMOCRATIQUE ET POPULAIRE

MINISTERE DE L'ENSEIGNEMENT SUPERIEUR ET DE LA RECHERCHE SCIENTIFIQUE

UNIVERSITE FRERES MENTOURI – CONSTANTINE 1

FACULTE DES SCIENCES EXACTES

DEPARTEMENT DE PHYSIQUE

THESE

Pour l'obtention du diplôme de

DOCTORAT en SCIENCES

OPTION

SEMI-CONDUCTEUR

par

Abdelhakim MEZIANI

Soutenue le :   18 / 12 / 2018

THEME

Electronic and Structural Properties of $Al_{1-x}In_xN$ with Application to an Electronic Device

Devant le jury:

Président: Amor DJEMEL   Prof.   Université Frères Mentouri, Constantine 1

Rapporteur: Azzedine TELIA   Prof.   Université Frères Mentouri, Constantine 1

Examinateurs: Zineddine OUILI   Prof.   Université Frères Mentouri, Constantine 1

Nadir BOUARISSA   Prof.   Université Badji Mokhtar, Msila

Ramdane MAHAMDI   Prof.   Université Moustafa Ben Boulaid Batna 2

Mourad. ZAABAT   Prof.   Université Larbi Ben Mhidi, Oum El Bouagui

ACKNOWLEDGEMENTS

Chapter 4 STRAIN EFFECTS AND APPLICATION TO AN ELECTRONIC DEVICE

LIST OF FIGURES

LIST OF TABLES

LIST OF ABBREVIATIONS

AE: All electron.

BM: Bulk modulus.

CB: Conduction band.

DFT: Density functional theory.

DOS: Density of states

GGA: General gradient approximation.

HEMT: High electron mobility transistor.

LAPW: Linearized Augmented Plane-Wave Method.

LCAO: Linear combination of atomic orbitals.

LDA: Local density approximation.

mBJLDA: modified Beck Johnson local density approximation

MTS: Muffin Tin Sphere.

VASP: Vienna ab-initio simulation package

NN: Nearest neighbors

PAW: Projector-augmented-wave.

PP: Pseudopotential.

PW: Plane wave.

RMT: Radius of Muffin Tin.

Rs: Rocksalt.

SQS: Special quasi-random structure.

TBM: Tight binding model.

Wz: Wurtzite.

XC: exchange-correlation.

Zb: Zincblende.

2DEG: Two-dimensional electron gas.

2DHG: Two dimensional hole gas.

INTRODUCTION

Introduction

Group III nitrides, InN, GaN, AlN, and their alloys, have revolutionized solid state lighting since the development of a commercial blue light emitting diode based on GaN by Nakamura **[1]** and continue to attract substantial research interest due to their unique properties and importance for optoelectronics and electronics.

Group-III nitrides consist of the compounds of nitrogen (N) and the elements in the column13 p-block of the periodic table namely boron (B), aluminium (Al), gallium (Ga), indium (In) and thallium (Tl). Amongst these compounds GaN, InN, AlN and their alloys the ternaries InGaN, AlGaN and AlInN, and the quaternary AlInGaN have been the subject of intensive research for the device scientists and engineers in recent years due to their potential application for electronic and optoelectronic devices fabrication **[2]**. The fundamental band gaps of III-nitride ternaries cover various light spectra over the entire composition and easily tailored lattice parameters allows the fabrication of electronic and optical devices on suitable lattice matched substrates. They present, compared to other III-V compounds, strong chemical bonds and high resistance to degradation from intense illumination and high currents. Among these semiconductor structures ternary $Al_{1-x}In_xN$ alloy has a band gap that covers a very wide energy range (0.69 eV to 6.25eV), which makes it an ideal candidate to fabricate electronic and optoelectronic devices such as high-power high-frequency field-effect transistors, blue and ultraviolet light emitting and laser diodes, resonant-cavity light emitting diodes, surface-emitting lasers, and solar blind ultraviolet photodetectors **[3,4]**.

Utilization of the group III-nitride ternary alloys such as $Al_{1-x}In_xN$ in the fabrication of electronic and optical device applications requires a better controlling of the growth and fabrication process conditions as well as a reliable and precise physical modeling of their structural, electronic and optical properties as a function of the alloy composition. It is now well known that the better controlling of the growth conditions by molecular beam epitaxy (MBE) and metal organic chemical vapor deposition (MOCVD) techniques allows precise tailoring of the dimensions and the material properties of group III-nitride semiconductor systems.
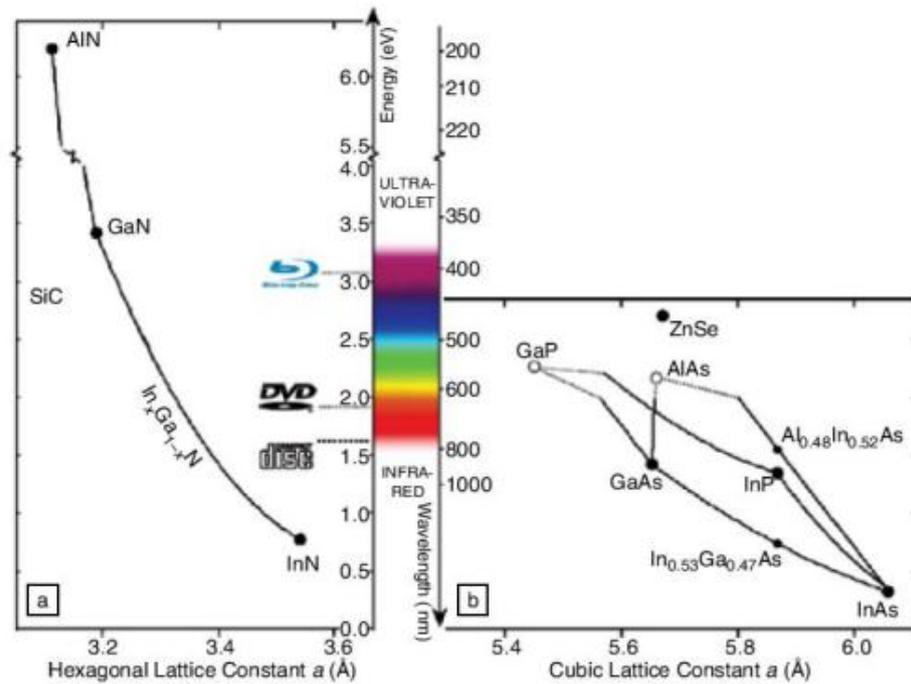
Figure 1 Band gaps vs. structural parameters of III-V wurtzitic nitrides (left). Color range of emitted light (middle). Relationship between band gap and structure parameters on some material used in LED (right) **[5].**

It is a fact that, at normal growth conditions, AlN and InN crystallize in hexagonal wurtzite structure (B4 phase), whereas growth of zincblende structure (B3 phase) on cubic substrates has also been achieved among reports of interesting physical properties for electronic devices that this phase may present **[6]**. In addition to that, thin layer film of zincblende structure has been achieved in a non polar growth **[7]**. On the other hand, high pressure experiments and *ab-initio* calculations showed that rocksalt (B1 phase) can also be obtained **[8,9]**. The perspective of the possibility of realization of three phases has led us to perform a comparative study of structural and electronic properties of the various phases of the ternary alloys $Al_{1-x}In_xN$ as well as high pressure effects on some of the undertaken physical properties. This study used as computational methods the density functional theory with modified Becke-Johnson functional based (mBJLDA) **[10,11]** and the semi-empirical sps^* tight binding theory with nearest neighbor interactions. By means of these two methods we investigated the composition effect on the structural and electronic properties of $Al_{1-x}In_xN$ ternary alloy in the zincblende, wurtzite and rocksalt phases. In the beginning, the lattice

parameters were computed at various In proportions taking into account alloy randomness by using special quasi-random structure, then from the obtained results bulk modulus, energy band gaps, density of states and the electron effective mass were derived. The physical properties variation with In content within each phase is first examined, then a phase comparison is carried out.

Over the last few years, study of materials under high pressure has become an extremely important subject exhibiting high growth. This is primarily due to both theoretical and experimental developments which have at last facilitated such work. The effects of pressure are more easily incorporated into first-principles simulations since it affords the possibility of studying the variation in the properties of solids as interatomic distances are changed in a systematic way.

In the high pressure effects, we first study the relative stability of the wurtzite and zincblende phases of the $Al_{1-x}In_xN$ alloy, then wurtzite-rocksalt and zincblende-rocksalt phase transition pressures throughout the whole indium composition range.

Finally, since varying gaps by means of pressure variation is another way of tailoring gaps and providing a wider spectrum for optoelectronic devices, we then examine the variation of the band gap with pressure for both phases.

The architecture of electronic or optical devices requires heterostructure stacking of different compounds with various lattice parameter constants creating hence strains on the thin films. This has an immediate effect on the structural properties on the strained alloy and therefore on its electronic and optical properties. In the case of AlInN based devices, binary GaN is often chosen as a buffer resulting in a biaxial strain on the alloy with an immediate modification of the lattice parameters resulting in a whole new physical parameters (band gaps, effective masses...) for the AlInN/GaN heterostructure.

To end with, previously studied phenomena are applied to a practical device namely the HEMT. As will be seen later many of its transport parameters depend greatly on the density n of a two dimensional electron gas (2DEG) created at the edge of the heterostructure. The purpose of the last section is to study the variation of the density with the strain.

The work in this thesis has been structured as follows:

- Chapter 1: The structural properties of wurtzite, zincblende and rocksalt are reviewed.

- Chapter 2: We describe the theoretical methods used in this thesis. The physical formalism of the tight binding method and density functional theory are presented.

- Chapter 3: The structural and electronic properties parameters for a bulk AlInN .are computed. Lattice parameters, band gap, electron effective masses and density of states are calculated for zincblende and wurtzite phases and results are analyzed and compared between phases and with experimental data. High pressure effects on the alloy are studied. The stability of the various phases, the phase transition pressures and the pressure variation gap are all examined.

- Chapter 4: Its first part deals with the effects of the strain. Electronic and structural properties of the strained AlInN in the heterostructure AlInN/GaN are revisited. The then obtained results are applied to a high electron mobility transistor (HEMT) by deriving the density of the two-dimensional electron gas and the variation of its resistance.

- Appendices A and B providing respectively the tight binding hamiltonians and matrices parameters for the zincblende and wurtzite structures.

- Appendix C: The elastic theory is reviewed briefly and the nitrides elastic constants are provided.

CHAPTER 1

CRYSTALLINE STRUCTURES OF III-N NITRIDES

1.1 Nitrides basic structures

III-nitride semiconductors AlN, GaN, InN and their alloys can crystallize in three structures: the hexagonal wurtzite phase (B4), the cubic zincblende phase (B3) and the rocksalt phase (B1). The thermodynamically stable phase at room temperature is the wurtzite phase, but also nitride epitaxial growth with zincblende structure can be achieved on (001)-oriented cubic substrates. Finally, the rocksalt structure can be induced in III-nitrides at high pressures. In the following sections we will try to give a brief reminder of the structures previously mentioned.

1.2 The zincblende structure:
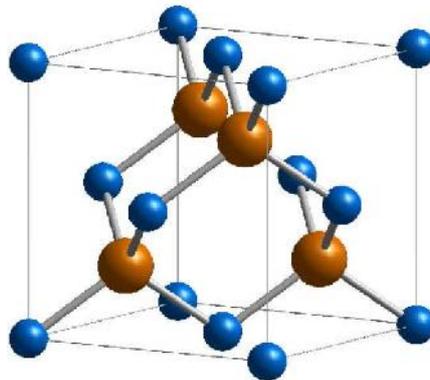
Figure 1.1 Zincblende unit cell

The zincblende structure (**Figure 1.1**) has a face-centered cubic (fcc) lattice with a diatomic basis. where the anion A is at (0, 0, 0) and the cation C is at (1, 1, 1)a/4 relative to the lattice point. Anion and cation atoms are tetrahedrally arranged with each anion bonded to four cations and vice versa and their respective sublattices shifted with respect to each other by a quarter of the diagonal of the fcc lattice. The close-packed layers adopt regular repeating arrangements: ABCABC along the (111) direction.

The primitive cell is formed by one cation and one anion, and the primitive translation vectors are:

$$\mathbf{a}=\frac{1}{2}a(0,1,1), \ \mathbf{b}=\frac{1}{2}a(1,0,1), \ \mathbf{c}=\frac{1}{2}c(1,1,0) \qquad (1.1)$$

where a is the lattice constant. The unit cell positions are:

$$R_1 = 0, \quad R_2 = \frac{1}{2}a + \frac{1}{2}b + \frac{1}{2}c$$

The B3 system belongs to the F-43m (No. 216) space group. The first Brillouin zone for the cubic face centered lattice with the main symmetry direction is represented in **Figure (1.2)** where the symmetry points have the following coordinates:

X(1,0,0), L(1,1,1), K(3/4,3/4,0), W(1,1/2,0).
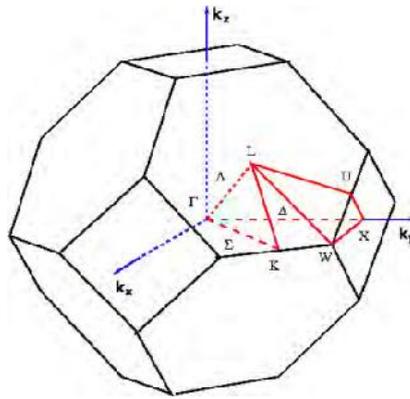
Figure 1.2 First Brillouin zone for the cubic face centered lattice.

1.3 The wurzite structure

The wurtzite structure can be described by considering two interpenetrating hexagonally close packed (hcp) sublattices shifted along the c axis. We thus have an hcp lattice with a diatomic basis. In addition, the wurtzite structure is characterized by an internal parameter u, defined so as the anion-cation bond length along the (0001) axis is cu.
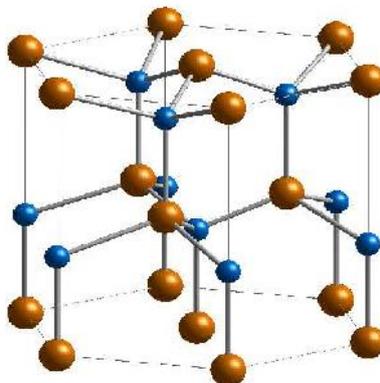
Figure 1.3 Wurtzite unit cell

The wurtzite unit cell is shown in **figure 1.3**. The corresponding lattice vectors are

$$\mathbf{a}=a(1,0,0), \mathbf{b}=a(1, \sqrt{3},0)/2, \mathbf{c}=c(0,0,1) \qquad (1.2)$$

and the unit cell positions are:

$$\mathbf{R_1}=0, \ \mathbf{R_2}=u\mathbf{c}, \ \mathbf{R_3}=\frac{1}{3}\mathbf{a}+\frac{1}{3}\mathbf{b}+\frac{1}{2}\mathbf{c}, \ \mathbf{R_4}=\frac{1}{3}\mathbf{a}+\frac{1}{3}\mathbf{b}+(u+\frac{1}{2})\mathbf{c}$$

The first Brillouin zone for the cubic face centered lattice with the main symmetry direction is represented in **Figure (1.4)** and the symmetry points have the following coordinates:

K(1/3,1/3,0), M(1/2,0,0), A(0,0,1/2), H(1/3,1/3,1/2), L(1/2,0,1/2).
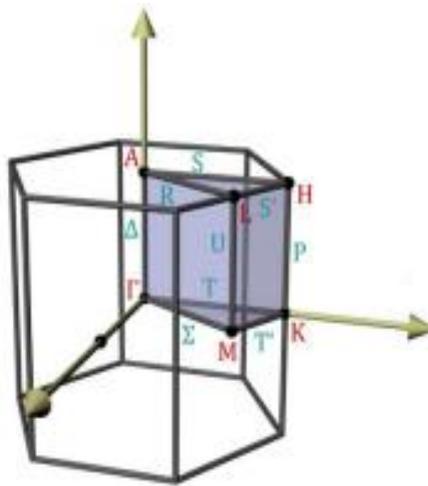
Figure 1.4 First Brillouin zone for the hexagonal lattice.

Wurtzite has the symmetry of P63 mc (space group 186) with both N and Al at Wyckoff position but with different z values. Wurtzite conventional unit cell, shown in **Figure 1.3**, contains four atoms The lattice parameters a and b are the length of the sides as shown, while the lattice parameter c is the height of the unit cell.

The ideal wurtzite structure (all bond lengths and angles as in ZB) corresponds to $a_w = {a_{zb}}/{\sqrt{2}}$; $c_w = \frac{2a_{zb}}{3}$; $\frac{c_1}{a} = \frac{8}{3}$; u=3/8 (whereas it deviates from this value for real wurtzite crystals). Since zincblende and wurtzite may have almost identical bond lengths, i.e. nearest neighbors (NN) distances, and bond angles, differing only in coordination of next-nearest neighbors (NNN), their total energies are usually very close, so that these phases are strongly competitive.

In the case of wurtzite the stacking arrangement, along the (0001) direction, as shown in **figure 1.5** is of the type ABAB.
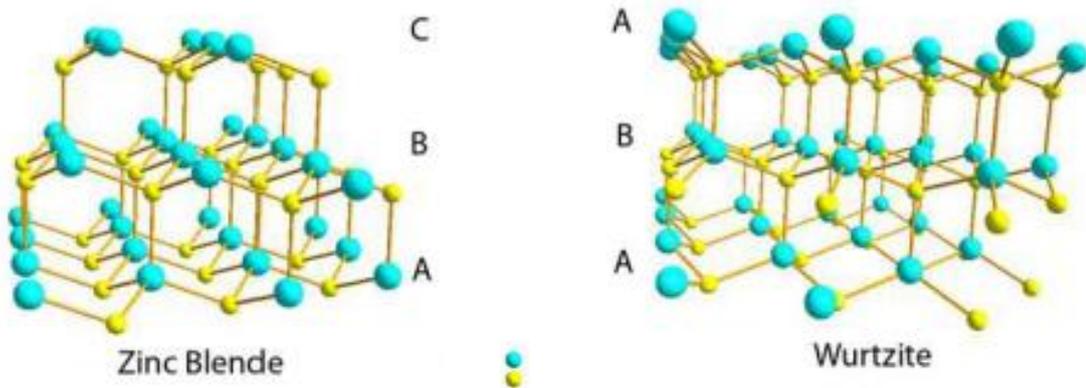
Figure 1.5 Zincblende and Wurtzite crystal structures. Shown are the ABCABC cubic close pack layer ordering and ABABAB hexagonal close pack layer ordering.

1.4 The rocksalt structure:

The rocksalt structure (**Figure 1.6**) has face centre cubic lattice with two basis: one at position **(0, 0, 0)** and the second at position **(1/2, 1/2, 1/2)a** where a is the lattice parameter.

The rocksalt structure contains equal amounts aluminium and nitrogen. Rocksalt has the symmetry of Fm-3m (space group 225). The smallest unit cell possible for the rocksalt structure contains only two atoms.
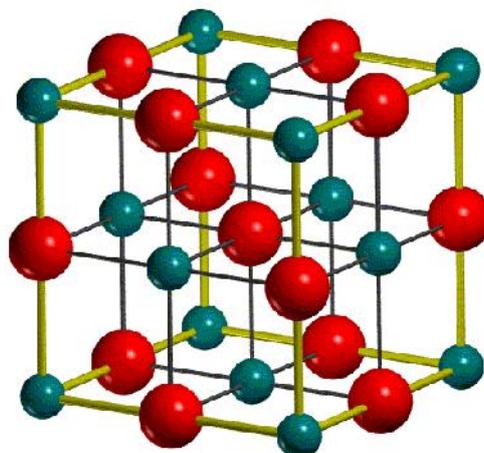
Figure 1.6 Rocksalt unit cell

The group III-nitrides have polar axes (lack of inversion symmetry). In particular, the bonds in the <0001> direction for wurtzite and <111> direction for zincblende are all faced by nitrogen in the same direction and by the cation (Al,Ga, or In) in the opposite. For example in the GaN (**Figure 1.7)** structure Ga-faced conventionally means Ga on the top position of the {0001} bilayer, corresponding to [0001] polarity.
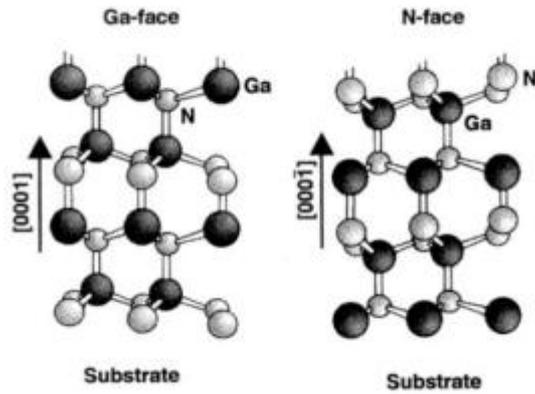
Figure 1.7 Structure of the N-face and the Ga -face GaN

CHAPTER 2

TIGHT BINDING AND DENSITY FUNCTIONAL THEORY METHODS

2.1 The Tight Binding method

The tight-binding method (TBM) or Linear Combination of Atomic Orbitals (LCAO) approach is based on the idea that in solids the electrons are tightly bound to their nuclei as in the atoms, the lattice can hence be modeled as a combination of atomic orbitals at each atomic position. The basic assumptions of the TBM are that a small number of basis states per unit cell is sufficient to describe the bulk band structure and that the overlap parameters, representing interactions between electrons on adjacent atoms of the localized atomic orbitals decrease rapidly with increasing distance of the atomic sites. Moreover since the inner electronic shells are only slightly affected by the field of all the other atoms, it is sufficient, for the description of the bulk band structure, to take into account the states of the outer shells.

The Schrödinger equation for an atom located at the position R_l is

$$H^{at}\left|R_l,\Gamma,\hat{},\dagger\right\rangle = E^{at}_{\Gamma,\hat{}}\left|R_l,\Gamma,\hat{},\dagger\right\rangle \tag{2.1}$$

where the atomic Hamiltonian H^{at} is:

$$H^{at} = \frac{p^2}{2m_0} + V^0(R_l,\Gamma) \tag{2.2}$$

and the basis states are $\left|R_l,\Gamma,\hat{},\dagger\right\rangle$ where: R_l is the unit cell position,   the type of atom,   the orbital type,   the spin. $V^0(R_l,)$ is the atomic potential of the atom at the position R_l. In the presence of all other atoms in the crystal, the single-particle Hamiltonian of the periodic system can be rewritten as:

$$H^{bulk} = H^{at}\left|R_l,\Gamma\right\rangle + \sum_{n\neq l,\Gamma'} V(R_n,\Gamma') \tag{2.3}$$

and the Schrödinger equation in the following way:

$$\left[H^{at}(R_l,\Gamma) + \sum_{n\neq l,\Gamma'} V(R_l,\Gamma')\right]\left|k\right\rangle = E(k)\left|k\right\rangle$$

Due to the crystal periodicity, the wave functions |k> are restricted to the first Brillouin zone and expressed in terms of Bloch functions. The wave functions are then approximated by linear combinations of the atomic orbitals:

$$\left|k\right\rangle = \sqrt{\frac{V_0}{V}}\sum_n e^{ikR_n}\sum_{\Gamma,\hat{},\dagger} e^{ik\Delta_\Gamma} u_{\Gamma,\hat{},\dagger}(k)\left|R_n,\Gamma,\hat{},\dagger\right\rangle \tag{2.6}$$

where   is the position of the atom   in the unit cell R_n, V_0 volume of the unit cell and V the volume of the system.

Replacing the wave function of Eq. (2.6) into the Schrödinger equation we get a matrix equation:

$$\sum_{r,\hat{},\dagger} H^{bulk}_{r',\hat{}',\dagger';r,\hat{},\dagger}(k)u_{r,\hat{},\dagger}(k) = E(k)\sum_{r,\hat{},\dagger} S_{r',\hat{}',\dagger';r,\hat{},\dagger}(k)u_{r,\hat{},\dagger}(k) \tag{2.7}$$

where the matrix elements are:

$$H^{bulk}_{r',\hat{}',\dagger';r,\hat{},\dagger}(k) = \frac{V_0}{V}\sum e^{ik(R_m+\Delta_r-R_n-\Delta_{r'})}\left\langle R_m,r',\hat{}',\dagger'\left|H^{bulk}\right|R_n,r,\hat{},\dagger\right\rangle \tag{2.8}$$

and the overlap matrix elements are:

$$S_{r',\hat{}',\dagger';r,\hat{},\dagger}(k) = \frac{V_0}{V}\sum e^{ik(R_m+\Delta_r-R_n-\Delta_{r'})}\left\langle R_m,r',\hat{}',\dagger'\left\|R_n,r,\hat{},\dagger\right.\right\rangle \tag{2.9}$$

In the semi-empirical tight binding approach additional approximations are made:

• Since distant orbitals have negligible overlap, the interactions are limited to first, second or third .nearest neighbors,

• Orthogonal orbital are obtained by performing a Löwdin transformation **[12].**

• The so-called two-center approximation of Slater and Koster **[13]** is generally used in which only the potential due to the two atoms at which the orbitals are located is taken into account. The three-center integrals which deals with two orbitals located at different atoms, and a potential part at a third atom is considerably smaller than the two-center integrals.

The two-center approximation allows to classify the overlap integrals into two classes; on-site elements $E_{,l}$ and overlap parameters V_{r,l,r_0,l_0} where $E_{,l}$ is the atomic energy level in the presence of all the other atoms in the lattice, and V_{r,l,r_0,l_0}, called hopping matrix elements, describe the coupling between different orbitals at different sites. They give the probability amplitude of an electron moving from one site to another and correspond to the matrix elements containing orbitals from different atomic sites.

with the previous assumptions Schrödinger equation, Eq. (2.7), is reduced to:

$$\sum_{r,\hat{},\dagger} H^{bulk}_{r',\hat{}',\dagger';r,\hat{},\dagger}(k)u_{r,\hat{},\dagger}(k) = E(k)u_{r',\hat{}',\dagger'}(k) \tag{2.10}$$

the matrix elements $H^{bulk}_{\Gamma',\hat{},\dagger',\Gamma,\hat{},\dagger}(k)$ being given by:

$$\langle k,\Gamma,\hat{},\dagger \,|\, H^{bulk} \,|\, k,\Gamma,\hat{},\dagger \rangle = \frac{V_0}{V} \sum_{m,n} e^{ik(R_m - R_n)} \langle R_m,\Gamma,\hat{},\dagger \,|\, H^{bulk} \,|\, R_n,\Gamma,\hat{},\dagger \rangle \qquad (2.11)$$

The atomic wave functions being very localized, the contribution of integrals for large $|(R_m - R_n)|$ become negligible and are therefore ignored. The largest contribution is for n=m, the 'on-site' energies, then first nearest neighbor contributions ($n = m \pm 1$) etc

Slater and Koster provide, in their paper, a formalism for evaluating the hopping matrix elements in terms of two centre integrals and direction cosines. Direction cosines are the projection of an orbital's amplitude in the direction of a bond vector joining two atoms. The direction cosines associated with a hopping matrix element gives the proportion of the relevant orbitals pointing along the vector joining their two sites For an sp3 or sp3s∗ basis the interaction parameters are classified into two different types   and . These parameters are depicted in **Figure. 2.1**. V_{ss} models two interacting s-states. V_{sapc} and V_{scpa} represent the interactions between an s-state and one of the lobes of a p-state, the difference between them being where the states are situated- on the cations (c) or anions (a). Interactions between two p-states are split between two terms, V_{pp} and V_{pp} . The   term describes that part of the interaction that results from the fraction of the lobes that are pointed directly towards each other while the   term describes the contribution from the fraction of the p-states that are aligned in parallel.

In practice the $V_{ss\ast}$ and $V_{s\ast s\ast}$ are generally neglected in the sp3s∗ Hamiltonian as the $V_{s\ast p}$ terms provide the required modulation of the conduction band. For the purpose of solving the eigenvalue equation one needs to have a knowledge of Hamiltonian matrix elements formed due to orbital interactions at different interatomic sites. In the particular case where only s and p atomic orbitals are responsible for bonding, there exists only four non-zero overlap integrals as presented in Figure 2.1. If the axis of the p orbital involved in sp-bonding is parallel (perpendicular) to the interatomic vector, it is called a   ( ) bond.
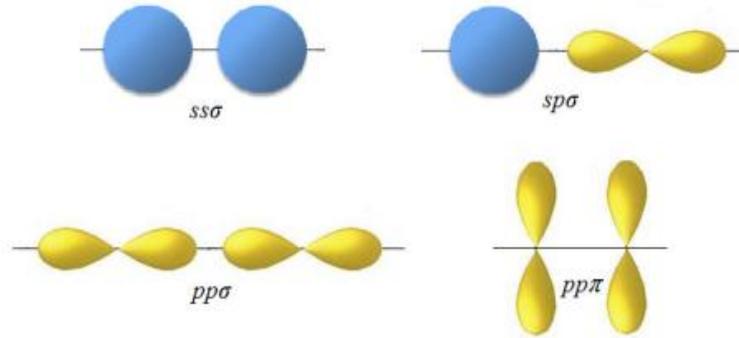
Figure 2.1 Non vanishing matrix elements between s and p in sp bonding [14].

In general, the p orbitals are not just parallel or lie along the direction of atomic bonding as is depicted in Figure (2.1), but, can also be oriented along different directions with respect to the bond length. In such cases, it becomes necessary to take projections of atomic orbitals in parallel and perpendicular direction to the bond length to account for the orbital interactions.

A projection of p orbitals is required along the direction of bond length in order to achieve well defined orbital interactions. Each p orbital thus can be decomposed into two components: (1) parallel to the line joining the atomic orbitals and (2) perpendicular to the line joining the atomic orbitals. Figure (2.2) represents a randomly oriented p atomic orbital relative to the direction of bond length. If **d** is the direction of bond length, **a** is the unit vector along one of the Cartesian axes (x, y, z) and **n** being the unit vector normal to the direction of **d**, each p orbital can then be decomposed into its parallel and normal components relative to **d**. Thus, the Hamiltonian matrix element between an s orbital at one site and a p orbital on another atomic site would be presented as

$$\langle s|H|p_a \rangle = \cos {}_{\prime\prime} \langle s|H|p_d \rangle + \sin {}_{\prime\prime} \langle s|H|p_n \rangle = H_{sp\dagger} \cos {}_{\prime\prime} \qquad (2.12)$$
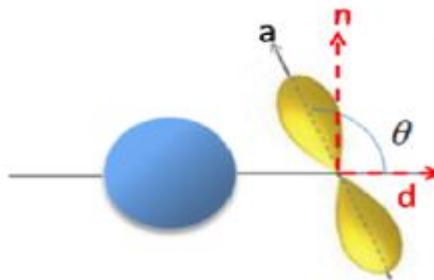
Figure 2.2 Relative orientation of p and s orbitals at an angle θ wrt the bond direction [14]

For two p orbitals oriented along the directions of unit vectors â 1 and â 2 at angles 1 and 2 respectively, relative to the direction of line joining the two p orbitals represented by d as depicted in **Figure (2.3)**, their decomposition in parallel and perpendicular directions could give Hamiltonian matrix element as a result of p − p orbitals interactions from two different site can thus be presented as

$$\langle p_a | H | p_b \rangle = \cos_{\theta 1} \cos_{\theta 2} \langle p_{d1} | H | p_{d2} \rangle + \sin_{\theta 1} \sin_{\theta 2} \langle p_{n1} | H | p_{n2} \rangle$$

$$= \cos_{\theta 1} \cos_{\theta 2} H_{pp\dagger} + \sin_{\theta 1} \sin_{\theta 2} H_{ppf} \tag{2.13}$$
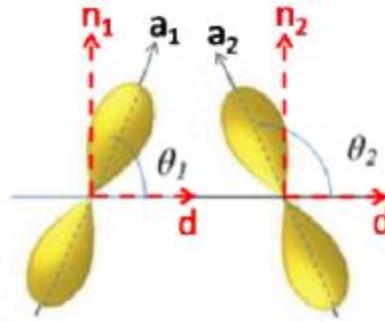
Figure 2.3 Orientation of two p orbitals at an angle θ w.r.t. the bond direction [14].

In the empirical TB model the matrix elements are treated as parameters. These parameters are obtained by fitting computed energies at high symmetry points to physical properties of the bulk band structure, such as band gaps and effective masses.

The quality of the TB band structure depends on the basis set used in the model. The minimal sp3 model (one s orbital and tree p orbitals) is quite accurate for the valence band of usual semiconductors, but less for the conduction bands, especially at high energy. The model with an extra fictious s* band **[15]** improves the description and is sufficient for describing the lowest conduction bands. The most accurate results are however obtained with the sp3d5s* model which includes 5 more d orbitals.

2.2 Density functional theory

Several physical properties of solids such as lattice constant bulk moduli piezoelectric constants defects to name a few are related to total energies. If total energies can be calculated, any of those physical properties, can be in principle be computed. The methods that obtain the total energy of a system, starting exclusively with the atomic constituents of the system, are designed as *ab-initio* or first principles methods. Density functional theory (DFT) is a powerful *ab-initio* method for the description of the ground state properties of solids. It is based on the possibility to describe the system by its electronic density, instead of using its complete many-body wave function. The Kohn-Sham (KS) equations [16] provide the way to convert the DFT a practical methodology.

2.2.1 General formulation

The starting point of DFT is a system of N interacting electrons under the influence of an external potential $V_{ext}(r)$. In most situations $V_{ext}(r)$ is the total coulombic potential created by the nuclei of the solid, assumed to be at fixed positions. The ground state many-body wave function of the system is denoted as   and the corresponding density is $n(r)$.

The energy and wavefunctions of a system of N particles can be theoretically determined by solving Schrodinger's equation:

$$H\Psi(r_1, r_2...., R_1, R_2.....) = E\Psi(r_1, r_2...., R_1, R_2.....) \tag{2.14}$$

where   is the wave function of the system, r_i and R_i are the positions of the electrons and ions respectively, and H is the Hamiltonian of the system:

$$H = -\sum_i \frac{\hbar^2 \nabla_i^2}{2m_e} - \sum_{i,I} \frac{1}{4f\nu_0} \frac{Z_I e^2}{|r_i - R_I|} + \frac{1}{2}\sum_{i \neq j} \frac{1}{4f\nu_0} \frac{e^2}{|r_i - r_j|} - \sum_I \frac{\hbar^2 \nabla_i^2}{2M_I} + \frac{1}{2}\sum_{i \neq j} \frac{1}{4f\nu_0} \frac{Z_I Z_J e^2}{|R_i - R_j|} ...(2.15)$$

$$H = T_e + V_{ext} + V_{int} + T_N + V_N \tag{2.16}$$

The Hamiltonian consists of five terms respectively: the electrons kinetic energy, the potential energy of the electrons in nuclei field, the Coulomb interaction between the electrons, the nuclei kinetic energy and the Coulomb interaction between nuclei. The problem

of solving the Schrödinger equation of a solid, where there are numerous nuclei and electrons is not computationally possible without some simplifications. The first of these is the Born-Oppenheimer approximation, which exploits the large difference in mass between the electrons and the nuclei.

In the Born Oppenheimer approximation, the ions are considered quasi-stationary since that the nucleus mass is much larger than the electron mass, and hence the electronic and nuclear dynamics are decoupled. The many-body problem is reduced to in a Hamiltonian in some set configuration of nuclei.

The density functional theory DFT replaces the many-body problem of an interacting electron gas in the presence of nuclei to of a single particle moving in an effective nonlocal potential taking the electronic density n as the key variable.

DFT is based primarily on two theorems by Hohenberg-Kohn **[17]**, stating that the total energy of an electron gas is a unique functional of the electron density, and that the ground state energy of the system can be obtained through minimization of the total energy functional with respect to the density. The electron ground state density can replace the wave function without any loss of information and the density that yields the minimum energy is the single-particle ground state density.

Theorem 1. For any system of interacting particles in an external potential $V_{ext}(r)$ the potential $V_{ext}(r)$ is determined uniquely, except for a constant, by the ground state density $n_0(r)$.

The first Hohenberg-Kohn theorem establishes that the ground state density $n(r)$ uniquely determines the external potential $V_{ext}(r)$. This implies that all the properties can thus be extracted from the exact ground state electron density.

Theorem 2. A universal functional for the energy $E[n]$ in terms of the density $n(r)$ can be defined, valid for any external potential $V_{ext}(r)$. The exact ground state energy of the system is the global minimum of this functional and the density that minimizes the functional is the exact ground state density $n_0(r)$.

This reduces the very complex problem of finding all ground state physical properties of a system to finding the minimum of the energy with respect to the electron density.

The second Hohenberg-Kohn theorem **[18]** demonstrates that the functional E[n] defined as follows has its minimum value for the ground state density:

$$E_{HK}[n] = T[n] + E_{int}[n] + \int V_{ext}(r)n(r)dr \qquad (2.17)$$

where is the $E_{HK}[n]$ total energy functional, $T[n]$ its kinetic energy part and $E_{int}[n]$ the part coming from the electronic interactions.

Unfortunately, the Hohenberg-Kohn theorems does not provide the exact functional $E_{HK}[n]$, and the problem of determining the ground state energy and density is subordinate to the discovery of sufficiently accurate estimations of such functional.

2.2.2 Kohn-Sham equations:

These equations establish the methodology for the practical use of the Hohenberg-Kohn theorems. In these equations, the interacting electron system under the influence of the external potential is represented by a system of non-interacting electrons under the influence of an effective potential. This potential, called Kohn-Sham (KS) potential $V_{KS}(r)$, is chosen in such a way that its ground state density is the same as that of the interacting electron system. The one-electron KS wave functions are then the solutions of the single-particle Schrödinger equation:

$$\left[-\frac{1}{2}\nabla^2 + V_{KS}(r) \right]\Phi_i(r) = v_i\Phi_i(r) \qquad (2.18)$$

where $_i$ are the energy eigenvalues.

The density $n(r)$ is written as follows:

$$n(r) = \sum_i^N |\Phi_i(r)|^2 \qquad (2.19)$$

Now we define the mean-field kinetic energy of the non-interacting electrons as follows:

$$T_s[n] = \sum_{i=1}^N \left\langle \Phi_i \left| -\frac{1}{2}\nabla_i^2 \right| \Phi_i \right\rangle \qquad (2.20)$$

that it is slightly different from the kinetic energy T of the interacting electron system. The functional F[n] is now conveniently rewritten in terms of T_s as follows:

$$F[n] = T_S[n] + V_H[n] + E_{XC}[n] \tag{2.21}$$

$$V_H[n] = \int \frac{n(r)n(r')}{|r_i - r'|} d^3 d^3 r' \tag{2.22}$$

and the term E_{XC} is the exchange-correlation energy.

The exchange energy is a consequence of the requirement for antisymmetry of the electron wavefunctions with the same spin. This antisymmetry causes a spatial separation of the electrons which reduces the Coulomb energy of the system, and this reduction computed using the Hartree-Fock approximation is called the exchange energy. The Coulomb energy can be further reduced (at a cost in kinetic energy) if electrons with opposite spins are also spatially separated, and the difference between this and that calculated using the Hartreee-Fock approximation is termed the correlation energy.

The potential V_{KS} (r) includes the external potential and the electron-electron interaction.

$$V_{KS}(r) = V_{ext}(r) + \int \frac{n(r)}{|r - r'|} d^3 r' + V_{XC} \tag{2.23}$$

where:

$$V_{XC}[n] = \frac{\partial E_{XC}}{\partial n(r)}$$

$$V_{KS}(r) = V_{ext} + V_H + V_{XC} = V_{ext}(r) + \int \frac{n(r')}{|r - r'|} dr' + \frac{\partial E_{XC}}{\partial n(r)} \tag{2.24}$$

The Kohn-Sham equations can now be solved instead of finding the minimum of Eq.(2.15), and the orbitals $_i$ (r) then give the electron density according to Eq.(2.19) above. The equations (2.18), (2.19) and (2.23) are acknowledged as Kohn-Sham equations., The ground state density and the total energy of the system can be derived by solving them self-consistently.

The Kohn-Sham equations provide the exact ground state density. However, all the benefits gained by this theoretical study depend on the ability to deal with the exchange-correlation functional, in an exact manner or by finding accurate approximations.

2.2.3 Some Exchange correlation Approximation

a) The Local Density Approximation

The most common approach for the exchange correlation potential is the Local Density Approximation (LDA). The core assumption of this approach is that the density is slowly varying. The exchange-correlation at point r can therefore be simply approximated by that due to a homogeneous electron gas of density n(r). Thus:

$$E_{XC}\left[n(r)\right] = \int \mathsf{v}_{XC}(r)n(r)d^3r \tag{2.25}$$

$$\frac{\mathsf{u}\,E_{XC}}{\mathsf{u}\,n(r)} = \frac{\partial n(r)\mathsf{v}_{XC}(r)}{\partial n(r)} \tag{2.26}$$

where

$$\mathsf{v}_{XC}(r) = \mathsf{v}_{XC}^{\text{hom}}\left[n(r)\right] \tag{2.27}$$

There are, of course, alternatives to the LDA. Of these, the most popular are those based around the generalized gradient approximation (GGA). In the GGA, the density is a function of both the electron density and its gradient, and for many materials, but not all, it has been shown to improve results for total energies and the general properties of solids.

b) The generalized gradient approximation:

In LDA one uses the knowledge of the density in a point r. In real systems the density varies in space. A logical improvement of the LDA approximation would be to include also information of this rate of change in the functional. This can be done by adding gradient terms. This approach is called the gradient-expansion approximation. In this class of approximation one tries to systematically calculate gradient-corrections of the form $|\nabla n(r)|$, $|\nabla n(r)|^2, |\nabla^2 n(r)|$ etc. to the LDA. In practice, the inclusion of low-order gradient corrections almost never improves on the LDA, and often even worsens it. Moreover higher-order corrections are exceedingly difficult to calculate and little is known about them. It was realized that instead of power-series-like systematic gradient expansions one could experiment with more general functions of n(r) and $|\nabla n(r)|$. Such functionals, of the general form:

$$E_{XC}^{GGA} = \int \mathsf{v}_{XC}(n, |\nabla n|, \nabla^2 n)dr \tag{2.28}$$

are known as generalized-gradient approximations (GGAs). The current GGAs seem to give reliable results for all main types of chemical bonds and are popular in computational chemistry. We have used the Perdew-Burke-Ernzerhof (PBE) version of GGA [19] in this work.

c)The hybrid functionals

The LDA or GGA approximation predict the structural properties such as lattice constants and bulk moduli with good accuracy. However, the LDA or GGA results for electronic properties such as band gaps are of much lower quality. The band gaps are typically underestimated by 50-100 %. Further improvements in the description of band gaps is achieved by the introduction of so-called hybrid functionals which are obtained by admixing a fixed amount of the Hartree-Fock (HF) exchange to the GGA functional. The hybrid functional proposed by Heyd, Scuseria and Ernzerhof termed as HSE06 functional [20] fulfills the need for a universally applicable method that is computationally feasible for a wide range of systems and nowadays becomes a popular choice for calculating the structural properties and the band gaps. The exchange potential employed in HSE06 is divided into short- and long-range parts, and HF exchange is mixed with Perdew-Burke-Ernzerhof(PBE) exchange in the short-range part. To avoid the expensive calculation of long-range HF exchange as well as enabling hybrid DFT calculations on metal elements for which conventional HF or global hybrid calculations are intractable, this term is replaced by long-range PBE exchange, as shown in the following equation:

$$E_{XC}^{HSE} = \frac{1}{4}E_X^{HF,sr}(\sim) + \frac{3}{4}E_X^{PBE,sr}(\sim) + E_X^{PBE,lr}(\sim) + E_C^{PBE} \qquad (2.29)$$

In addition to the aforementioned functionals we can also cite the meta-GGA's like TPSS [21] where typically the kinetic energy is used $E_{xc}(n(r), \nabla n(r), \nabla^2 (r))$.

2.2.4 The band gap problem in DFT

In DFT the lattice parameters and atomic positions are accurately predicted within an error of 1 to 5%, depending of exchange correlation functional used. However the band gaps calculated within DFT show a large underestimation compared to experiment. Nonetheless, this underestimation of the band gap is not surprising since the Kohn-Sham eigenvalues are completely artificial objects. These are the eigenvalues of a non-interacting system chosen to

yield the same density as the many-body interacting system. There is no physical basis to interpret the Kohn-Sham gaps as the real experimental gaps. However, in practice, such a comparison is motivated by the close resemblance observed between the Kohn-Sham band structure and the real band structure for many systems.
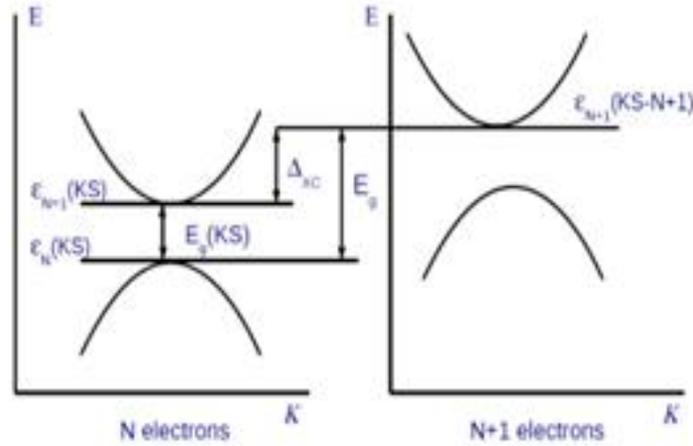
Figure 2.4 Schematic picture of the real band gap and Kohn Sham gap

The band dispersion shows a good agreement with the experiments. The band gaps of semiconductors are differences of ground-state energies (E) of N and N ± 1 particle systems:

$$E_g = E(N+1) + E(N-1) - 2E(N) = I - A \tag{2.30}$$

where I represents the ionization potential and A represents the electron affinity of the system. In particular, the lowest conduction band energy is given by $_c = E_{N+1} - E_N$ and highest valence band energy corresponds to $_v = E_N - E_{N-1}$. Similar to metals, the highest "occupied "eigenenergy for the N-electron system $_N$ (N) is the Fermi energy and thus $_c = _{N+1}$ (N +1), $_v = _N$ (N). Hence, the energy gap is related to the eigenenergies as:

$$E_g = v_{N+1}(N+1) + v_N(N) \tag{2.31}$$

It is different from the definition of the band gap in terms of only N-particle eigenenergies given by:

$$v_g = v_{N+1}(N) - v_N(N) \tag{2.32}$$

This deviation is given by:

$$\Delta_{XC} = v_{N+1}(N+1) - v_{N+1}(N) \tag{2.33}$$

and corresponds to the neglected derivative discontinuity $_{XC}$ by the standard local and semi-local exchange-correlation functionals **[22,23].** It is illustrated schematically in **Figure**. **2.4**. $_{XC}$ is given by:

$$\Delta_{XC} = \lim_{y \to 0} \left(\frac{\text{u} E_{XC}}{\text{u} n} \Big|_{N+y} - \frac{\text{u} E_{XC}}{\text{u} n} \Big|_{N-y} \right) \tag{2.34}$$

To calculate $_{XC}$, DFT had to be extended to describe systems with fractional number of particles N $\pm$. The evaluation of E_{XC} / n(r) at N $\pm$ ensures that the discontinuity at integer particle number N is captured. Depending on the approximation used for E_{XC} the results differ strongly. For LDA and all GGAs, $_{XC}$ = 0. Therefore, the fundamental gap is given solely by the Kohn-Sham gap which is always underestimated compared to the experiment. The essence of this result is that even with the exact XC functional the Kohn-Sham band structure does not provide the fundamental band gap of the real interacting-electron system as it does not include the finite and positive derivative discontinuity.

A detailed account on this paragraph is given in the original paper by Perdew **[24]** or in the book by Engel **[25].**

2.2.5 Tran-Blaha modified Beck Johnson potential

As LDA and GGA can only reproduce the band structure but cannot produce a band gap of comparable value to that obtained experimentally, Becke and Johnson (BJ) developed a BJ potential **[26]**, that improves the band gap in comparison with LDA and GGA functionals. It can be formulated as:

$$V_{x,\uparrow}^{mBJ}(r) = V_{x,\uparrow}^{BR}(r) + \frac{\sqrt{5}}{6f} \frac{\sqrt{t_\uparrow(r)}}{\ldots_\uparrow(r)} \tag{2.35}$$

where denotes electron density and t represents kinetic energy .

Blaha et al. **[10]** further modified the exchange and correlation potential of the BJ approach, and developed the mBJ potential, capable of better reproducing the experimental gap of semiconductors in comparison to the LDA or the GGA. The mBJ potential is given by:

$$V_{x,\uparrow}^{mBJ}(r) = cV_{x,\uparrow}^{BR}(r) + (3c-2)\frac{\sqrt{5}}{12f}\frac{\sqrt{2t_\uparrow(r)}}{\dots_\uparrow(r)} \qquad (2.36)$$

where (r), t (r) and $V^{BR}x$, (r) are the spin-dependent density of states, kinetic energy density and the Becke-Roussel potential (BR), respectively. In the TB-mBJ, the value of c is calculated by:

$$c = \Gamma + s\left(\frac{1}{V_{cell}}\int_{cell}\frac{|\nabla_{\dots}(r')|}{\dots(r')}\right)^{\frac{1}{2}} \qquad (2.37)$$

where V cell is the unit cell volume, an and are the free parameters with the value of - 0.012 and 1.023 Bohr, respectively. The only disadvantage of the TB-mBJ potential is that the derivative of a XC functional cannot be obtained. Consequently, this potential cannot be used for the calculation of forces that act on the nuclei, which is required for the optimization of the geometry.

Figure 2.5 [10] show the remarkable improvement obtained with the Tran-Blaha potential. The gaps are more accurate than with LDA or GGA and nearly as precise as those obtained by much more time consuming functionals like HSE or G_0W_0.
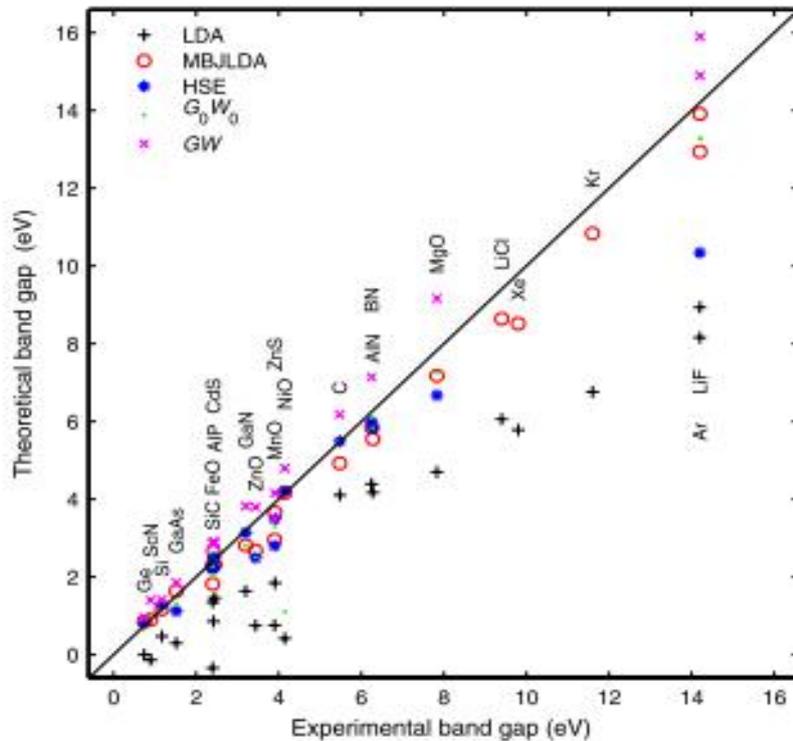
Figure 2.5 Theoretical versus experimental band gaps.

2.3 Implementations of Density Functional Theory

Density functional theory is implemented in a variety of software packages such as VASP **[27],** SIESTA **[28],** Wien2k **[29],** Abinit **[30,31],** Quantum espresso **[32]** and many others.

The existing implementations can be divided into two main groups: all-electron implementation (i.e. Wien2k) and pseudopotential implementations (i.e. SIESTA, VASP). The last ones treat only valence electrons and replaces the core electrons by an effective pseudopotential. This allows to speed up the calculations but leads to less accurate solutions in comparison to the all electron methods. In this section we describe two main methods and software which were applied in the calculations on this thesis: the pseudopotential method as implemented in Abinit or VASP and LAPW+lo method implemented in Wien2k program.

We practically have three basis sets used in the expansion of Kohn-Sham orbitals: the plane-wave basis, the linear combination of localized atomic orbitals (LCAO) and a mixed plane-wave and atomic basis set.

2.3.1 Pseudopotentials

A pseudopotential is an effective potential designed to substitute to the all-electron potential of Eq. (2.15), and is constructed to reproduce the effects of the all-electron system on the valence states beyond a certain cutoff distance from the ionic core. In a pseudopotential calculation, the "core" consists of the nucleus and the inner electrons, which are highly localized around the nucleus. Outside the core region (that is beyond the cutoff), the potential matches the Coulomb interaction between the core (whose ionic charge Z_{core} equals that of the nucleus minus the inner electrons) and each of the valence electrons. Inside the core region, the Coulomb potential is replaced by a smooth function which is more easily representable, for instance, by plane waves. Pseudopotentials (PP) are constructed so that the wave functions of the valence electrons outside the core region match those of an all-electron calculation, in a calculation for the isolated atom. To illustrate this, **Figure 2.6** show the radial part (r) of the 2s and 2p orbitals of atomic C together with the corresponding pseudo wave functions obtained with PP designed to make them match at r_c.
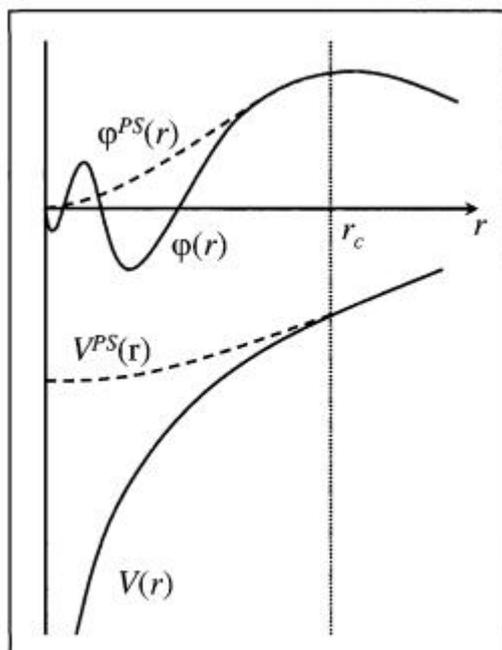
Fig 2.6 Schematic illustration of the replacement of the all-electron wavefunction and core potential by a pseudo-wavefunction and pseudopotential. **[33].**

The main argument underlying the use and success of pseudopotentials is the fact that most chemical properties of atoms can be accurately modeled taking account of the interacting valence states alone. The core states, much lower in energy, have little interaction with valence states of the same or surrounding atoms.

The most common types of *ab-initio* pseudopotentials are "norm-conserving" and "ultrasoft" pseudopotentials. If the pseudo and AE charge densities within the core are constructed to be equal, the type of PP is called the norm-conserving PP **[34,35].** Many PP are generated to meet this criterion:

$$. \int_0^{r_c} \left| \textcE_{pp}(r) \right|^2 dr = \int_0^{r_c} \left| \textcE_{AE}(r) \right|^2 dr \tag{2.38}$$

On the other hand, if we forget about the norm conserving condition and in addition to the elimination of radial nodes, shift the peak position of a wave function further to a bigger r_c with reduced peak height, the so-generated potentials introduced by Vanderbilt **[36]** are called ultrasoft PPs. They present better computational efficiency at the cost of complicating the formulas.

The "hardness" of a pseudopotential refers to how smooth or soft the potential looks in real space, in particular how rapidly the corresponding pseudo wavefunctions vary in the core region. In the context of plane wave calculations, functions that are smooth in real space can be represented in reciprocal space by a lower number of plane waves, compared to more rapidly varying functions.

In recent times, the projector augmented-wave method (PAW) has gained popularity due to its providing further computational advantages compared to the norm-conserving and ultrasoft pseudopotential methods. Projector augmented wave (PAW) potential may be classified as a frozen-core AE potential. This type, first proposed by Blöchl (1994) **[37]** and adopted by Kresse and Joubert (1999) **[38],** aims for both the efficiency of the PP and the accuracy of the AE potential. It maps both core and parts of valence wavefunctions with two separate descriptions.

The wavefunction ($_{inter}$) of the valence part is represented with a PW expansion, while the wavefunction ($_{core}$) of the core part is projected on a radial grid at the atom center. After the additive augmentation of these two terms, the overlapping part $_{net}$ is trimmed off to make the final wavefunction, $_{PAW}$ very close to the AE wavefunction.

2.3.2 The VASP package

Vasp, or the Vienna Ab initio Simulation Package, is a powerful computational tool for total energy calculations using a plane-wave basis set. In Vasp , the Schrodinger equation is solved self-consistently by iteratively optimizing the charge density that determines the KS Hamiltonian that, in turn, determines the single-particle eigenstates. These eigenstates are used to calculate the new charge density that will serve as an input for the following iteration. The total energy difference between one iteration and the following will progressively decrease as convergence (and hence self-consistency) is achieved. Once the energy difference between two consecutive iterations falls within the desired precision range, the iterative process comes to an end: the single-particle eigenstates determine a charge density which gives rise to those same eigenstates. This basic procedure is shown as a chart in **Figure 2.7.**

The pseudopotential is calculated by solving Kohn-Sham equations for the core electrons:

$$(-\frac{1}{2r}\frac{d^2}{dr^2}r+\frac{l(l+1)}{2r^2}+V_{xc}(r)+V_{hartree}(r)+V_l(r))\Phi_{\ln}(r)=V_{\ln}\Phi_{\ln}(r) \qquad (2.39)$$

Here $V_{Hartree}$ and V_{xc} are Hartree and exchange-correlation potentials, respectively, V_l is a part of pseudopotential called "semilocal potential", l is the angular momentum. The pseudopotential and the eigenfunctions are calculated by the following expressions:

$$V_{ln}^{pseudo}(r) = \langle \{_{ln} | V_l(r) | \{_{ln} \rangle$$

$$\{_{ln}(r) = Œ_{ln}(r) - \sum_{n'=1}^{n-1} \{_{ln'}(r) \frac{\langle \{_{ln'} | V_l(r) - V_{local}(r) | Œ_{ln} \rangle}{\langle \{_{ln'} | V_l(r) - V_{local}(r) | \{_{ln} \rangle}$$

(2.40)
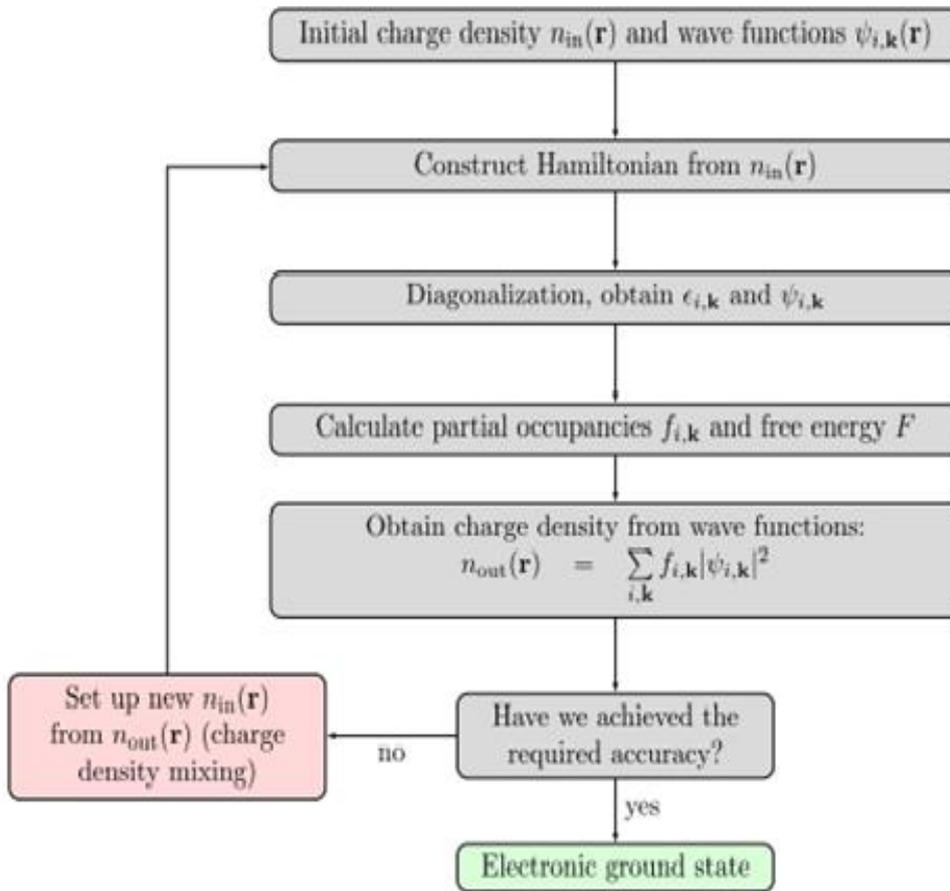
Figure 2.7 VASP basic procedure towards obtaining self-consistently electronic ground state.

2.3.3 LAPW methods

The Linearized Augmented Plane-Wave Method (LAPW) is an all-electron method implemented among others in Wien2k software package. It is the improvement of the original

Augmented Plane-Wave Method (APW), which was used in this package before. The idea of this method lies in the fact that in the region far away from nucleus, the electrons behave like free electrons and can therefore be described by plane waves. In contrast, the electrons close to the nucleus behave like they were in the free atom and can be described by spherical functions which are the solutions of Schrodinger equation for a single atom. So, following this idea, the unit cell of the system is partitioned into atom-centered spheres of selected radii and the interstitial region (**Figure.2.8**). The atomic spheres are called Muffin-Tin Spheres (MTS) and their radii are called muffin-tin radii (RMT).
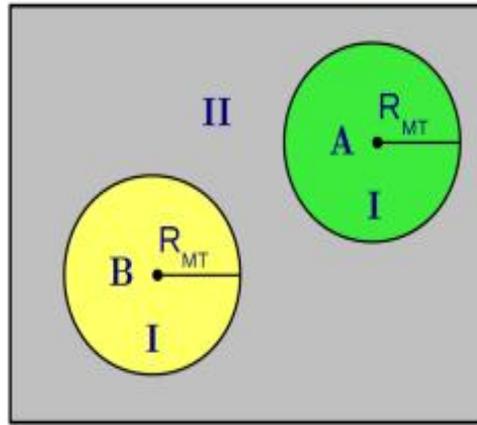
Figure 2.8 Schematic division of unit cell containing two types of atoms A and B in Muffin-Tin spheres(I) and an interstitial region (II).

In these two regions two different basis sets are used for solving Kohn-Sham equations. In the interstitial region the plane-wave expansion of Kohn-Sham orbitals is used:

$$\Phi^k(r,E) = \frac{1}{\sqrt{V}} e^{i(k+G)r} \tag{2.41}$$

Here k is the wave vector in the first Brillouin zone, G is a reciprocal lattice vector, V is a unit cell volume. Inside the atomic sphere an expansion of spherical harmonics times radial functions is used:

$$\Phi^k(r,E) = \sum_{lm} A_{lm}^j u_l^j(r',E) Y_{lm}(r) \tag{2.42}$$

Here Y_{lm} (r) are spherical harmonics, A_{lm}^j are expansion coefficients (unknown at the beginning), E is the parameter with the dimension of energy, u_l^j (r, E) is the solution of the Schrodinger equation for the atom j at the energy E. Of course, these two parts of the basis set should match together at $r_j = RMT_j$, where RMT_j is j-th atom muffin-tin radius (RMT). Expanding the plane-wave part (Eq. 2.42) into the basis of spherical harmonics and comparing it to the atomic part of the basis set (Eq. 2.43) at $r_j = RMT_j$, gives the expression for A_{lm}^j:

$$A_{lm}^j = \frac{4f\, i^l e^{i(k+G)r_j}}{\sqrt{V} u_l^j(R_j^{MT},E)} j_l(|k+G|R_j^{MT}) Y_{lm}(k+G) \tag{2.43}$$

here j is a Bessel function of order l.

LAPW method: In order to solve the Kohn-Sham equations with such a basis one needs to "guess" the value of the parameter E, then solve the equations and determine E from them again. That's time consuming and that is the reason why APW method is replaced by more efficient one. Unlike this method, the LAPW method sets this parameter fixed to some value $E = E_0$ (it is called linearization energy), and the Schrodinger equation is solved to determine $u_{jl}(r, E_0)$. Since the eigenstate E remains unknown we have to introduce a new parameter $B_{lm}^j = A_{lm}^j(E_0 - v_k^n)$.

So that:

$$\{_G^k(r,E) = \sum_{lm} (A_{lm}^j u_l^j(r',E_0) + B_{lm}^j \dot{u}_l^j(r',E_0)) Y_{lm}(r') \tag{2.44}$$

The coefficients B_{jlm} and A_{jlm} can be determined by matching the basis at the boundary. As we now have a fixed value E_0, the basis can be determined uniquely from the linearization energy E_0. One has to note that different atoms will have different linearization energies depending on the dominant orbitals and so the basis will vary.

2.3.4 Wien2k package

The diagram of a Wien2k program execution is represented in **Figure 2.9**. A self consistent calculation SCF is preceded by some steps:

The first one deals with the generation of the structure by selecting the space group, lattice coordinates, constituent atoms and appropriate RMT's. Then follow an initialization step in which the symmetry of the system is detected, followed by inputting the number of terms being used for an expansion into spherical harmonics $_{max}$, the cut-off parameter K_{max} for plane wave expansion and the sampling density of the reciprocal space defined by the number of k-points in the irreducible Brillouin zone (IBZ). Finally before starting a SCF spin-polarization, spin–orbit coupling diagonalization matrix method and electron and charge convergence limit are selected. Various properties to name a few like lattice constant bulk modulus, density of state, electronic structure elastic may be extracted after completion of the SCF cycles.
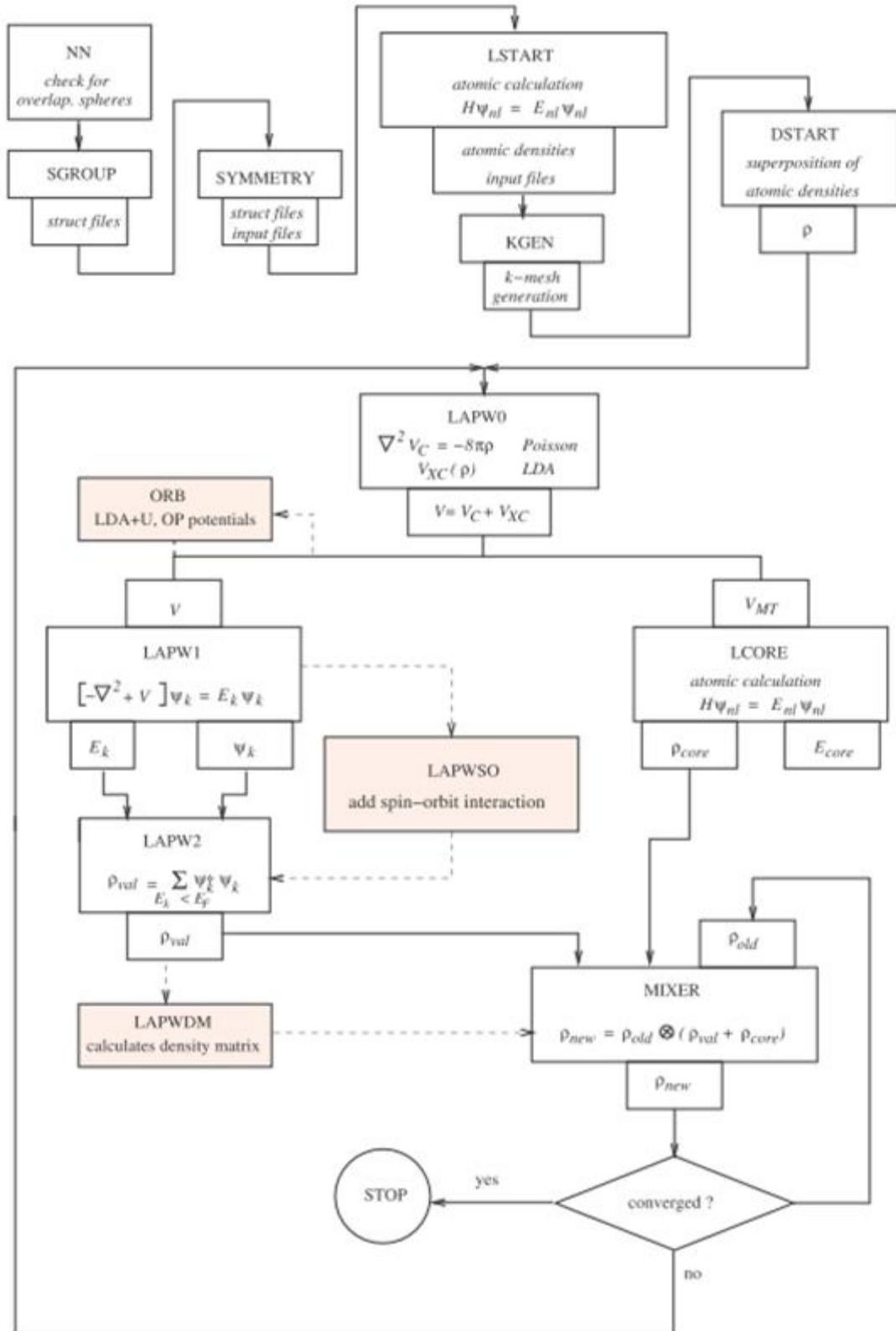
Figure 2.9 Diagram of a standard Wien2k calculation **[39]**

CHAPTER 3

STRUCTURAL AND ELECTRONIC PROPERTIES; HIGH PRESSURE EFFECTS

3.1 Computational parametrizing

3.1.1 Density Functional Theory Calculation

The DFT-based *ab-initio* calculations were performed by means of Wien2k and VASP codes.

Wien2k tuning

Wien2k uses the full potential linearized augmented plane wave (FP-LAPW) method. Inside each atomic sphere the wave function is approximated by a linear combination of radial functions times spherical harmonics, while in the interstitial region a plane wave expansion is used, with an energy separation between valence and core states of 6 Ry. The l-expansion (azimutal quantum number) of the non-spherical potential and charge density inside MTS was carried out up to $l_{max} = 10$. The plane waves were expanded up to a cut-off parameter, K_{max}, so that $R_{MT}K_{max} = 7$ where RMT is the average radius of MTS. The convergence of total energy was set to an accuracy of 0.1 mRy. Starting from bulk AlN structure we obtained the ternary $Al_{1-x}In_xN$ (x=0.25, 0.5, 0.75, 1) by replacing the Al atoms with In in the supercell. For the wurtzite structure of the ternary (**Figure 3.1)** calculation were carried out using a supercell of 16 atoms (2x2x1) in an ordered form, whereas for the zincblende form a 8-atom supercell having luzonite structure for x=0.25, 0.75 and a chalcopyrite (**Figure 3.2)** for x=0.50 was used. The sampling density of the reciprocal space defined by the number of k-points, whose value needed a convergence test with respect to the energy, was found to be 1500 k-points in the irreducible Brillouin zone (IBZ) for both binary compounds structures. A proportionally smaller number of k-points was used for the ternary calculation.
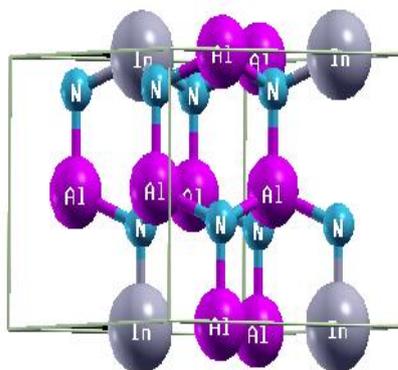
Figure 3.1 $Al_{75}In_{25}N$ wurtzite cell
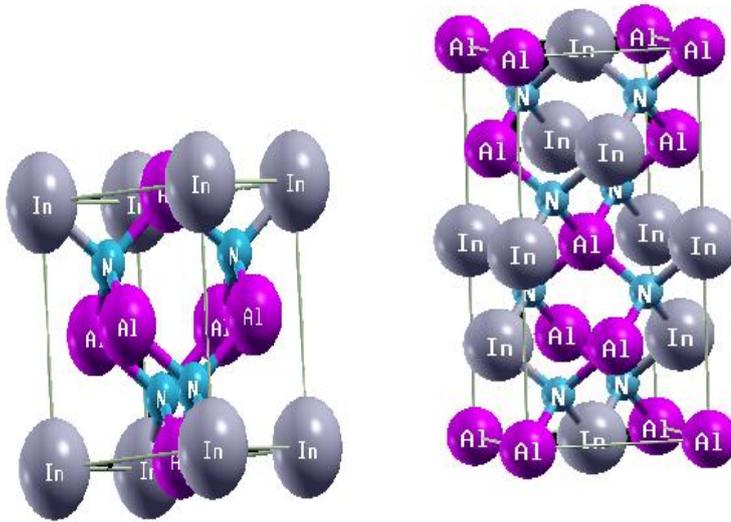
Figure 3.2 $Al_{1-x}In_xN$ zincblende cell: Left: (luzonite), right: (chalcopyrite).

VASP tuning

Starting from bulk AlN structure the ternary $Al_{1-x}In_xN$ (x varying from 0 to 1) was obtained by replacing, in a supercell of 64 atoms **(Figure 3.3)**, the Al with In atoms in a proportion step variation x of 0.125. Alloy disorder was taken into account for all phases by using a special quasi-random structure (SQS) [**40,41**] in the 64-atom supercell and was implemented by means of the Alloy Theoretic Automated Toolkit (ATAT) **[42].** The SQS approach proved to be an efficient method for calculating random alloy physical properties **[43,44]**, it is designed in a manner that In or Al atomic sites of the supercell are occupied in such a way that the pair correlation function reproduces that of an infinite random alloy.
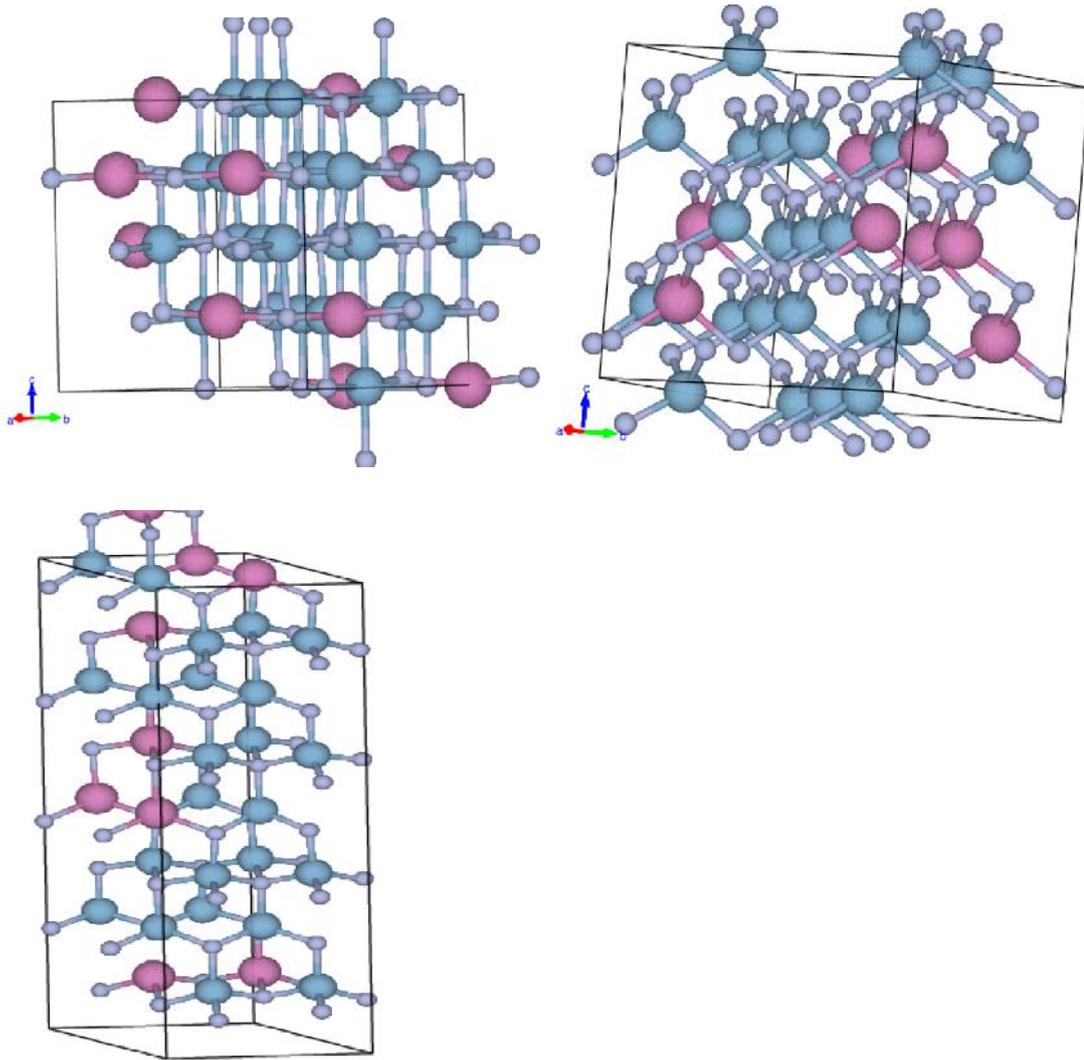
Figure 3.3 Special quasi-random 64-atom supercell $Al_{0.75}In_{0.25}N$ derived with ATAT. top left: rocksalt structure top right: zincblende structure, bottom: wurtzite structure.

The interaction between the ionic cores and the valence electrons were treated in the VASP code by the projector-augmented-wave (PAW) method.

The Brillouin integration for binaries was performed using a Gamma centered grid of 8x8x8 for both B1 and B3 AlN and InN and 8x8x6 for B4. For ternary $Al_{1-x}In_xN$, a 4x4x4 k-points sampling grid was selected for B1 and B3 phases and a 6x6x2 for B4. Calculations for all phases were performed with a plane wave basis set with an energy cut-off of 600 eV and an energy convergence criteria fixed at 0.01meV.

For both codes, the Perdew, Burke and Ernezerhof (PBE)sol **[45]** exchange correlation functional, a modified version for solids of PBE, was utilized for total energy and lattice

parameter calculations while, since PBE greatly underestimates band gaps, the Tran-Blaha potential was employed in the energy gap calculations.

3.1.2 Semi-empirical tight binding calculation

The nearest neighbor (NN) *sp3s** tight binding model was adopted since it has proved to be sufficiently precise as regards to the electronic properties. In this model every atom is described by valence s orbital and the outer p orbital and an *s** state added to reproduce high orbital states. The spin orbit effect is neglected regarding the type of atoms used. The resulting zincblende and wurtzite structures Hamiltonian matrices are respectively 10x10 and 20x20 matrices.

The tight binding parameters on-site energies E_{sa}, E_{sc}, E_{pa}, E_{pc}, E_{s*a}, E_{s*c} and the off diagonal elements V_{ss}, V_{xx}, V_{sapc}, V_{scpa}, V_{xy}, V_{s*p}, V_{p*s} for binary compounds are obtained from available literature and modified so as to reproduce physical properties such as band gap or effective mass obtained from experimental data[A1,A2].

The calculation of atomic energies for the $Al_{1-x}In_xN$ ternary is carried out by using the virtual crystal approximation

$$E_{vi}(x) = xE_{vi,AlN} + (1-x)E_{vi,InN}$$

$$V_{vi}(x) = xV_{vi,AlN} + (1-x)V_{vi,InN}$$

where $i=s$, p_x, p_y, p_z, s^* and $= $, *with* $V_i = V_{ss}$, V_{xx}, V_{sapc}, V_{scpa}, V_{xy}, V_{s*p}, V_{p*s}.

Using the derived matrix parameters, the energy bands are obtained by diagonalizing the Hamiltonian matrix at each point of the Brillouin zone The matrix diagonalization and eigenvalues were computed by means of MATLAB codes.

3.2 Structural and electronic properties

3.2.1 Structural properties

The equilibrium lattice parameters and the bulk modulus of the ternary $Al_{1-x}In_xN$ alloys are determined by calculating the total energy at various volumes and fitting it to the pressure versus volume Birch-Murnaghan equation of state **[46]** in its third-order expansion of volume as expressed in equation (3.1):

$$P(V) = \frac{3B_0}{2}\left[\left(\frac{V_0}{V}\right)^{7/3} - \left(\frac{V_0}{V}\right)^{5/3}\right]\left\{1 + \frac{3}{4}\left(B_0' - 4\right)\left[\left(\frac{V_0}{V}\right)^{2/3} - 1\right]\right\} \qquad (3.1)$$

where P is the pressure, V_0 the equilibrium volume, V the deformed volume, B_0 the bulk modulus and B_0' its pressure derivative.

The results obtained for the various phases ground state energy confirms the B4 phase as the most favorable for the entire x range. The ground state energy difference E with respect to B4 is, on one hand, small for the B3 phase ranging from 22 (x=0) to 18.8meV/atom (x=1), and on the other hand rather significant for the B1 phase ranging from 81 (x=0) to 63.5 meV/atom (x=1). B1, B3 and B4 phases computed lattice parameters along with experimental and others *ab-initio* data are listed in **Table 3 1.**

The lattice constants, represented in **Figure 3 4**, are increasing with In contents. The phases B3 is presenting the largest lattice constant ranging from 4.37 Å (x=0) to 5.05 Å (x=1) compared to B1 varying from 4.04 to 4.67Å, whereas the parameter a and c of the B4 phase vary respectively from 3.11 to 3.58 Å and from 4.98 to 5.77 Å.

The lattice constants of the $Al_{1-x}In_xN$ ternary alloys may be expressed in terms of the binaries parents by:

$$a(x) = x.a_{InN} + (1-x).a_{AlN} + b.x.(1-x) \qquad (3.2)$$

with the term *b.x.(1-x)* representing the linearity correction term due to the lattice distortion.

We observe very little deviation from linearity for all phases, with the bowing parameter b calculated values of 0.020; -0.253; 0.006 for B3, B1 and B4 phases respectively.

Table 3.1. Lattice parameters for AlN, InN and their alloys $Al_{1-x}In_xN$ (B1, B3 and B4 phases).

Composition x	a (Å)			c (Å)
	$\overline{B1}$	$\overline{B3}$	$\overline{B4}$	$\overline{B4}$
0 TW	4.044	4.377	3.113	4.982
Exp.	4.043[a]	4.37[b], 4.38[c]	3.112[d], 3.111[e]	4.982[d], 4.978[e] 5.006[h] 4.959[k]
Others	4.069[h],4.072[j]	4.396[h] 4.353[k], 4.308[l]	3.124[h] 3.096[k]	
0.125 TW	4.155	4.459	3.170	5.096
0.25 TW	4.266	4.544	3.227	5.199
0.375 TW	4.339	4.623	3.294	5.291
0.5 TW	4.437	4.708	3.345	5.400
0.625 TW	4.483	4.796	3.410	5.482
0.75 TW	4.545	4.878	3.463	5.584
0.875 TW	4.615	4.962	3.526	5.682
1 TW	4.676	5.052	3.587	5,775
Exp.	4.688[g]	4.98[m],	3.548[d], 3.533[e]	5.760[d], 5.693[e]
Others	4.636[o] 4.641[r]	4.947[i], 4.980[k]	3.58[p], 3.544[s]	5.722[l], 5.751[s]

Note: This work (TW)

a: Ref. [8], b: Ref. [47,48], c: Ref. [49], d: Ref. [50],e: Ref. [51], g: Ref. [52], h: Ref.[53], i: Ref. [54], j: Ref. [55], k: Ref. [56], l: Ref. [57], m: Ref. [58,59], o: Ref. [60], p: Ref. [61], r: Ref. [62], s: Ref. [63]
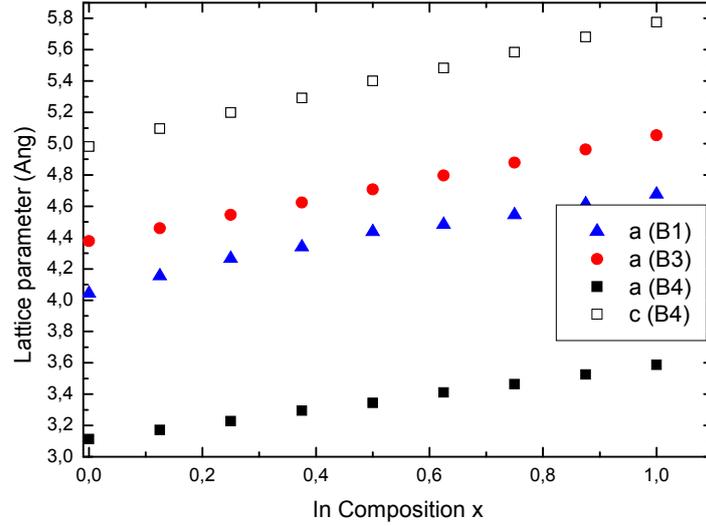
Figure 3.4 Lattice parameters of $Al_{1-x}In_xN$: the AlInP versus In composition (B1, B3 and B4 phases).

Computed bulk modulus (BM) B and its derivative B' for B1, B3 and B4 phases along with experimental and others *ab-initio* findings are listed in **Table 3.2** and represented in **Figure 3.5**.

The first things to note are the large values obtained compared to the other III-V families phosphides, antimonides and arsenides alloyed with In. The BM of AlInP, AlInSb and AlInAs varies respectively, with In, in the range [82 71] [58 43] [75 60] GPa. The other fact is that BM decreases as the In content is increased. This can be a consequence of a longer lattice parameter leading to a weaker bond. Furthermore, the bulk modulus presents the largest value for B1 phase and close values for B3 and B4 phases. This may be traced back to the fact that the B1 phase has a shorter lattice constant and B3 and B4 phases have similar bond lengths and coordinate numbers. There also seems to be a discontinuity in the BM B1 curve occurring at a composition of 0.5 this may be due to the fact that AlN and InN have different phase transition pressures and so is the evolution of the $Al_{1-x}In_xN$ and $In_{1-x}Al_xN$ curves.

The variation of B with In content x which can expressed as :

$$B(x) = x.B_{InN} + (1 - x).B_{AlN} + b.x.(1 - x) \qquad (3.3)$$

The bulk modulus bowing parameters for B3, B1 and B4 phases are respectively 21.28, 67.42, 24.33 GPa. A relatively large deviation from linearity is then noticed and may be attributed to the AlN and InN lattice parameter mismatch.

Table 3.2 Bulk modulus B and its fist derivative B'$_0$ for AlN, InN and their alloys Al$_{1-x}$In$_x$N (B1, B3 and B4 phases).

Composition x	$\overline{B\ (GPa)}$			$\overline{B'(GPa)}$		
	$\overline{B^1}$	$\overline{B^3}$	$\overline{B^4}$	$\overline{B^1}$	$\overline{B^3}$	$\overline{B^4}$
0 TW	264.32	202.43	203.33	3.935	3.87	3.866
Exp.	221[f]	---	207.9[f]	4.8[g]	---	5.7-6.3[g]
Others	272[g]	211.78[i], 213.03[l]	209[g]	3.8[g]	3.90[i] 3.7[g]	3.7[f]
0.125 TW	249.18	192.91	193.65	4.121	3.904	3.664
0.25 TW	223.92	183.51	184.66	4.546	3.964	3.648
0.375 TW	195.07	176.59	175.10	5.245	3.959	3.609
0.5 TW	167.15	167.69	166.90	5.955	3.991	3.909
0.625 TW	208.37	158.24	159.19	4.670	4.236	3.579
0.75 TW	203.33	152.65	149.04	4.762	4.278	4.414
0.875 TW	198.78	147.53	146.03	4.838	4.321	4.344
1 TW	193.39	142.56	141.82	4.931	4.443	4.477
Exp.	170[f]	137[f]	125[f]	5.0[g]	----	12.7[n]
Others	170.0[r], 186[t]	144[i], 143.41[h]	125.5[q], 143[t]	4.6[g] 6.0[t]	4.56[i], 4.558[l]	4.6[g]

f: Ref. [64], g: Ref. [52], h: Ref.[53], i: Ref. [54], l: Ref. [57], n: Ref. [65], q: Ref. [66], r: Ref. [62], t: Ref. [67].
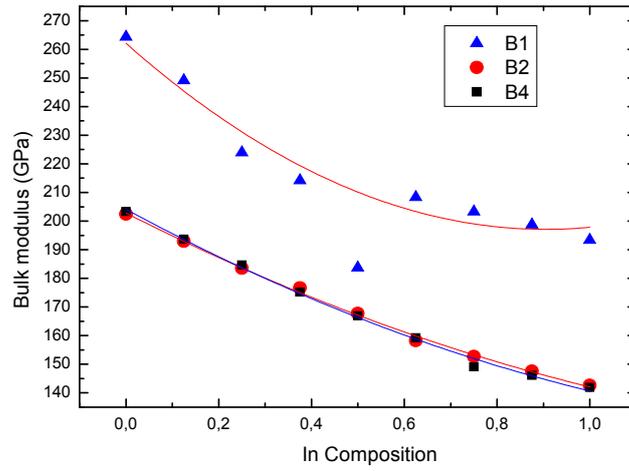
Figure 3.5 Bulk modulus of $Al_{1-x}In_xN$ vs In composition (B1, B3 and B4 phases).

Table 3.3. Bowing parameters of bulk modulus

Bowing parameter	Phase	*This work*	*Others*
Bulk modulus	*B3*	21,28	10.34 ± 9.37[a]
	B1	67,42	----
	B4	24,33	----

a: Ref.[59]

3.2.2 Band structures

The energy band diagram of the wurtzite and zincblende binaries are respectively shown in **Figures 3.6 and 3.7**. The graphs clearly indicate that, apart from zincblende AlN which is an indirect semiconductor, wurtzite AlN and InN in its two phases have a direct band gap.
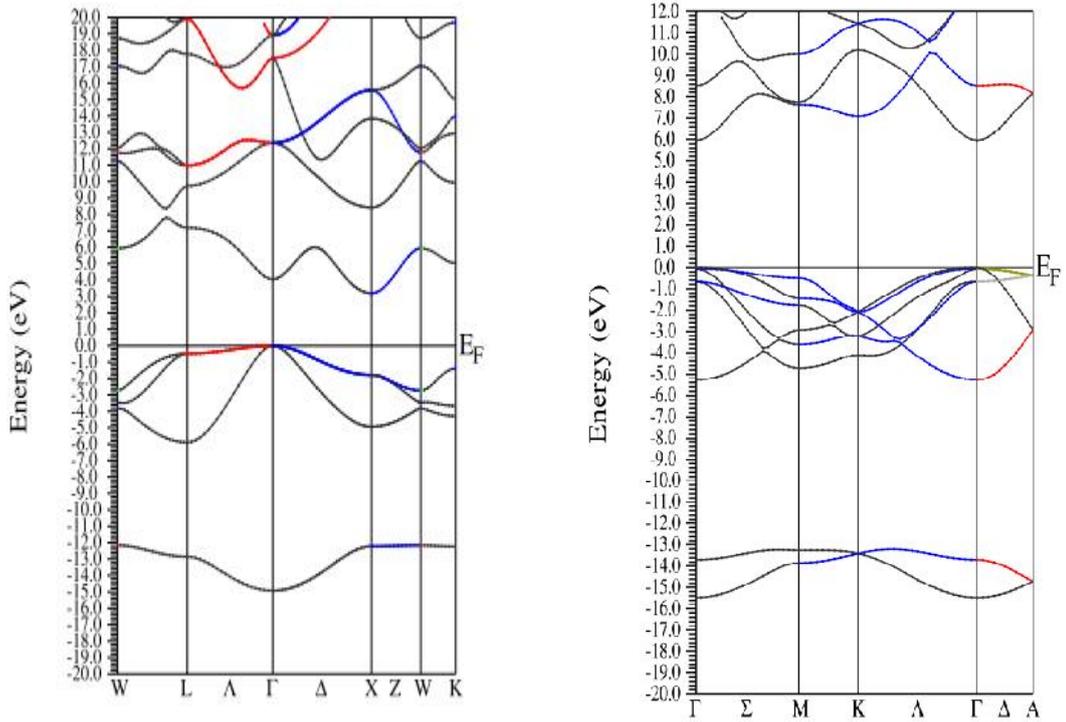
Figure 3.6 AlN band diagram: zincblende (left) wurtzite (right).
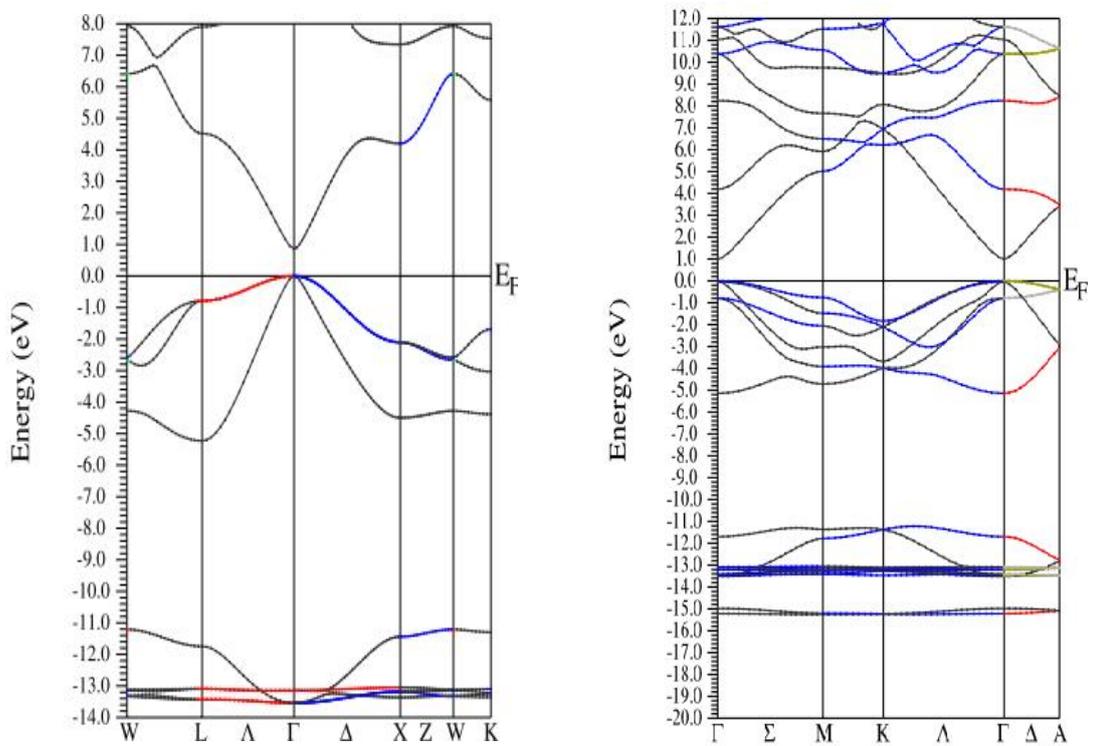
Figure 3.7 InN band diagram: zincblende (left) wurtzite (right).

a) Band gap

Two sets of calculations were carried out, the first one involving the main ambient phases (zb, wz) with Wien2k and TBM, the second one relating all phases with VASP.

The band gap calculated with TBM and DFT (Wien2k) at high symmetry points at several In compositions in zincblende phase, along with the available experimental and other works are respectively listed in **Table 3.4.** Experimental data being available for the binaries allows to draw some comparison. Zincblende AlN is found to be of indirect gap, the DFT (TBM) calculated gap values at Γ and X high symmetry points are respectively 5.60 eV (5.4 eV) and 5.03 eV (4.92eV), compared to 5.34 eV and 4.90 experimental/ab initio values while, on the other hand, zincblende structure InN is a direct semiconductor with DFT (TBM) gap value 0.86 eV(0.64 eV) compared with experimental value of 0.61 eV.

The wurtzite phase, in contrast, shows direct gap for both AlN and InN, with respective DFT (TBM) values of 5.95 eV (6.23 eV) and 0.99 eV(0.79 eV), compared to experimental values of 6.23 eV and 0.78 eV **[67]**. One has to note, at that point, that the indium band gap has long been overestimated at 1.7 eV it was not until 2001 that the correct value was reported.

When alloying AlN and InN the band gap remains indirect up to a crossover whose concentration value was found at x = 0.17 (TBM) and 0.10 (DFT) with a corresponding gap of 4.47 eV (4.95) in comparison to works of Liou et al. **[57]** who find a crossover at x=0.183 and a gap Eg=4.97 eV and Wang et al. **[68]** with at x = 0.18 and Eg=4.36 eV. The - and -X band gap variation with In for the wz and zb phases along with similar works are represented in **Figure 3.8**. The data was obtained with Wien2k where the work was mainly centered on obtaining the crossover point.

Table 3.4 Band gap of $Al_{1-x}In_xN$ in zincblende phase.

		AlN	$Al_{0.75}In_{0.25}N$	$Al_{0.50}In_{0.50}N$	$Al_{0.25}In_{0.75}N$	InN
TBM	$Eg^{\Gamma-\Gamma}$ (eV)	5.4	4.04	2.774	1.62	0.64
	$Eg^{\Gamma-X}$ (eV)	4.92	4.26	3.64	3.07	2.59
DFT-	$Eg^{\Gamma-\Gamma}$ (eV)	5.65	3.68	2.69	1.57	0.83
	$Eg^{\Gamma-X}$ (eV)	5.09	5.89	4.53	4.33	4.18
Others	$Eg^{\Gamma-\Gamma}$ (eV)	6.53[a], 5.4[b], 4.36[c], 4.25[d], 6.00[e], 6.03[m]	4.70[f], 3.61[m]	2.35[m]	2.20[f], 1.43[m]	0.53[a], 0.78[b], 0.0[d], 0.013[g], 0.73[h], 0.53[m]
	$Eg^{\Gamma-X}$ (eV)	5.63[a], 4.9[b], 2.50[i], 3.23[j], 3.16[d], 4.90[e], 4.87[m]	4.04[m]	3.48[m]	2.85[m]	2.51[b], 1.56[d], 2.81[j], 2.32[m]
Experiment		5.34[a]				0.7[i], 0.6[k], 0.7-1.1[l]

a: Ref. [47], b: Ref. [49],c: Ref. [48],d: Ref. [69],e: Ref. [70],f: Ref. [71],g: Ref. [72],h: Ref. [59],i: Ref. [73], k: Ref. [68],l: Ref. [50],

Table 3.5 Band gap of AlN, InN and their alloys $Al_{1-x}In_xN$ in rocksalt (B1), zincblende (B3) and wurtzite (B4) phases.

Composition x	Eg (eV)		
	E_g B1	E_g B3	E_g B4
0 TW	5.743	4.817	5.347
Exp.	----	5.34[a]	6.28[b], 6.23[c],
Others	5.42[d], 5.40[e]	4.09[d], 4.36[f]	4.26[d], 4.22[g],
0.25 TW	3.794	2.961	2.924
0.5 TW	2.037	2.044	1.794
0.75 TW	1.346	1.256	1.203
1 TW	0.800	0.595	0.782
Exp.		0.7[h], 0.6[i]	0.9[a], 0.78[c], 0.7[h]
Others	1.0[k]	0.53[a], 0.78[c], 0.73[l]	0.69[a], 0.90[l]

a: Ref. [47], b: Ref. [2], c: Ref. [49], d: Ref. [55], e: Ref. [57],f: Ref. [56], g: Ref. [58], h: Ref. [68]; i:Ref.[73], k: Ref. [47], l: Ref.[61],
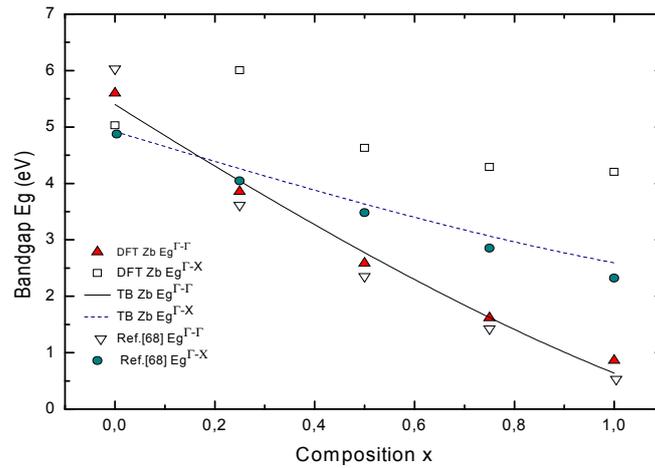
Figure 3.8 Band gap variation of $Al_{1-x}In_xN$ zincblende with In (TBM and DFT)

The - energy band gap, computed with Vasp, of $Al_{1-x}In_xN$ for all three phases Zb, Wz and Rs as a function of indium proportion is listed in **Table 3.5** and illustrated in **Figure 3.9**. The results confirm that AlInN has the largest spectrum compared to the other III-V semiconductors. For example the gap variation with In for the phosphides the antimonides and the arsenides are respectively **[**3.63, 1.42]; AlInSb [2.38, 0.23]; AlInAs [3.09, 0.41]eV. The results show that the band gaps are decreasing with In composition. They are varying from 5.74 to 0.80 eV for rocksalt which is shows the largest band gap range, from 4.81 to 0.59 eV for zincblende and from 5.34 eV to 0.78 eV for wurtzite. For a given In concentration (0<x<1) the Rs ,overall, appear to have the highest band gap, and the Wz the lowest one.
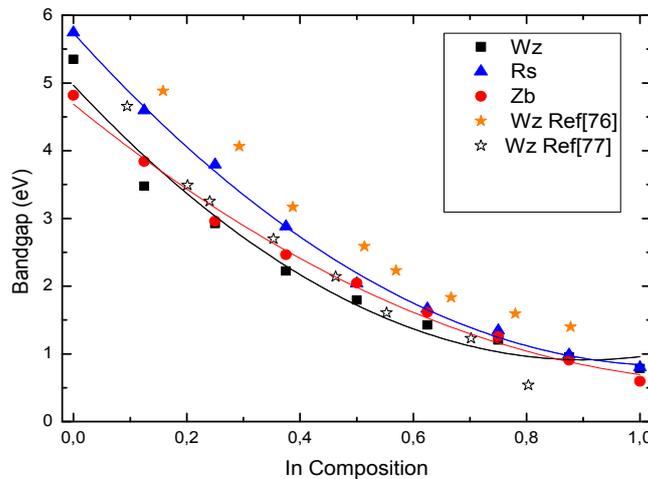
Figure 3.9 Band gap variation of $Al_{1-x}In_xN$ rocksalt, zincblende and wurtzite.

The energy band gap variation with In contents can be expressed as follows:

$$E_g(x) = xE_{g,AlN} + (1-x)E_{g,InN} + bx(1-x) \qquad (3.4)$$

where E_{gAlN} and E_{gInN} are respectively the band gap energy of InN and AlN and b the band gap bowing parameter for $Al_{1-x}In_xN$ ternary alloy. The obtained values of b are presented in **Table 3.6.**

Table 3.6 AlInN Band gap bowing parameter of zinc-blende, wurtzite and rocksalt

Phase	*bowing parameter This work*	*bowing parameter Others*
B3	2.83	2.5[a]
B1	4.37	----
B4:		
x=0.125	11.82	11.74 (x=0.13)[b]
x=0.25	6.80	8.12
x=0.50	5.07	5.15
x=0.75	3.85	4.24
x=0.875	3.61	3.87 (x=0.85)

a: Ref.[49],b: Ref.[82]

From Eq. (3.4) the bowing parameter is deduced as follows :

$$b(x) = \frac{\Delta E}{x(1-x)} \qquad (0 \le x \le 1) \qquad (3.5)$$

where $\Delta E = E_g^{alloy}(x) - (1-x)E_g^{AlN} - xE_g^{InN}$ represents the deviation from linearity.

b is considered composition dependent if its fluctuation around the mean value b_m is over 20% otherwise it is independent.

So since for usual concentration (0.25,0.5,0.75) : (x(1-x)) is roughly 0.2 and a small deviation from linearity for usual semiconductors is estimated at less than 0.2 eV (for small gap semiconductors it is much less) therefore the bowing factor should be considered small when its value is less than 1 eV.

As can be seen in **Table 3 6** the band-gap bowing parameter yielded by our calculations has a constant value for both B1 and B3 phases. Nevertheless, it depends on the alloy composition x for the B4 phase. A similar band-gap bowing parameter composition dependent has been reported in numerous works for the same material system of interest **[81,82,83,84,85,86,].**

In fact the bowing parameter strong dependence on In-composition is a general trend in all the In-containing nitride alloys. Physical explanation seem still in debate and there a number of theories regarding the cause among which: a large size mismatch between cation atoms **[83],** charge transfer contributions due to a large electronegativity differences between aluminum and indium atoms **[81,85],** localized electronic states **[82],** indium clustering **[84].**

Moreover, the composition dependence of the band gap bowing parameter has been reported for InGaN ternary semiconductor materials in the zincblende structure **[86,87]**. According to these authors, the dependence of the band gap bowing parameter on the alloy composition is traced back to the carrier localization effects. Furthermore, have also reported a composition dependence of the band gap bowing parameter in wurtzite InGaN **[88].** Besides, using DFT calculations, Schulz et al. **[89]** showed also that even a single In atom in wurtzite InAlN can introduce localized states in the material in question. They argue that this feature is responsible for the composition dependence of the band gap bowing parameter. As far as the

B1 and B3 phases are concerned in the present contribution, the physical reason for the non-dependence of the band-gap bowing parameter on the alloy composition x is not clear.

b) Effective mass

In addition to the band gap, the effective mass of electrons stand to be another significant physical parameters giving more insights as regards the electronic transport electronic devices engineering especially the newly HEMT's using AlInN active layers **[4].** The electronic mass calculation has been carried out using Effective mass calculator **EMC**) software (https://github.com/afonari/emc) which implements calculation of the effective masses at the bands extrema using finite difference method. The results are presented in **Table 3.7** with $m_{\parallel}$ and $m_{\perp}$ being the masses in the direction parallel and perpendicular to the c-axis, respectively. The obtained masses are, to some extent, heavier than the other In based III-V's. AlInN effective mass varies in the range **[**0.29, 0.05] compared to [0.22, 0.08] for AlInP [0.14, 0.014] for AlInSb and [0.15, 0.026] for AlInAs. Calculated values show reasonable agreement with experimental data and other theoretical works and a phase comparison reveals, overall, a lighter relative electron mass for the B4 structure and within this phase, independently of concentration, a smaller mass along the c-axis.

Plots of the calculated electron effective mass of $Al_{1-x}In_xN$ alloy, as a function of indium composition, for B1, B3 and B4 phases are illustrated in **Figure 3.10** where the B4 mass is taken as the mean mass value defined by $m^* = \sqrt[3]{m_{\parallel}m_{\perp}^2}$.

By observing Figure 3.9, the electron effective mass of rocksalt and zinc-blende structure seems to vary quite strongly with composition even in the low In content regime. This may affect the mobility of the carriers which in turn has an effect on the transport properties and hence on devices performance. On the other hand, a nearly constant value for the wurtzite effective mass at low In content is observed. This mass stability regarding fluctuation of

concentration could of interest for HEMT devices in which the In content that matches the lattice parameters between AlInN with GaN [3] is not steady but varies around 0.82.

Assuming that the electron effective mass versus alloy content x curve is quadratic, similarly to the band-gap energy, one defines an electron effective mass bowing parameter $b_m(x)$ by the relation,

$$m*(x) = (1-x)m*_g^{AlN} + x m*_g^{InI} + b_m(x) x(1-x) \tag{3.6}$$

Our findings regarding the electron effective mass bowing parameter for the three phases being considered here at various alloy concentrations x are listed in **Table 3.8**. Note that the electron effective mass exhibit small bowing parameters.

Since the electron effective mass is inversely proportional to the electron mobility, one may expect a contribution of the decrease of the electron effective mass in richer In ternary compounds to the increase of the mobility bearing in mind that this is not the only parameter that affects the electron mobility. As a matter of fact, the electron mobility is also affected by the alloy scattering and a deeper study should include the effects of disorder and eventual clustering in the AlInN alloying on scattering.
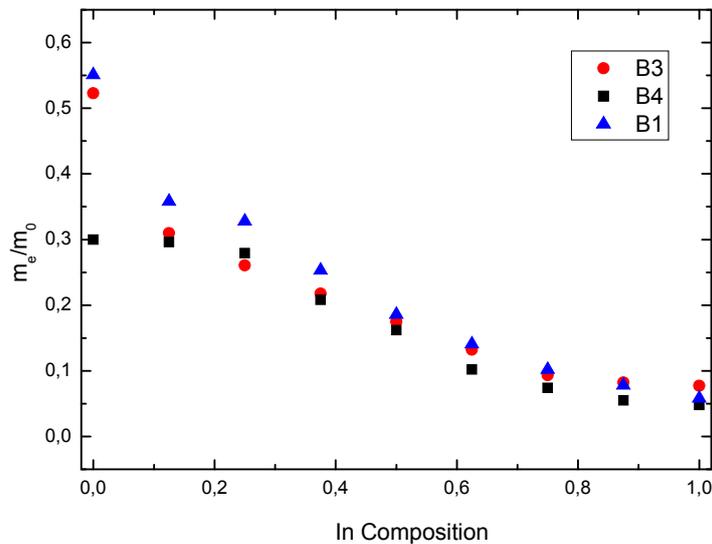
Figure 3.10 Electron effective mass of $Al_{1-x}In_xN$ zinc-blende and wurtzite (DFT).

Table 3.7 Electron effective masses m (in units of free electron mass m_0) of ternary $Al_{1-x}In_xN$ (B1, B3 and B4 phases).

Composition x				
0 TW	0.583	0.523	0.306	0.289
Exp.	----	----	0.29-0.45[a]	0.29-0.45
Others	----	0.32[g]	0.32[g], 0.321[d]	0.284[m]
0.25 TW	0.438	0.260	0.293	0.253
0.5 TW	0.202	0.174	0.169	0.151
0.75 TW	0.134	0.093	0.077	0.069
1 TW	0.096	0.077	0.049	0.046
Exp.	---	0.04[j]	0.07[a]	0.07[a]
Others	----	---	0.129[m]	0.089[m]

a: Ref. [47], d: Ref. [51], g: Ref. [58], j:Ref. [90], m: Ref. [76].

Table 3.8 Electron effective mass bowing factor

x	0.25	0.5	0.75
b (B1)	-0.124	-0.55	-0.447
b (B3)	-0.808	-0.504	-0.507
b (B4)	0.273	0.094	0.0386

3.2.3 Density of states

The number of states available per unit energy (density of states (DOS)) is an important factor in studying the electronic properties. The calculated total and partial density of states of zincblende and wurtzite are shown respectively in **Figures 3.11 a and b**. The vertical dashed line represents the Fermi level which is set to zero. It is clear that the density of states is higher in wurtzite phase than in zincblende phase. The upper energy valence bands range from -5 eV to 0 eV. The major contribution comes from the nitrogen atom for all compositions in the two phases. The p-orbital seems to bring all the contribution of nitrogen to the binaries. The lower conduction band of wurtzite phase extends continuously from the value of the gap up to about 15 eV with a similar contribution of all atoms either in wurtzite or zincblende phase. In the case of AlN, the p-orbital is prevalent while for InN, N and In, respectively, contributes through the p-and s-orbitals. The ternary compounds present in the case of wurtzite phase a continuous lower conduction band. However, there is a discontinuity for zincblende phase that seems to shift towards higher energies with augmenting indium content. In the case of the valence band we notice that the DOS peak increases with indium.

(a)   (b)   (c)
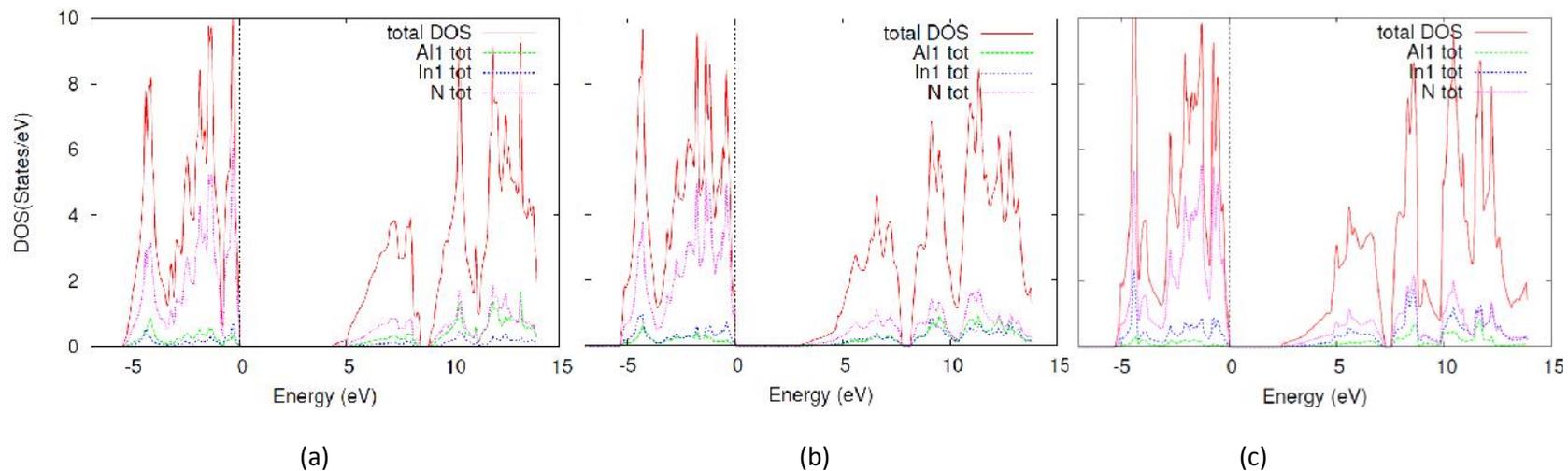
Fig. 3.11 a Total and partial density of states of zinc-blende$Al_{1-x}In_xN$: x=0.25 (a), 0.50 (b) and 0.75 (c).
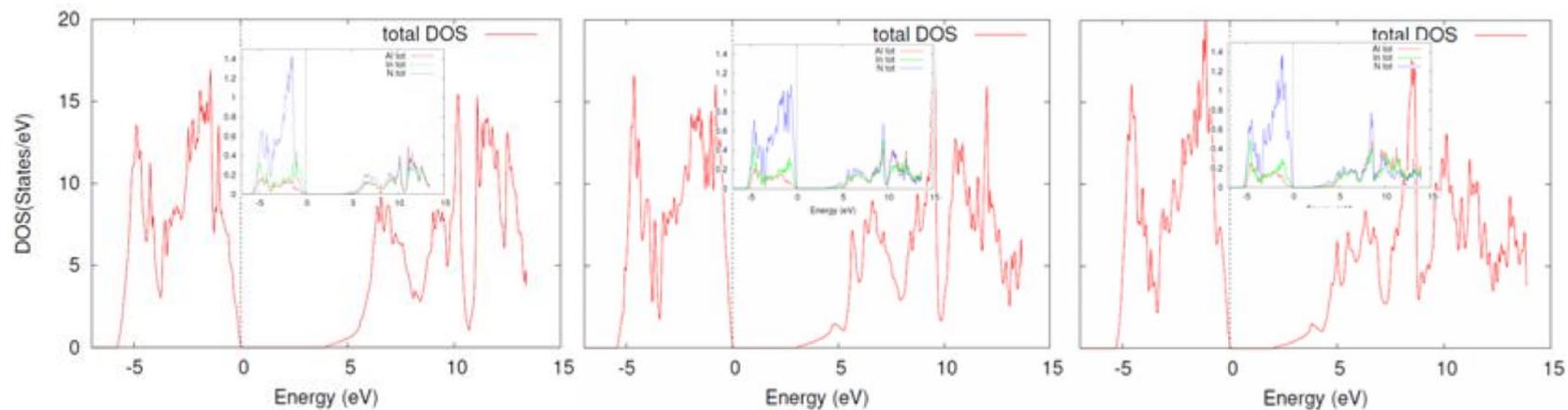
Fig. 3.11 b Total and partial density of states of wurtzite$Al_{1-x}In_xN$:x=0.25 (a), 0.50 (b) and 0.75 (c).

3.3 High Pressure effects and Phase transition

3.3.1 Introduction

High pressure studies of semiconductors have given valuable insights to their room pressure properties and have also been used to generate new phases. It is important to note that hydrostatic pressure acts as a perturbation on the electronic properties without a change of symmetry within a single, homogeneous phase. Accordingly, the changes in optical or electronic properties can be interpreted in a straightforward manner. Experimentally high pressure attracted attention from the Semiconductor Physics community after the discovery of William Paul's Empirical Rule **[91]**. The technique gained further momentum with the invention of the diamond-anvils high pressure cell.

Phase transitions of nitrides will help us to theoretically understand and in some cases even theoretically predict their properties. Nitrides are most commonly found in the wurtzite crystalline structure. The atoms in the wurtzite structure rearrange into the rocksalt structure when put under extreme high pressure. This phase transition is the one that we investigated for the nitrides.

There are two widely adopted techniques, called enthalpy comparison method, to investigate pressure-induced phase transition and identify stable phases. The first one is to optimize the total internal energy of some selected structures with respect to structural parameters at constant volume, and then construct in the same diagram total energy versus the volume per unit atom for each phase. From the common tangent (**F**igure **3.12**) one can extract the transition pressure.
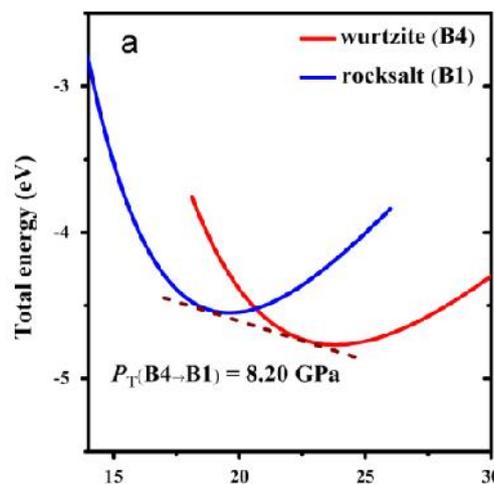
Figure 3.12 Typical energy-volume E(V) diagrams.

In the second method one plots the enthalpy of the various phases against the pressure and the intersect of the plot of two phases will provide the phase transition pressure (**Figure 3.13**).
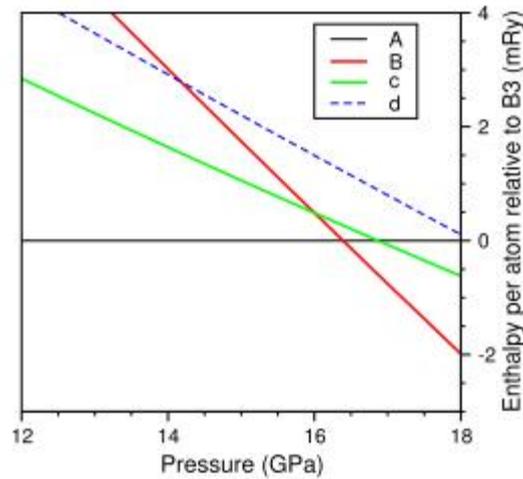
Figure 3.13 Enthalpy-pressure H(p) diagrams for four phases of ZnS material **[92]**.

3.3.2 Band gap variation

We will first begin with the study of the effects of pressure on the energy band gap of $Al_{1-x}In_xN$ in its B3 and B4 phases. The pressure are varied from tensile to compressive up to the transition phase pressure. Results show a linear increase of the gap for either phases (**Figures 3.14 a and 3.14 b**), with the slopes $\frac{dE_g}{dp}$ varying with In concentration from 36.8 meV/GPa (x=0) to 24.5 (x=1) for B4 and from 41.5 (x=0) to 29.5 meV/GPa (x=1) for B3. The magnitude of these slopes is typical of III-group nitrides which, due to their large ionicity,and independently of their phase, exhibit much lower band gap pressure coefficients than other III-V group compounds such as GaAs (117 meV/GPa) **[93]**. It is also expected that the pressure coefficient of the bandgap decreases with increasing indium composition as a consequence of the larger ionicity of InN with respect to AlN **[94].**
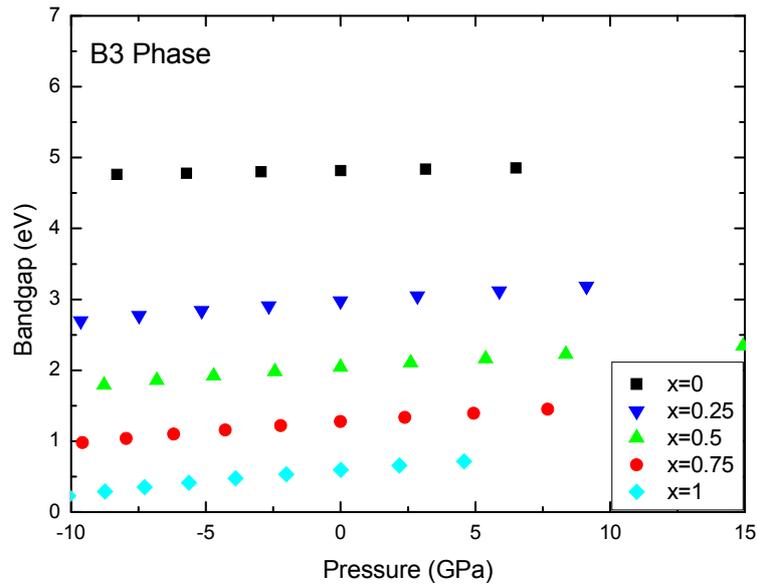
Figure 3.14a Band gap of $Al_{1-x}In_xN$ vs pressure B3:phase.
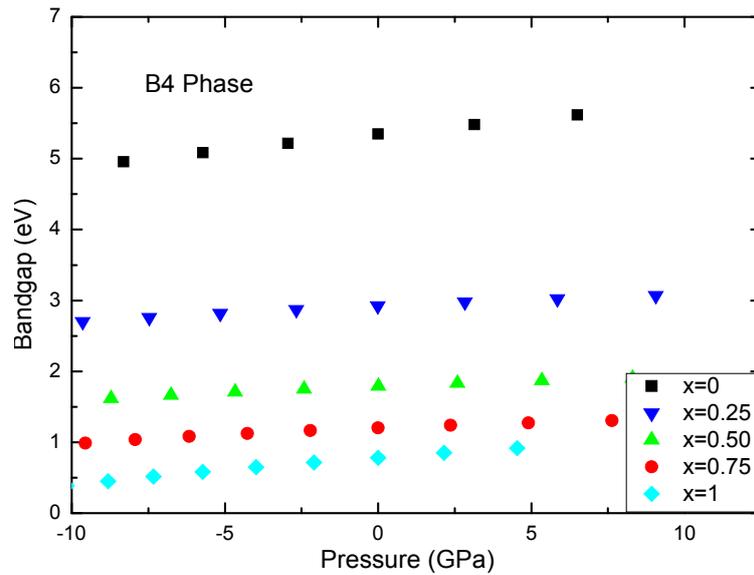
Figure 3.14b Band gap of $Al_{1-x}In_xN$ vs pressure B4 phase.

3.3.3 Phase transition pressure

Starting from a sequence of different volumes, calculation of the corresponding energies were carried out within PBEsol with the energy versus volume E(V) plot illustrated in **Figure 3.15**. Results show clearly that, B4 is the most stable phase structure independently

of In proportion, that B3 is slightly higher in ground state energy than B4, and that we may get phase transitions B4-B1 and B3-B1 for the entire proportions of In contents.
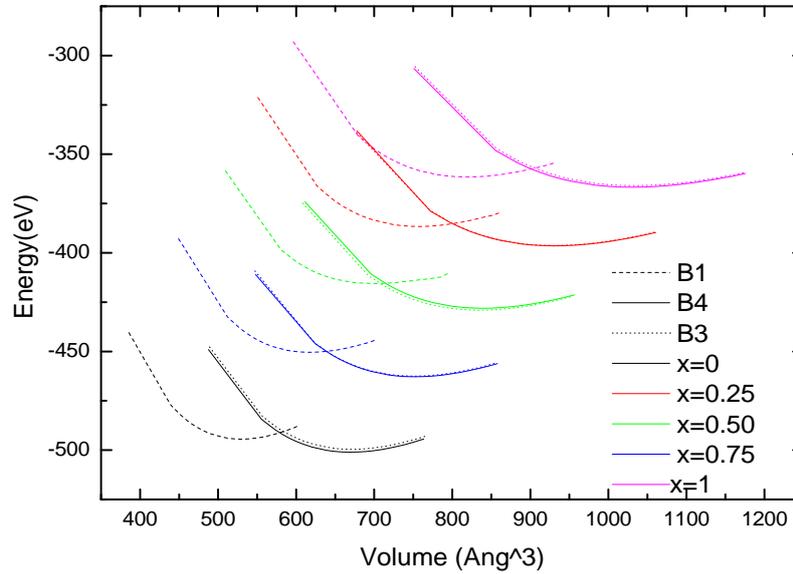
Figure 3.15 $Al_{1-x}In_xN$ total energy vs cell volume.

The phase stability is determined by the minimum of the Gibbs free energy G:

$$G = E + P.V - T.S \tag{6}$$

where E, P, V, T, S stand respectively for internal energy, pressure, volume, temperature and entropy. The Gibbs free energy reduces to enthalpy H $(H = E + P.V)$ given that calculations are made at 0°K. By using the obtained values for total energy and corresponding volume one can easily calculate the variation of enthalpy with pressure for each phase. The variation of the relative enthalpy difference of B4 and B3, for various In proportions, are plotted in **Figures 3.16(a, b)** with the phase transition pressures determined at the x-axis intersection of the various enthalpy curves (H=0).

The computed phase transition pressures are summarized in **Table 3.8** and plotted in **Figure 3.16**. The results show a structural phase transition varying, with dopant, from 4.02 (x=0) to 7.84 GPa (x=1) for B4-B1 transition and from 3.37 (x=0) to 6.02 GPa (x=1) for B3-B1 transition with a maximum value around 16 GPa for x=0.5.

Table 3.9 B4-B1 and B3-B1 phase transition pressures.

Composition x	Transition pressure of $Al_{1-x}In_xN$ (GPa)	
	B4-B1	B3-B1
0 TW	7.84	6.02
Others	12.5[a], 9.2[b]	7.1[b]
Exp.	14,20[c]	
0.25 TW	15.015	14.69
0.5 TW	15.194	16.94
0.75 TW	9.608	9.456
1 TW	4.024	3.37
Others	13.4[d],4.93[e],11.1[b]	10.5[b]
Exp.	11.6[b]	

a: Ref. [95], b: Ref. [64], c: Ref. [65], d: Ref. [96], e: Ref. [97]
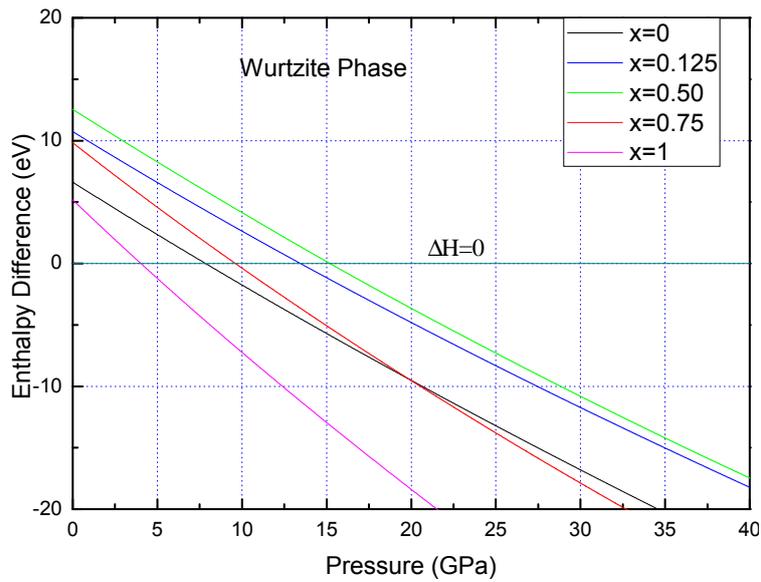
Figure 3.16a B4- B1 $Al_{1-x}In_xN$ enthalpy difference
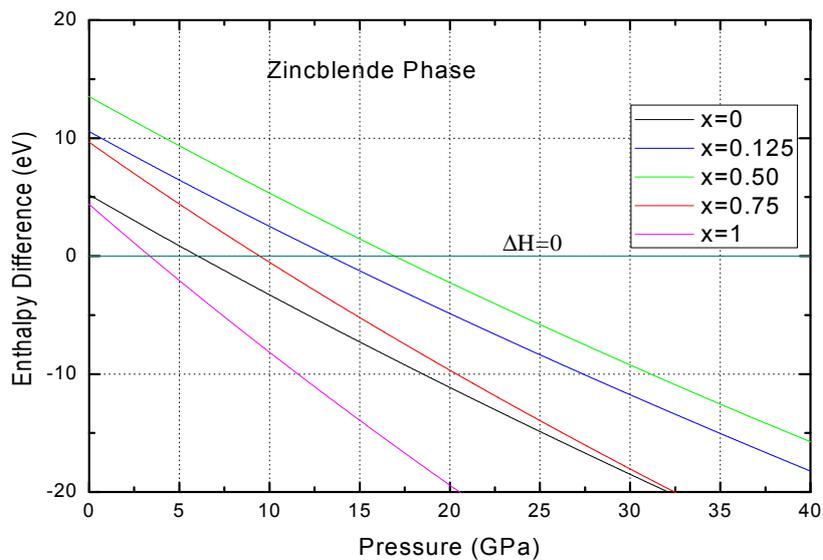
Figure 3.16b B3- B1 $Al_{1-x}In_xN$ enthalpy difference.
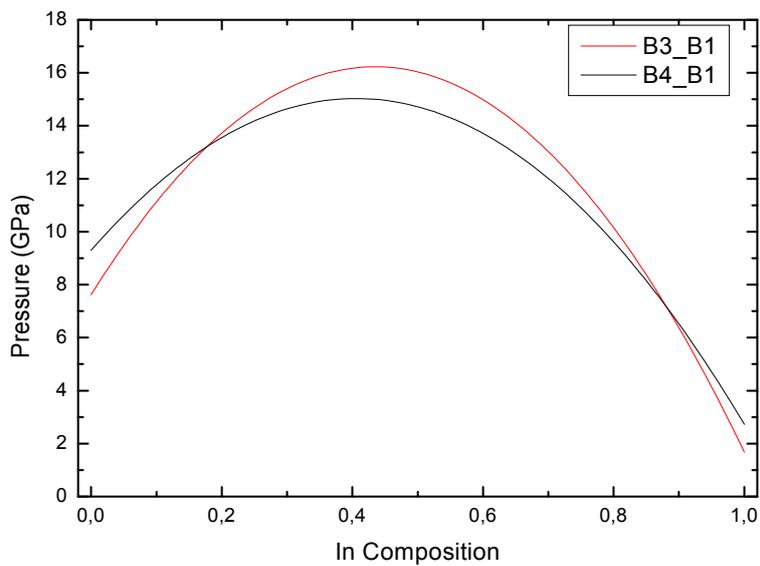
Figure 3.17 Phase transition pressure vs In composition.

CHAPTER 4

STRAIN EFFECTS

AND

APPLICATION TO AN ELECTRONIC DEVICE

4.1 Introduction to the origin of strains

In the growth process the AlInN films are deposited on a substrate, the difference in the lattice structure parameters results in strain effects which in itself has a great influence on the structural and therefore to the physical properties of the alloy. The following study deals with the effect of depositing a AlInN film on a GaN substrate, this kind of substrate being chosen ahead of studying a device based on this type of heterostructure.

Prior to the study of an electronic device, we analyze the physics of a layer deposited on a substrate. We will try to see the effects of the mismatch of the lattice parameters of two compounds as well as the change of the physical properties due to the mismatch.

If we consider that the first few layers of the AlInN film are affected by the substrate and that mainly the bond length and the angles are changed within the process, the first direct effect will be the change in lattice parameters of AlInN compound causing a whole new energy band diagram. Thereof the band gap and the electronic effective mass will modify and hence the semiconducting properties of the compound will be affected.

4.2 Theory of Strain

Consider the two materials A and B shown in **Figure 4.1(a)**. These two materials have an obvious lattice mismatch, and this is the case to be found in all the nitride materials considered in this work. Due to this lattice mismatch, strain effects will be present in any heterostructures made from these materials. This is obvious if one considers growing an epilayer of material B on a substrate of material A, as is shown in **Figure 4.1(b)** The atoms of B are forced to align themselves with those of A with the in-plane lattice constant of B matching that of A, and thus the epilayer will be under biaxial compression. As a result of this, the epilayer of B expands along the growth direction by taking the shape of substrate A (a_s) and changes in the normal direction , such that, instead of being described by one lattice constant a, B is now described by a_s and a_r such that $a_r > a > a_s$.

For a sufficiently thin epilayer we can assume that all the strain is incorporated in the layer. The net strain in the layer plane is given by;

$$\epsilon_\parallel = \epsilon_{xx} = \epsilon_{yy} = (a_s - a_l)/a_l \tag{4.1}$$

The strain in the epilayer along the growth direction $\epsilon_\perp$ is given by:

$$\nu_{\perp} = -\frac{2\dagger}{1-\dagger}\nu_{\parallel} \dots\dots\dots\dots\dots\dots\dots\dots\dots\dots\dots\dots\dots\dots\dots\dots\dots(4.2)$$

where   is Poisson coefficient.
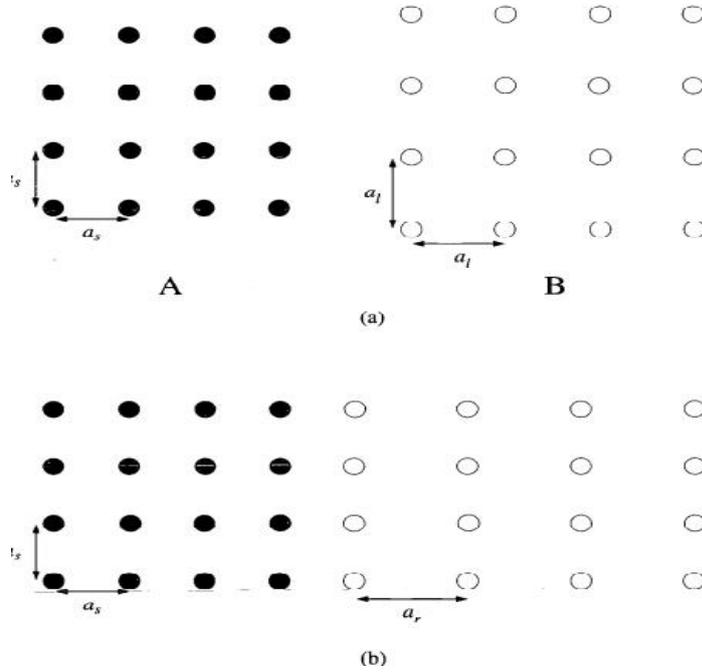
Figure 4.1 Lattice modification under strain

4.3 Strain effect on the electronic band structure

If we consider that only the first few layers of the AlInN film are affected by the substrate and that mainly the bond length and the angles are changed within the process, the first direct effect will on the energy band diagram of AlInN. In order to calculate electronic structure, one has first to calculate or measure the position dependent strain tensor ν_{rs} .

The basic approach to calculating such strains is Harmonic continuum elasticity: Here, one uses classical elasticity within the harmonic approximation, to compute the theoretical variation on the geometry of the unit cell:

For a cubic system, the strain energy per atom, E_{CE} **[98]** is:

$$E_{CE} = \frac{V}{2}C_{11}(\nu_{xx}^2 + \nu_{yy}^2 + \nu_{zz}^2) + \frac{V}{2}C_{44}(\nu_{xy}^2 + \nu_{yz}^2 + \nu_{zx}^2) + VC_{12}(\nu_{xx}\nu_{zz} + \nu_{yy}\nu_{xx} + \nu_{zz}\nu_{yy})$$

'4.3)

where V is the equilibrium volume, C_{ij} are cubic elastic constants, and v_{rs} the strain tensor.

In the absence of shear strain, for a film coherently grown on a substrate with parallel lattice constant a_s, the strain components are:

$$v_\parallel = v_{xx} = v_{yy} = \frac{a_s - a_{eq}}{a_{eq}} \qquad\qquad v_\perp = v_{zz} = \frac{c - a_{eq}}{a_{eq}} \tag{4.4}$$

where a_{eq} is the equilibrium lattice constant of the unstrained material and c is the perpendicular lattice constant of the strained film. The equilibrium value of this c axis is determined from: $\dfrac{\partial E_{CE}}{\partial v_\perp} = 0$

yielding **[92]**:

$$\frac{c_{eq}(a_s, G)}{a_{eq}} - 1 = (2 - 3q(G))v_\parallel(a_s) \tag{4.5}$$

where the 'epitaxial strain reduction factor' for orientation G of the c axis is

$$q(G) = 1 - \frac{B}{C_{11} + x(G)\Delta}$$

and $\Delta = C_{44} - \dfrac{1}{2}(C_{11} - C_{12})$ is the elastic anisotropy,

$B = \dfrac{2}{3}(C_{11} + 2C_{12})$ is the bulk modulus,

and $x(G)$ is a purely geometric factor given in**.**

For principal directions, $x(001)=0$, $x(011)=1$, $x(111)=4/3$. Equations 4.4 and 4.5 are used routinely to predict tetragonal distortions of strained films.˙

In the case of an hexagonal structure as in wurtzite **[99]:**

$$v_\parallel = v_{xx} = v_{yy} = \frac{a_s - a_{eq}}{a_{eq}}$$

$$c = c_{eq}(1 - 2\frac{C_{13}}{C_{33}}v_{xx}) \tag{4.6}$$

$$\mathsf{V}_z = \frac{c - c_{eq}}{c_{eq}}$$

Thus the growth of both the zincblende or wurtzite AlInN structures on a GaN substrate yields a tetragonal structure whose basal parameter corresponding to the substrate (GaN) lattice parameter and the perpendicular parameter given by equations 4.6.

The computed lattice parameters of the resulting tetragonal structure are listed in **Table 4.1**. The basal parameter a is that of the substrate i.e. $a=a_{GaN}=3.189$ Ang, while c_{wz} and c_{zb}, correspond respectively to the perpendicular parameters of the former wurtzite and zincblende structures.

Table 4.1 Perpendicular lattice parameter of the tetragonal strained structure

	AlN	$Al_{0.75}In_{0.25}N$	$Al_{0.50}In_{0.50}N$	$Al_{0.25}In_{0.75}N$	InN
C_{zb} *(Ang)*	2.062	1.856	1.618	1.333	0.976
C_{wz} *(Ang)*	4.913	5.204	5.543	5.964	6.535

4.3.1 Calculation of strain by the Tight Binding method

The modification of the bonding length and cell parameters owing to the strain means that the TB matrix elements $H_{lR,mR}$ differ from those of the unstrained bulk material. In the following the bulk matrix elements of the unstrained structure are denoted by $H^0_{lR,mR}$. We consider here only scaling of the inter-site matrix elements, for which, in general, a relation:

$$H_{lR',mR} = H^0_{lR',mR} f(d^0_{R'-R}, d_{R'-R}) \tag{4.7}$$

is expected, where $d^0_{R'-R}$ and $d_{R'-R}$ are the bond vectors between the atomic positions of the unstrained and strained material, respectively. Since the atomic-like orbitals of TB models are typically orthogonalized Löwdin orbitals, it might be that the diagonal matrix elements, too, vary in response to displacements of neighboring atoms [100]. However, Priester et al. [101] achieved a very accurate band structure description in the framework of a spin-orbit dependent sp3s* TB model without adjusting the diagonal matrix elements. Therefore, we consider here only scaling of the inter-site matrix elements. The function $f(d^0_{R'-R}, d_{R'-R})$ describes, in general, the influence of the bond length and the bond angle on the inter-site

(hopping) matrix elements. Here we use the relation: $f(d^0_{R'-R}, d_{R'-R}) = (d^0_{R'-R} / d_{R'-R})^2$. This corresponds to Harrison's d^{-2} rule **[100],** the validity of which should be a reasonable approximation.

The bond angle distortions can exactly be included in a TB model and the directional cosines between the different atomic orbitals are calculated according to the strain-induced displacements of the different atoms. With this so-called d^{-2} ansatz, the new interatomic matrix elements $H_{lR,mR}$ are given by:

$$H_{lR',mR} = H^0_{lR',mR} \left[\frac{d^0_{R'-R}}{d_{R'-R}} \right]^2 \qquad (4.8)$$

Taking into account all these facts the energy band diagram of a unstrained and strained AlInN film for x=0.75 is presented in **Figure 4.2**.(wurtzite) and **Figure 4.3** (zincblende). For this particular indium concentration we notice a slight change in the band gap and a rather appreciable variation of the conduction band shape between enlarged to squeezed depending on the phase (wurtzite or zincblende) and therefore a consequent change in the electron effective mass.
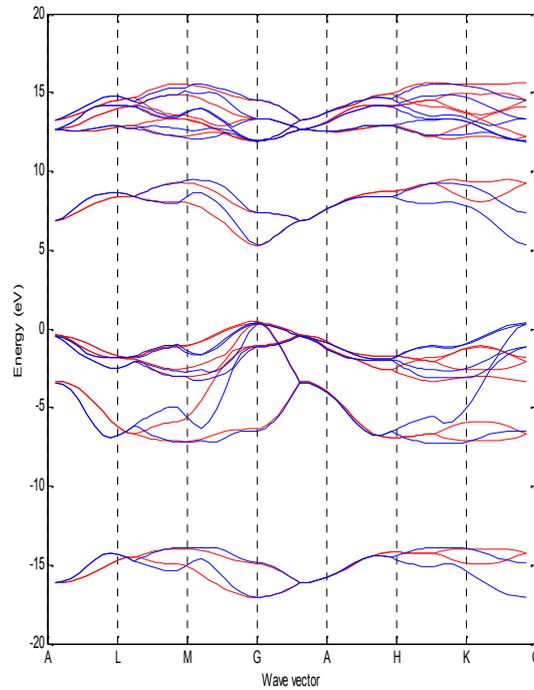
Figure 4.2 Unstrained (blue) and strained (red) $Al_{0.75}In_{0.25}N$ wurtzite band diagram (TBM)
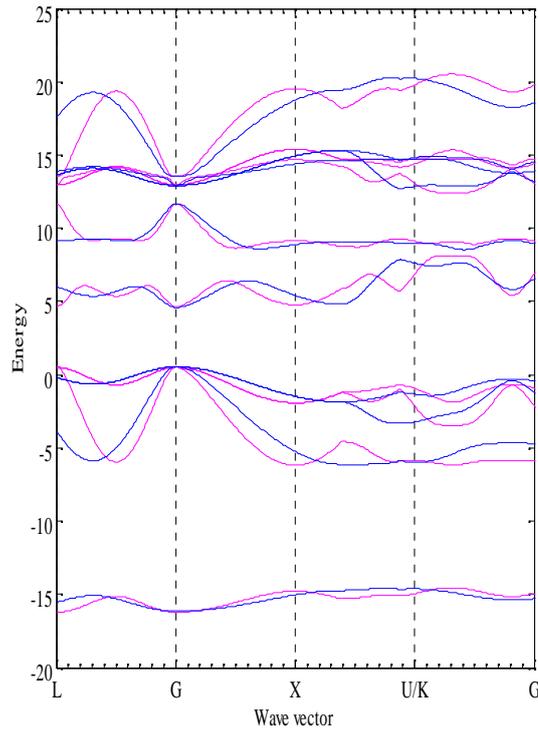
Figure 4.3 Unstrained (blue) and strained (red) $Al_{0.75}In_{0.25}N$ zincblende band diagram (TBM)

The band gap is extracted from the band energy diagram for various In concentration x and its variation with x is plotted in **Figure 4.4**. Below the matching concentration the strained mass is lower than the unstrained one whereas the trend reverses for higher In contents. The variation is quasi-linear since constant basal parameter dictates all the stress variation.
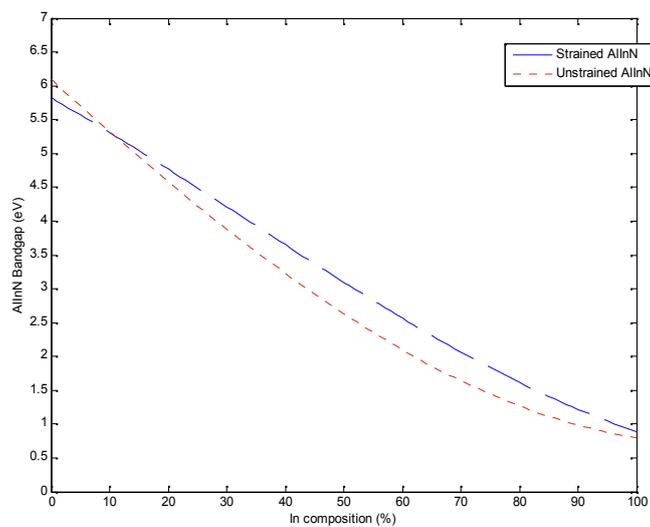
Figure 4.4 Band gap variation of strained and unstrained $Al_x In_{1-x}N$ with In proportion

4.3.2 Computation of strain effects by DFT

The strain results in a deformation of the wurtzite cell, leading to a tetragonal structure. All calculation have been made using 16 atom supercell with the new atom positions determined by equations 4.6 and 4.7.

As previously we used a PBEsol exchange correlation function with the remaining Wien2K tuning parameters similar to the unstrained case. **Figure 4.5 and 4.6** represent respectively the energy band diagram of unstrained and strained $Al_{0.75} In_{0.25}N$ in wurtzite and zincblende form;

We notice a for the wurtzite diagram a widening inthe shape of the lower conduction band and a narrowing of the band gap. Moreover the degeneracy is lifted for the higher valence bands. The same observation is valid for zincblende where the lowering on the lowest CB is more severe than in the other CB bands.
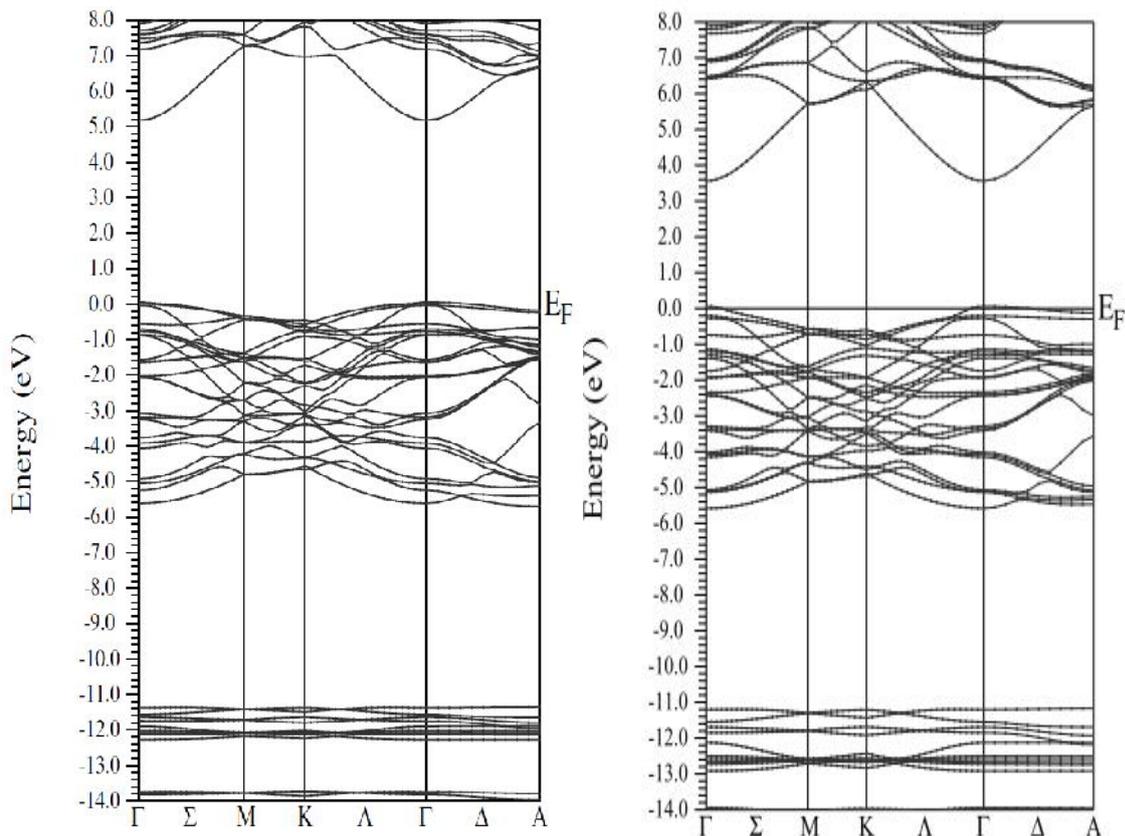
Figure 4.5 Energy band diagram (DFT) $Al_{0.75} In_{0.25}N$ (wz). left: unstrained right: strained
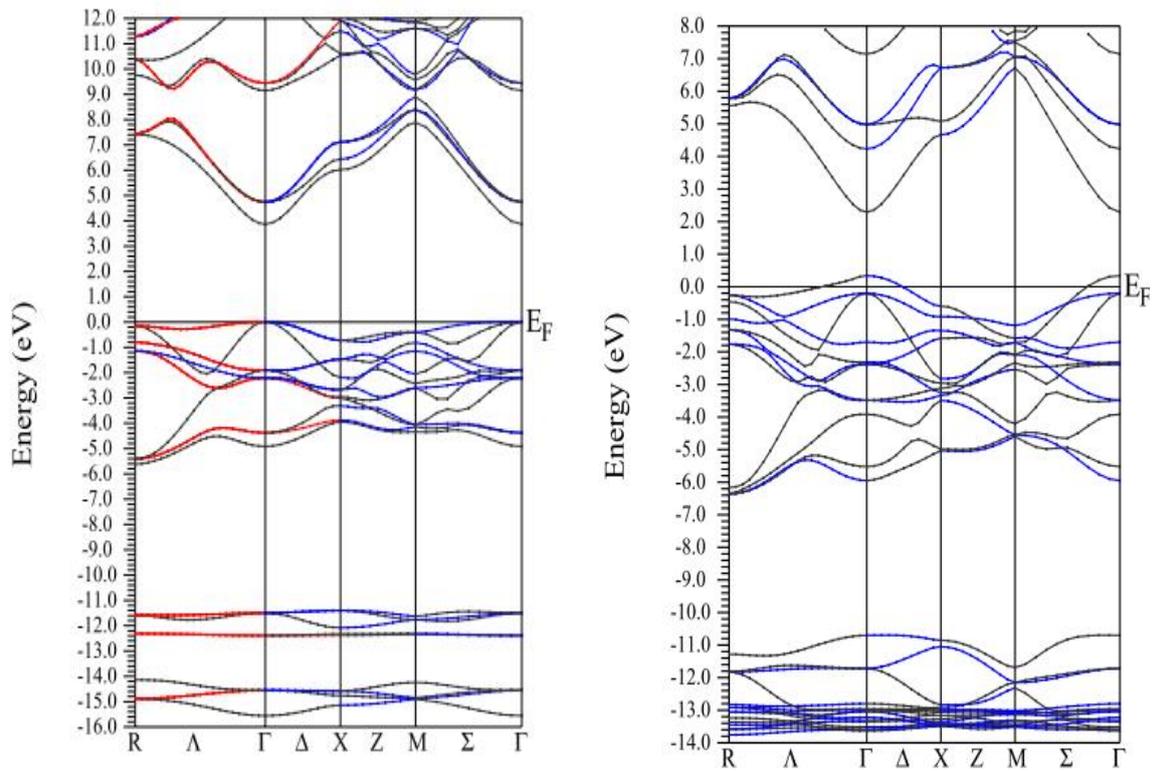
Figure 4.6 Energy band diagram (DFT) $Al_{0.75}$ $In_{0.25}$N (zb). left: unstrained, right: strained

The data extracted from these band diagrams are reported in **Table 4.2** for the energy band gaps and in **Table 4.3** for the electron effective mass.

Table 4.2 Calculated band gap for strained and unstrained AlN, InN and their alloys $Al_{1-x}In_xN$ in wurtzite phase

	AlN	$Al_{0.75}In_{0.25}N$	$Al_{0.50}In_{0.50}N$	$Al_{0.25}In_{0.75}N$	InN
TB unstrained	6.231	4.303	2.656	1.448	0.790
TB strained	5.825	4.492	3.097	1.833	0.879
DFT unstrained	5.950	3.769	2.802	1.786	0.998
DFT strained	5.238	3.368	3.175	2.145	1.523
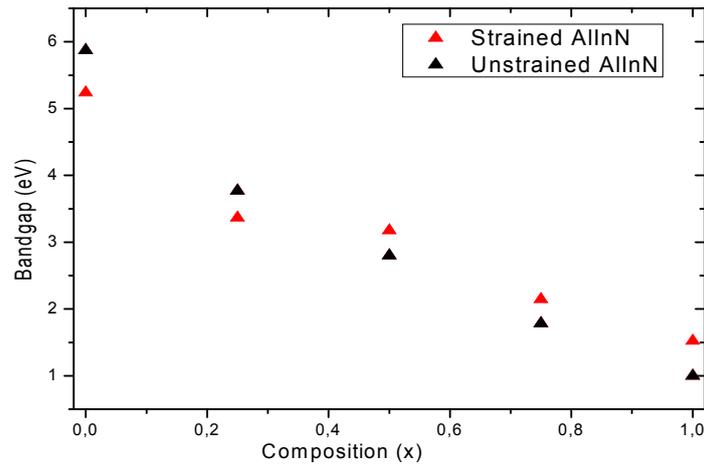
Figure 4.7 Band gap of unstrained and strained wurtzite AlInN versus In composition

We notice in **Figure 4.7** as expected a decrease of the gap with In with a change in the relative value or the strained and unstrained at the concentration at which the lattice parameter of the $Al_x In_{1-x}N$ turns out to be greater than that of GaN. The strain modulates the range of gap causing a modification in eV from [6.23, 0.79] to [5.82, 0.88].

Table 4.3. Electron effective masses *TBM* and *DFT* calculations for strained and unstrained AlN, InN and their alloys in wurtzite phase.

		AlN	$Al_{0.75}In_{0.25}N$	$Al_{0.50}In_{0.50}N$	$Al_{0.25}In_{0.75}N$	InN
TB unstrained	m^e/m^o	0.321	0.259	0.194	0.127	0.054
TB strained		0.294	0.257	0.215	0.166	0.113
DFT unstrained	m^e/m^o	0.306	0.293	0.169	0.077	0.049
DFT strained		0.300	0.209	0.196	0.185	0.141

Figures 4.8 and 4.9 show the variation of the electron effective mass, obtained respectively by TBM and DFT, with In concentration

Both methods show decreasing mass with In proportion. Above around 25% strained mass raises with respect to the unstrained one the difference of which increases with In. What is noticeable in the short interval centered on x=0.18, our zone of interest, is that the strain causes a smaller electron effective mass contributing positively to the electron mobility.
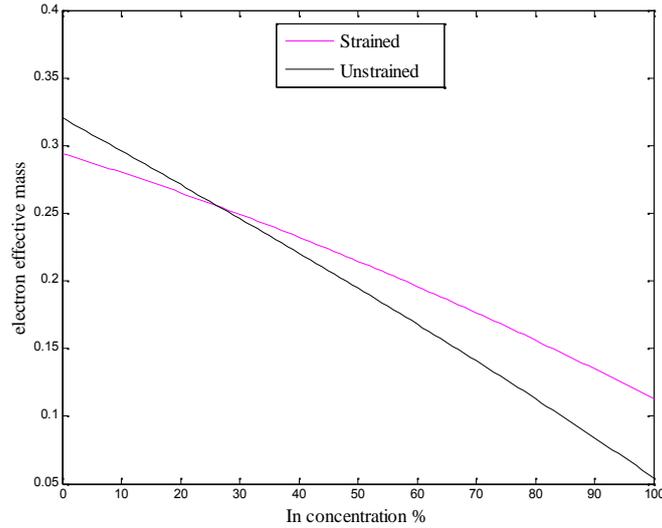
Figure 4.8 Electron effective mass of unstrained and strained AlInN versus In composition (TB)
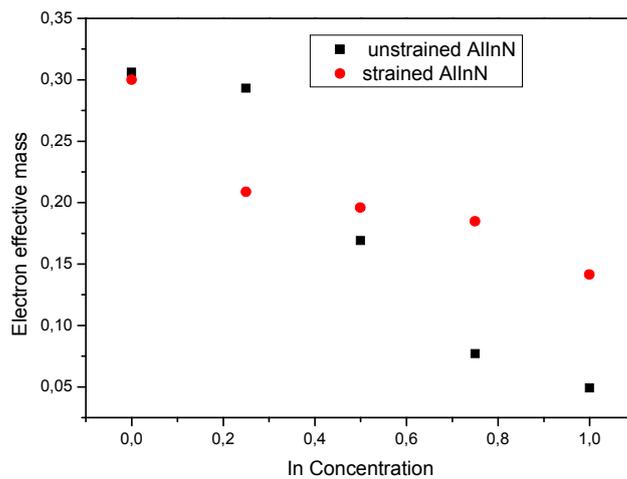
Figure 4.9 Electron effective mass of unstrained and strained AlInN versus In composition (DFT calculation)

4.6 Polarization effects

4.6.1 Theoretical framework

Piezoelectricity is a charge that accumulates in certain solid materials (such as crystals certain ceramics and biological matter) in response to applied mechanical stress.

The piezoelectric effect arising from stress-occurs in crystals that lack a center of inversion. A piezoelectric potential can be created in any bulk or nanostructured semiconductor crystal having non central symmetry, such as the Group III–V and II–VI materials, due to polarization of ions under applied stress and strain. This property is common to both the zincblende and wurtzite crystal structures. The semiconductors where the strongest piezoelectricity is observed are those commonly found in the wurtzite structure, i.e. GaN, InN, AlN and ZnO.

The polarization is related to stress through the piezoelectric tensor by the relation:

$$P_{pz} = e_{ij} v_j \tag{4.9}$$

where e_{ij} is the piezoelectric coefficients and v_j the strain tensor.

For zincblende semiconductors, the piezoelectric tensor only has one non vanishing tensor element e_{14}, and the polarization induced by strain is then given by:

$$\begin{bmatrix} P_x \\ P_y \\ P_z \end{bmatrix} = \begin{bmatrix} 0 & 0 & 0 & e_{14} & 0 & 0 \\ 0 & 0 & 0 & 0 & e_{14} & 0 \\ 0 & 0 & 0 & 0 & 0 & e_{14} \end{bmatrix} \begin{bmatrix} v_{xx} \\ v_{yy} \\ v_{zz} \\ v_{yz} \\ v_{zx} \\ v_{xy} \end{bmatrix} \tag{4.10}$$

Because of the special form of the piezoelectric tensor, only the shear strain generates the piezoelectricity. Hence a biaxial strain does not generate piezoelectricity in zincblende semiconductors grown on (001) direction, whereas this effect is largest along the (111) axes, since the anions and cations are stacked in the (111) planes.

On the other hand in strained wurtzite structures along or perpendicular to c-axis, a piezoelectric polarization will appear given by:

$$\begin{bmatrix} P_x \\ P_y \\ P_z \end{bmatrix} = \begin{bmatrix} 0 & 0 & 0 & 0 & e_{15} & 0 \\ 0 & 0 & 0 & e_{15} & 0 & 0 \\ e_{31} & e_{31} & e_{33} & 0 & 0 & 0 \end{bmatrix} \begin{bmatrix} \vee_{xx} \\ \vee_{yy} \\ \vee_{zz} \\ \vee_{yz} \\ \vee_{zx} \\ \vee_{xy} \end{bmatrix}$$

(4.11)

where the piezoelectric tensor e presents three nonzero coefficients e_{31}, e_{33} and e_{15}.

For strained III–V nitride epitaxial layers grown in the [0001] orientation, a piezoelectric polarization will be present aligned along the [0001] direction and given by:

$$P_{pz} = e_{31}(\vee_{xx} + \vee_{yy}) + e_{33}\vee_{zz}$$

(4.12)

In addition to piezoelectric polarization, among III-V semiconductors, III-V nitrides show a property, consisting of a built-in electric field, called spontaneous polarization (Psp). The materials showing this property are called pyroelectric.

Spontaneous polarization is an intrinsic property related to the bonding nature of the material, whose origin can be attributed to the fact that the geometric center of the negative charges (electrons) in the solid does not coincide with the center for the positive charges (nuclei). Another way to express this concept is to think that, in the pyroelectric, the bonds connecting the atoms with their first neighbors are not equivalent, i.e., one of these bonds has a more (or less) ionic nature when compared to the others. Tetrahedrally coordinated semiconductors with cubic structure have four equivalent bonds and due to this symmetry the center of the electronic charge belonging to an atom coincides with the nucleus position.. This intuitive picture shows why elemental semiconductors (Si, C, Ge) and zincblende-structure semiconductors, such as most of the III-V and II-VI semiconductors, do not show a Psp .

However, the Psp can arise in some cubic semiconductors by the effect of alloying. In the case of InGaP alloys **[102],** materials formed by the substitution of a certain amount of In atoms at the Ga sublattice sites of a zincblende GaP crystal, the bond distortion induced by the atomic size mismatch between Ga and In, can induce a break in the symmetry among the four bonds of the tetrahedral structure. The ensuing polarization must be called Psp since it is shown in the equilibrium structure of the alloy: this effect is fairly relevant in III-N alloys.

On the other hand, lower symmetry crystals, such as hexagonal structure semiconductors, having a bond oriented in the [0001] direction longer from the other ones, show the existence of an asymmetry in the bonding. This difference in ionicity leads to the center of the electron charges being displaced along the [0001] direction (the pyroelectric axis direction).

The Modern Theory of Polarization (MTP) **[103],** sometimes referred to as Berry's phase method, provides an easy and accurate way to compute Psp. Within MTP the calculation of Psp is performed using first-principles computational tools and does not require a previous experimental knowledge about the material structure.

4.6.2 Polarization effect on AlInN layer grown on a bulk GaN

Since, as previously mentioned, the cubic binaries do not show any kind of spontaneous polarization, we will concentrate for the remaining part of this study on the wurtzite case.

In the case of a biaxial strain on a AlInN layer grown on a GaN buffer the piezoelectric polarization takes the following expression:

$$P_{piezo}^{Al_{1-x}In_xN}(x) = 2(e_{31}(x) - e_{33}(x)\frac{C_{13}(x)}{C_{33}(x)})v_{xx}(x) \tag{4.13}$$

where the piezo-coefficient e_{ij} and elastic parameter C_{ij} are given by Vegard's law:

$$e_{ij}^{Al_{1-x}In_xN} = (1-x)e_{ij}^{AlN} + xe_{ij}^{InN} \tag{4.14}$$

$$C_{ij}^{Al_{1-x}In_xN} = (1-x)C_{ij}^{AlN} + xC_{ij}^{InN} \tag{4.15}$$

and the AlInN/Gan biaxial strain v_{xx} is determined by equation 4.6 .

whereas the spontaneous polarization takes the form

$$P_{sp}^{Al_{1-x}In_xN}(x) = (1-x)P_{sp}^{AlN} + xP_{sp}^{InN} + bx(1-x) \tag{4.16}$$

here b is the spontaneous polarization bowing factor. Its computed value given in the literature **[104]** is: $b_{PspAlInN} = 0.071$ Cm^{-2}

The values of the binaries AlN and InN spontaneous polarization and piezoelectric coefficients e_{31} and e_{33} used in this work, are presented in **Table 4.4.**

Table 4.4 Piezoelectric constants and spontaneous polarization of nitrides binaries **[104,105]**

Parameters	AlN	InN	GaN
$e_{31}(Cm^{-2})$	-0.58	-0.412	-0.55
$e_{33}(Cm^{-2})$	1.55	0.815	1.12
P_{sp} (Cm^{-2})	-0.09	-0.042	-0.034

The resulting values of piezoelectric and spontaneous polarization for are listed in **Table 4.5,** with their variation with In concentration plotted in **Figure 4.10.** The plot shows the decrease of the piezoelectric polarizations with In concentration due to decreasing strain to finally cancel in the matching of lattice parameters of the AlInN and the GaN substrate (proportion x=0.18). Obviously the P_{piezo} rises again with strain but reverses to take the same direction of Psp . The spontaneous polarization, on the other side, shows a slow decrease over the concentration range, and at high In concentration P_{piezo} will be minor with respect to Psp.

Table 4.5 Piezoelectric and spontaneous polarization of $Al_{1-x}In_xN$ vs In composition

x	0	0.25	0.5	0.75	1
P_{sp}	-0.0900	-0.0647	-0.0483	-0.0407	-0.0420
P_{pz}	0.0484	-0.0191	-0.0807	-0.1378	-0.1930
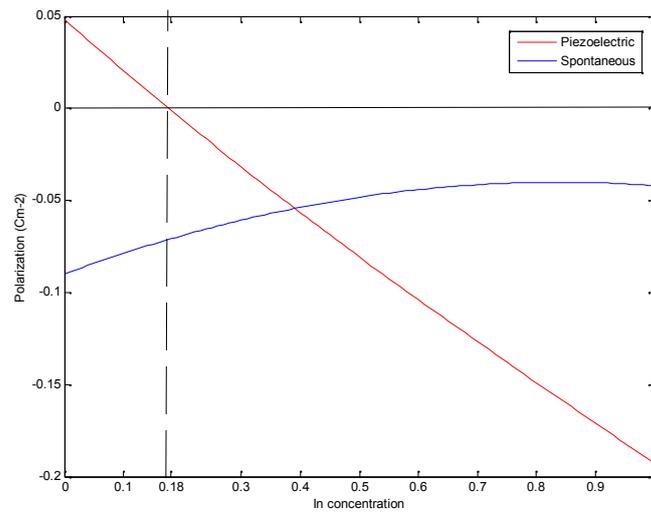
Figure 4.10 $Al_{1-x}In_xn$ Spontaneous and Piezoelectric polarization vs In concentration

4.7 Application to an electronic device :The HEMT

4.7.1 Introduction

The High Electron mobility Transistor HEMT (also known as MODFET), is a field effect transistor consisting of a heterostructure of two different gap semiconductors. A commonly used material combination is GaAs with AlGaAs, though there is wide variation, dependent on the application of the device. Devices incorporating more indium generally show better high-frequency performance, while in recent years, gallium nitride HEMTs have attracted attention due to their high-power performance. GaN based HEMT have the ability to operate at high frequencies are used in high power devices such as radars, satellite TVs, cell phones voltage converters. Nitride HEMTs traditionally use a heterogeneous AlGaN / GaN structure with a n-doped large band n type AlGaN donor delivery layer and an undoped GaN narrow band gap channel layer. The heterojunction created by different band gaps materials forms a quantum well and within this structure high mobility electrons are generated in the thin layer of AlGaN and fall completely into the GaN layer. The electrons can move rapidly in the GaN-side conduction band without colliding with impurities because of the undoped the GaN layer and form what is called a two-dimensional electron gas (2DEG),. The effect of this is to create a very thin layer of highly mobile conductive electrons at very high concentration, giving the channel a very high electron mobility. As with all other types of FETs, a voltage applied to the gate changes the conductivity of this layer. Thus the supplier to conduction in a HEMT is the 2DEG which itself comes from the sum of spontaneous polarization of the polar material and a piezoelectric polarization due to the deformation induced by the mismatch between the two layers (AlGaN and GaN).

However, after years of development there are some drawback on the traditional AlGaN/GaN HEMTs. Indeed, there is increasing indication, that total stress limits the reliability of AlGaN / GaN conventional HEMTs (Park et al [106], Chini et al. [107]). In addition, the need to extend GaN HEMTs to millimeter-scale applications imposes thinner upper barriers to minimize the effects of short channels and to allow higher cutoff frequencies, while 2-DEG AlGaN/GaN electron gases are subject to surface depletion effects when the thickness of the upper barrier is thinned below 15 nm.

Following the idea of Kuzmik [3], AlInN/GaN HEMTs were proposed as an alternative to GaN-based HEMTs, offering a solution to the strain-related device reliability . In addition, surface depletion effects should be far weaker for the AlInN/GaN system

(Kuzmik) **[3]**, enabling, in principle, thin-barrier GaN HEMTs that should maintain excellent channel aspect ratios down to very short gate lengths. Ultrathin-barrier of AlInN/GaN HEMTs was verified down to 3-nm and high temperature stability (as high as 1000 C) have also been reported (Medjdoub et al **[108]).**

AlInN/GaN HEMTs have two main advantages over AlGaN/GaN HEMTs: (i) the charge induced by the spontaneous polarization is almost three times higher, allowing higher current densities. Electron densities as high as 2.73×10^{13} can be reached in lattice matched AlInN/GaN devices.(ii) $Al_{0.83}In_{0.17}N$ and GaN are lattice matched removing strains in the heterostructures . These mechanical constraints are harmful to the reliability of the devices and are also supposed to be at the origin of trapping centers in transistors **[109,110,111].**

4.7.2 HEMT Physical processes and derived equations:

A basic configuration AlInN/GaN HEMT is shown in **Figure 4.11**
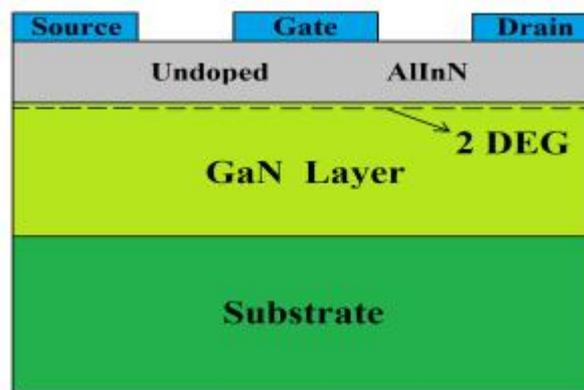
Figure 4.11 Basic AlInN/GaN HEMT

Its corresponding band diagram is sketched in **Figure 4.12.**
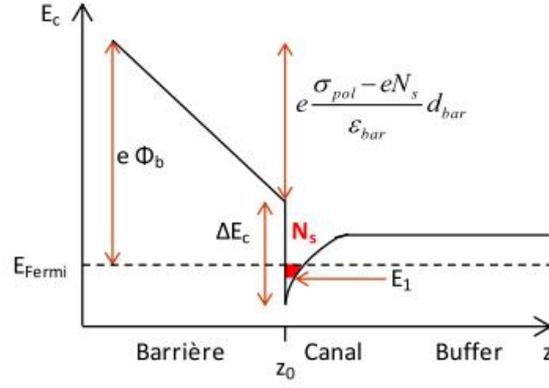
Figure 4.12 Band diagram for the balance equation model of an AlInN/GaN structure

For most of cases only quantum well ground state energy E_1 is occupied then the balance equation can then be written as:

$$e\Phi_b(x) - \frac{ed_{AlInN}}{v_0 v_{AlInN}(x)}(\dagger_{AlInN/GaN}(x) - en_{2d}) - \Delta E_{c,AlInN/GaN} + E_1 + (E_F - E_1) = 0 \qquad (4.17)$$

Triangular quantum well discrete energy levels are well known with the ground state E_1 is:

$$E_1 = \chi\, n_s^{2/3}$$

with $\qquad \chi = \left(\dfrac{9f\,\hbar e^2}{8\sqrt{8m^*}\, v^{AlInN}}\right)^{2/3}$

and the energy difference $E_F - E_1$:

$$E_F - E_1 = \frac{f\,\hbar^2}{m^*} n_s \qquad (4.18)$$

where $\dfrac{f\,\hbar^2}{m^*}$ is the quantum well density of states.

The 2D electron gas density is then:

$$n_s = \left(\frac{f\,\hbar^2}{e^2 m^*}\frac{v_0 v_r^{Al_{1-x}In_xN}}{d^{AlInN}} + 1\right)^{-1}\left(\frac{\dagger^{Al_{1-x}In_xN}}{e} - \frac{v_0 v_r^{Al_{1-x}In_xN}}{e^2 d^{AlInN}}(e\Phi_b(x) - \Delta E_c^{AlInN/GaN}(x) + \chi\, n_s^{2/3})\right) \qquad (4.19)$$

the previous equation is simplified if we consider that in reality the ground state energy E_1 nearly coincides with the bottom of channel conduction band i.e. neglecting the term $\chi\, n_s^{2/3}$

and then neglecting further $\dfrac{f\,\hbar^2}{e^2 m^*}\dfrac{v_0 v_r^{Al_{1-x}In_xN}}{d^{AlInN}}$ we get the standard expression for the density of

the 2DEG:

$$n_s = \frac{\dagger^{Al_{1-x}In_xN}}{e} - \frac{v_0 v_r^{Al_{1-x}In_xN}}{e^2 d^{AlInN}}\left(e\Phi_b(x) - \Delta E_c^{AlInN/GaN}(x)\right) \tag{4.20}$$

e is the electron charge, d^{AlInN} barrier layer thickness and $v_r^{Al_{1-x}In_xN}$ the alloy permittivity given by:

$$v_r^{Al_{1-x}In_xN}(x) = (1-x)v_r^{AlN} + xv_r^{InN} \tag{4.21}$$

$\dagger^{AlInN}$ the polarization-induced charge

$$\dagger^{Al_{1-x}In_xN} = -P_{sp}^{Al_{1-x}In_xN} - P_{piezo}^{Al_{1-x}In_xN} \tag{4.22}$$

$_b$ is the Schottky contact barrier height., E_F is Fermi energy level.

$\Delta E_c^{AlInN/GaN}(x)$ the conduction band discontinuity between barrier and buffer takes the following value [112]:

$$\Delta E_c^{AlInN/GaN}(x) = 0.63(E_g^{Al_{1-x}In_xN}(x) - E_g^{GaN}) \tag{4.23}$$

In a real device one usually introduce a thin AlN layer, to get an heterostructure with AlInN for the barrier, AlN for the interlayer, and GaN for the bulk (**Figure 4.11**). The introduction of an AlN spacer layer at the AlInN/GaN interface increases the carrier density and effectively reduces the alloy scattering of 2DEG as well as provides better carrier confinement **[114,115]**.
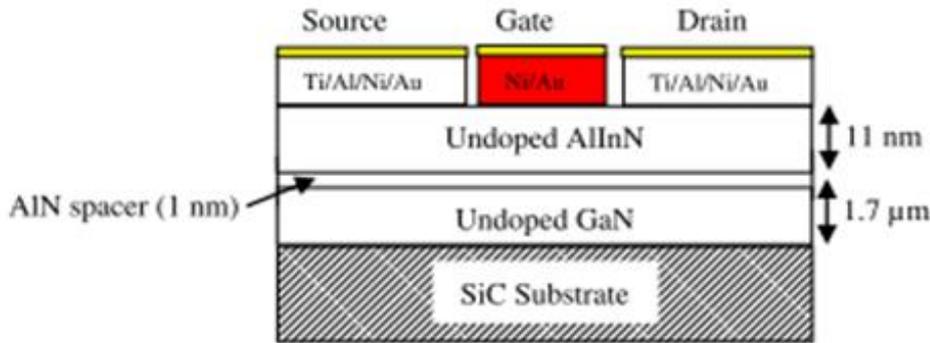
Figure 4.13 Structure of an AlInN HEMT transistor

The corresponding energy band diagram is sketched in **figure 4.14.**
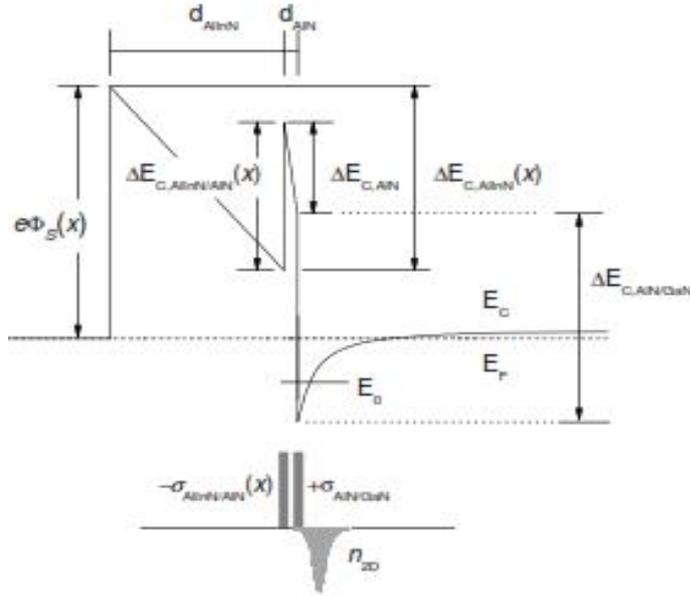
Figure 4.14 Band diagram for the balance equation model of an AlInN/AlN/GaN

The balance equation for a configuration with the AlN spacer is:

$$e\Phi_b(x) - E_{c,AlInN/AlN}d_{AlInN} + \Delta E_{c,AlInN/AlN} - E_{c,AlN}d_{AlN} - \Delta E_{c,AlN/GaN} + E_0 + (E_F - E_0) = 0 \quad (4.24)$$

Note that in this case

$$E_{c,AlN} = e(\dagger_{AlN/GaN} - en_{2d})/\vee_0\vee_{AlN}$$

is the field across the AlN and

$$E_{c,AlInN} = e(\dagger_{AlInN/AlN}(x) + \dagger_{AlN/GaN} - en_{2d})/\vee_0\vee_{AlInN}(x)$$

is the field across the AlInN barrier. The latter is thus determined by the total polarization charge across the AlN interlayer.

We get the expression of n_s:

$$n_s = \frac{1}{e}\left(\frac{d^{AlInN}}{\vee^{AlInN}} + \frac{d^{AlN}}{\vee^{AlN}}\right)^{-1}\left[\frac{d^{AlInN}\dagger^{AlInN}}{\vee^{AlInN}} + \frac{d^{AlN}\dagger^{AlN}}{\vee^{AlN}} - \frac{\vee_0}{e}(e\Phi_b(x) - \Delta E_c^{AlN/GaN} + \Delta E_c^{AlInN/AlN}(x) + E_F)\right]$$

$$(4.25)$$

If we assume that ₆ for III-nitrides is given by the difference between the metal work function ₘ and the semiconductor electron affinity **[113],** and taking the following values

of electron affinities **[114]**:   (InN) = 5.75 eV,   (AlN)= 2.05 eV,   (GaN) = 4.16 eV, $_m$ (Ni) = 5.1 eV by applying Vegard's law we get:

$$\Phi_b(Ni / Al_{1-x}In_xN) = 3.05 - 3.7x \tag{4.22}$$

If we further take a buffer (AlInN) thickness of 11nm and a spacer thickness of 1nm, equations 4.21 and 4.25 representing the variation of the two-dimensional gas density with In concentration for a basic (red) and with a spacer (blue) configurations are illustrated in Figure 4.15.
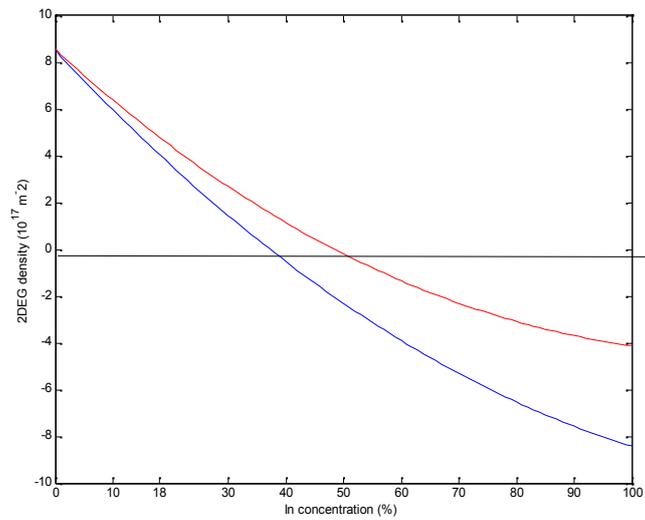
Figure 4.15 2DEG density vs In concentration for AlInN/GaN (blue) and AlInN/AlN/GaN (red) HEMT configurations.

One is mainly interested in the region around the matching point (MP) x=0.82, at that concentration the electron gas may, theoretically, reach a density of 4.70 10^{17} m^{-2} for a AlInN/AlN/GaN configuration. In the case of a basic configuration calculation yields a density of 4 10^{17} m^{-2} in agreement with other works [3]. Now, if we compare the two curves we clearly observe the impact of the thin layer of AlN by the increase the gas density estimated at approximately 18% at the MP. Another noticeable fact is the negative values obtained for the gas density at above approximately 50% of In content. That corresponds to obtaining a gas of holes as carriers (2DHG).

Since the stress is composition dependent, to provide estimation of a gauge factor, the factors influencing the change in channel resistance with concentration are investigated. The channel resistance is inversely related to the 2DEG sheet carrier density and electron mobility

$$R_{ch} = \frac{A}{q n_s \tilde{}_e} \tag{4.26}$$

where the A is cross sectional area of the 2DEG. In the presence of stress, the normalized change in channel resistance can be written as:

$$\frac{\Delta R_{ch}}{R_{ch}} = \frac{\Delta n_s}{n_s} + \frac{\Delta \tilde{}_e}{\tilde{}_e} \tag{4.27}$$

To evaluate the effect of stress on the channel resistance, both the effect of stress on the 2DEG sheet carrier density and mobility needs to be considered. Strain-enhanced mobility can result from reduced average conductivity effective mass from carrier repopulation and band warping, suppression of intervalley scattering from subband splitting, and change in density of states with stress. Unlike Si, GaN is a direct semiconductor with a non-degenerate conduction band minimum at the -point. Therefore, stress-induced change of the average effective mass due to electron repopulation and scattering can be neglected. Thus, the mobility change is dominated by a change in the effective mass through band warping.

$$\frac{\Delta R_{ch}}{R_{ch}} = \frac{\Delta n_s}{n_s} + \frac{\Delta m_e}{m_e} \tag{4.28}$$

If we take the zero stress concentration x=0.82 as the reference point, we will get the fluctuation of the 2DEG density and the electron effective mass around the matching point as respectively:

$n_s=n_s(x) - n_s(0.82), \quad m_e=m_e(x) - m_e(0.82).$

where $m_e(x)$ is the electron effective mass of the strained structure.

The relative variation due to the indium concentration fluctuation around the matching (x=0.82) of the channel resistance along with the 2DEG and the electron effective mass is plotted in **Figure 4.16.** For In variation less than ±8% the plot is linear with the variation of the electron gas density having the main contribution, and to get a practical evaluation a 2% variation of the In results approximately in a variation of 10% of the channel resistance.
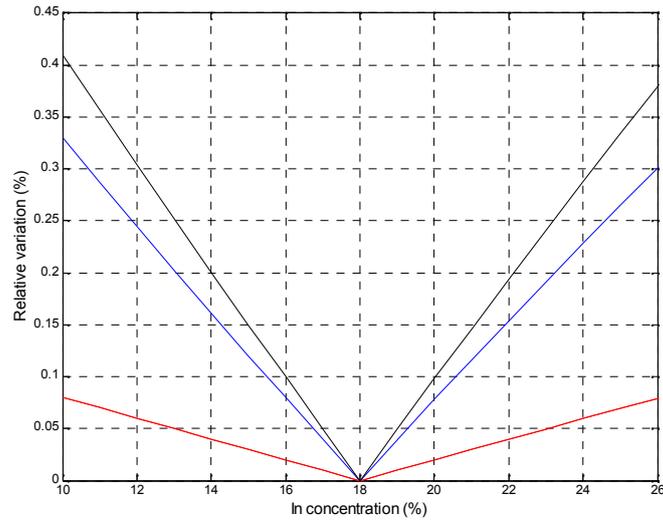
Figure 4.16 Channel resistance variation ΔR/R (black), 2DEG relative variation Δn$_s$/n$_s$ (blue)

electron effective mass variation (red)

CONCLUSION

This work was dealing with a nitride compound AlInN which is a relatively new comer with respect to the other well studied alloys such as AlGaN or InGan. Thanks to new methods of growing this ternary has found new multiple use in electronic and optical devices such as, to name a few, high power transistors or distributed Bragg reflector.

Our contribution was through a comparative study of all possible phases of this compound. This comparative study was conducted by means of two methods : the first one the tight binding method is semi-empirical, the second the density functional theory is an ab-initio method. The aim of this work is first to study, for a given phase, the variation of a physical property with the indium composition, then to set an inter phase comparison. In the following we summarize our main results:

First of all the obtained data for $Al_x In_{1-x}N$ were checked with the binaries that is for x=0 and x=1 for which experimental results were available and the results were pretty good in agreement with experimental works.

As far as the structural properties are concerned we observe : A linear increase of the lattice parameter and so a decrease of the bulk modulus. The denser packing rocksalt phase taking the highest BM value while wurtzite and zincblende phases have close values

In the chapter of electronic properties DFT calculation with the modified Becke and Jonson potential allowed decent band gap values compared experimental data . The first comment confirmed literature results that AlN in its zincblende phase is an indirect semi conductor, and since InN is a direct one (for all structures) the AlInN alloy presented mixed properties from direct to indirect depending on the In proportion.

 On the other side, wurtzite structure- showed a direct band gap variation for the whole In range and the largest gap spectrum (from AlN to InN) belongs to the rocksalt phase with an extent of.4.94 eV. The gap of all phases decreased with In, however with a composition dependent bowing factor confirming the general trend in nitride alloys (InGaN and AlGaN). Without being conclusive, our result and the absence of this tendency in the zinc blende phase may suggest a charge transfer cause for this dependency .

The effective mass presented a decreasing value with In composition favoring the mobility at rich In concentrations and the lighter mass for the wurtzite structure. The density of states diagrams show a higher density in the wurtzite structure and the predominance of p states.

High pressure study showed the following points:

- confirmed the wurtzite as the most stable, independently of In proportion, and that the wurtzite and zincblende presented rather close values of ground state energies.
- the Wz-Rs and Zb-Rs occurred for all In concentrations and that the phase transition pressures were relatively low (less than 20 GPa).
- slow increase of band gap with pressure.
- If we consider the ternaries as $In_xAl_{1-x}N$ or $Al_xIn_{1-x}N$, the effect of augmenting x results in an increase of the phase transition pressure.

Heterostructure in which a film of AlInN is deposited on a bulk GaN induces a biaxial strain resulting in a tetragonal symmetry in which the basal parameter may be compressed or extended depending on the In content, and the perpendicular parameter c taking the other way round. The first main result that the cubic binaries do not show any kind of spontaneous polarization nor do they present any piezoelectric one under a biaxial strain, so the rest of the study was carried out for the wurtzite structure.

The strain effect on the electronic structure resulted in a lower band gap and a lower electron effective mass for In concentration less than 25%. The piezoelectric and spontaneous polarizations has been recalculated according to the new structure and the main contribution has been found to proceed from the latter one.

Finally the outcome of the strain study was applied to a HEMT transistor and results showed that the sheet of induced electron gas has a high density of about $4.7 \ 10^{17} \ m^{-2}$ and that the channel resistance variation was mainly caused by the 2DEG fluctuation.

Outlook

Several extensions can be added to the current study of which the:

- High temperature effects

- Optical properties with application to an optical device

- Effects of defects on physical properties

- calculation of the spontaneous and piezoelectric polarization of AlInN cubic phase.

APPENDIX A

TIGHT BINDING HAMILTONIAN AND PARAMETERS OF A ZINCBLENDE STRUCTURE

The TB sps[*] Hamiltonian matrix of a zincblende structure without spin-orbit interaction is given by the following matrix [116]:

$$
H = \begin{bmatrix}
E_{sa} & V_{ss}g_1 & 0 & 0 & 0 & V_{sapc}g_2 & V_{sapc}g_3 & V_{sapc}g_4 & 0 & 0 \\
V_{ss}g_1' & E_{sc} & -V_{pasc}g_2' & -V_{pasc}g_3' & -V_{pasc}g_4' & 0 & 0 & 0 & 0 & 0 \\
0 & -V_{pasc}g_2 & E_{pa} & 0 & 0 & V_{xx}g_1 & V_{xy}g_4 & V_{xy}g_3 & 0 & -V_{pasc*}g_2 \\
0 & -V_{pasc}g_3 & 0 & E_{pa} & 0 & V_{xy}g_4 & V_{xx}g_1 & V_{xy}g_2 & 0 & -V_{pasc*}g_3 \\
0 & V_{pasc}g_4 & 0 & 0 & E_{pa} & V_{xy}g_3 & V_{xy}g_2 & V_{xx}g_1 & 0 & -V_{pasc*}g_4 \\
V_{sapc}g_2' & 0 & V_{xx}g_1' & V_{xy}g_4' & V_{xy}g_3' & E_{pc} & 0 & 0 & V_{s*apc}g_2 & 0 \\
V_{sapc}g_3' & 0 & V_{xy}g_4' & V_{xx}g_1' & V_{xy}g_2' & 0 & E_{pc} & 0 & V_{s*apc}g_3 & 0 \\
V_{sapc}g_4' & 0 & V_{xy}g_3' & V_{xy}g_2' & V_{xx}g_1' & 0 & 0 & E_{pc} & V_{s*apc}g_4 & 0 \\
0 & 0 & 0 & 0 & 0 & V_{s*apc}g_2' & V_{s*apc}g_3' & V_{s*apc}g_4' & E_{s*a} & 0 \\
0 & 0 & -V_{pasc*}g_2' & -V_{pasc*}g_3' & -V_{pasc*}g_4' & 0 & 0 & 0 & 0 & E_{s*c}
\end{bmatrix}
$$

The four parameters g_1 to g_4 arise from summing over the factors $\exp(i.d_1.k_0)$. They are defined by:

$$g_1 = \frac{1}{4}\left(\exp(id_1k_0) + \exp(id_2k_0) + \exp(id_3k_0) + \exp(id_4k_0)\right)$$

$$g_2 = \frac{1}{4}\left(\exp(id_1k_0) + \exp(id_2k_0) - \exp(id_3k_0) - \exp(id_4k_0)\right)$$

$$g_3 = \frac{1}{4}\left(\exp(id_1k_0) - \exp(id_2k_0) + \exp(id_3k_0) - \exp(id_4k_0)\right)$$

$$g_3 = \frac{1}{4}\left(\exp(id_1k_0) - \exp(id_2k_0) - \exp(id_3k_0) + \exp(id_4k_0)\right)$$

where we have assumed that atom 1 is located at the origin and d_i (i=1,4) are the positions of its four nearest neighbors and a is the lattice parameter.

$$d_1 = \frac{1}{4}(1,1,1); \ d_2 = \frac{a}{4}(1,-1,-1); \ d_3 = \frac{a}{4}(-1,1,-1); \ d_4 = \frac{a}{4}(-1,-1,1).$$

Some of the onsite and hopping parameters AlN InN and GaN parameters listed below have been extracted from Ref. **[117]** and modified so as to fit with high symmetry points.

AlN:

E_{sa}=-11.5047; E_{pa}=4.3815; E_{sc}=0.5047; E_{pc}=10.2184; E_{s*a}=12.04;E_{s*c}=13.74;V_{ss}=-9.8077;V_{xx}=6.031; V_{xy}=8.6191; V_{sapc}= 9.4; V_{pasc}=8.5; V_{s*apc}=8.03; V_{pas*c}=2.47;

InN:

E_{sa}=-12.8605; E_{pa}=1.98; E_{sc}=-0.3994; E_{pc}=8.02; E_{s*a}=10.63; E_{s*c}=13.00; V_{ss}=4.2285;V_{xx}=3.65; V_{xy}=6.405; V_{sapc}= 3.81; V_{pasc}=5.75; V_{s*apc}=6.88; V_{pas*c}=3.36;

All elements are given in eV.

APPENDIX B

TIGHT BINDING HAMILTONIAN AND PARAMETERS OF A WURTZITE STRUCTURE

The TB sps Hamiltonian matrix for a wurtzite structure without spin-orbit interaction, can be expressed in block from as below with the notation following the Ref. **[118,119].**

$$H = \begin{bmatrix} E_a & H_0 & H_{13} & H_{14} \\ H_0 & E_a & H_{14} & H_{24} \\ H'_{13} & H'_{14} & E_c & H_0 \\ H'_{14} & H'_{24} & H_0 & E_c \end{bmatrix}$$

where the different matrix elements are 4×4 matrix blocks. The diagonal matrices E_a and E_c contain the orbital energies. The matrices H_{ij} represent the interaction up to nearest neighbors.

$H_{13} = g_1 * M_{13}$

$H_{14} = g_3 * M_{14}$

$H_{24} = g_2 * M_{24}$

$$E_a = \begin{bmatrix} E_{sa} & 0 & 0 & 0 \\ 0 & E_{pza} & 0 & 0 \\ 0 & 0 & E_{pxa} & 0 \\ 0 & 0 & 0 & E_{pxa} \end{bmatrix}$$

$$E_c = \begin{bmatrix} E_{sc} & 0 & 0 & 0 \\ 0 & E_{pc} & 0 & 0 \\ 0 & 0 & E_{pc} & 0 \\ 0 & 0 & 0 & E_{pc} \end{bmatrix}$$

$$M_{13} = \begin{bmatrix} f_0 U_{1ss} & f_0 U_{1sz} & f_1 U_{1sx} & \dfrac{\sqrt{3}}{2} f_3 U_{1sx} \\[2ex] f_0 U_{1zs} & f_0 U_{1zz} & f_1 U_{1zx} & \dfrac{\sqrt{3}}{2} f_3 U_{1zx} \\[2ex] f_1 U_{1xs} & f_1 U_{1xz} & f_1 U_{1xx} + \dfrac{3}{4} f_2 \left(U_{1xx} + U_{1yy} \right) & \dfrac{\sqrt{3}}{4} f_3 \left(U_{1xx} - U_{1yy} \right) \\[2ex] \dfrac{\sqrt{3}}{2} f_3 U_{1xs} & \dfrac{\sqrt{3}}{2} f_3 U_{1xz} & -\dfrac{\sqrt{3}}{4} f_3 \left(U_{1xx} - U_{1yy} \right) & f_1 U_{1yy} + \dfrac{3}{4} f_2 \left(U_{1xx} + U_{1yy} \right) \end{bmatrix}$$

$$M_{14} = \begin{bmatrix} U_{ss} & U_{sz} & 0 & 0 \\ U_{zs} & U_{zz} & 0 & 0 \\ 0 & 0 & U_{xx} & 0 \\ 0 & 0 & 0 & U_{xx} \end{bmatrix}$$

$$M_{24} = \begin{bmatrix} f_0' U_{1ss} & f_0' U_{1sz} & -f_1 U_{1sx} & -\dfrac{\sqrt{3}}{2} f_3' U_{1sx} \\[2ex] f_0' U_{1zs} & f_0' U_{1zz} & -f_1 U_{1zx} & -\dfrac{\sqrt{3}}{2} f_3' U_{1zx} \\[2ex] -f_1 U_{1xs} & -f_1 U_{1xz} & f_1 U_{1xx} + \dfrac{3}{4} f_2' \left(U_{1xx} + U_{1yy} \right) & -\dfrac{\sqrt{3}}{4} f_3' \left(U_{1xx} - U_{1yy} \right) \\[2ex] -\dfrac{\sqrt{3}}{2} f_3' U_{1xs} & -\dfrac{\sqrt{3}}{2} f_3' U_{1xz} & -\dfrac{\sqrt{3}}{4} f_3' \left(U_{1xx} - U_{1yy} \right) & f_1 U_{1yy} + \dfrac{3}{4} f_2' \left(U_{1xx} + U_{1yy} \right) \end{bmatrix}$$

$U_{ss} = V_{ss}/4$; $U_{sz} = -(\mathrm{sqrt}(3)/4) * V_{sapc}$; $U_{zs} = -U_{sz}$;

$U_{zz} = ((V_{xx}/4) + (V_{xy}/2))$; $U_{xx} = ((V_{xx}/4) - (V_{xy}/4))$;

$U_{1ss} = U_{ss}$; $U1_{sz} = -U_{sz}/3$; $U_{1zs} = -U_{zs}/3$; $U_{1sx} = V_{sapc}/\mathrm{sqrt}(6)$;

$U_{1xs} = -V_{scpa}/\mathrm{sqrt}(6)$; $U_{1xz} = V_{xy}/(3*\mathrm{sqrt}(2))$; $U_{1zx} = U_{1xz}$;

$U_{1xx} = ((8*U_{zz}/9) + (U_{xx}/9))$; $U_{1zz} = ((U_{zz}/9) + (8*U_{xx}/9))$; $U_{1yy} = U_{xx}$;

The tight binding (self Energies In, Al (cation) and N (anion)), AlN, InN and GaN parameters have been extracted from Ref. **[91]** and modified so as to fit with high symmetry points.

On-site elements:

$E_{sa}(AlN)=-12.104$

$E_{pxa}(AlN)= 3.581; E_{pza}(AlN)= 3.725; E_{sc}(AlN)=-0.096; E_{pc}(AlN)=8.95$

$E_{sa}(InN)=-6.791; E_{pxa}(InN)= 0.000; E_{pza}(InN)= 0.000; E_{sc}(InN)=-3.015; E_{pc}(InN)=8.822;$

off site elements:

$V_{ss}(AlN)= -10.735; V_{xx}(AlN)= 5.808; V_{xy}(AlN)= 7.486;$

$V_{scpa}(AlN)= 9.755; V_{sapc}(AlN)=10.092;$

$V_{ss}(InN)= -5.371; V_{xx}(InN)= 0.022;$

$V_{xy}(InN)=6.373; V_{scpa}(InN)= 0.370; V_{sapc}(InN)=18.0$

All elements are given in eV.

APPENDIX C

ELASTIC THEORY

1) Strain tensor

For a detailed analysis refer to the classical book of Nye [120].

Two close points A and B of a solid ($\overrightarrow{AB} = \overrightarrow{dr}$) under stress shift to a position $\overrightarrow{A'B'} = \overrightarrow{dr'}$ so that $\overrightarrow{dr'} = \overrightarrow{dr} + \overrightarrow{du}$ where

$$\overrightarrow{du} = \frac{\partial u_i}{\partial x_1} dx_1 + \frac{\partial u_i}{\partial x_2} dx_2 + \frac{\partial u_i}{\partial x_3} dx_3$$

is the displacement vector.

the relation between du and dx may be written in a matrix form

$[du] = [s][dx]$ with $[s]$ the matrix representation of the strain tensor.

The symmetric part of the strain tensor which correspond to the length variations (not the rotation of the body) is:

$$\overset{=}{v} = \begin{bmatrix} v_{11} & v_{12} & v_{13} \\ v_{12} & v_{22} & v_{23} \\ v_{13} & v_{23} & v_{33} \end{bmatrix} \tag{C1}$$

where

$$v_{ij} = \frac{1}{2}\left(\frac{\partial u_i}{\partial x_j} - \frac{\partial u_j}{\partial x_i} \right)$$

The diagonal terms of the tensor represent the stretching components of the strain whereas the off diagonal are the shear components.

2) Stress tensor

If a stress is applied to a solid along its facets experiences forces dF$_i$

$$d\overrightarrow{F_i} = \overline{\overline{\dagger}} ds_i = \overline{\overline{\dagger}} dx_j dx_k \tag{C2}$$
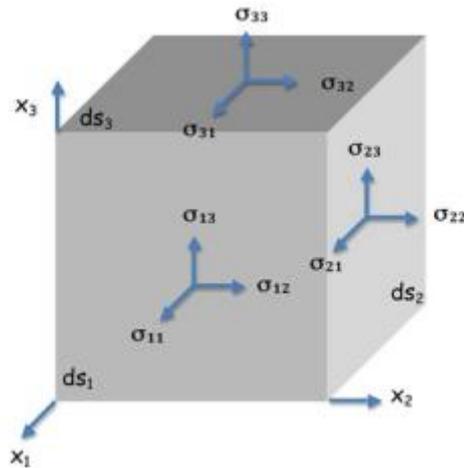
the overall effect can be described by a symmetric tensor called the stress tensor $\overline{\overline{\mathsf{T}}}$ of the form:

$$\overline{\overline{\mathsf{T}}} = \begin{bmatrix} \mathsf{T}_{11} & \mathsf{T}_{12} & \mathsf{T}_{13} \\ \mathsf{T}_{12} & \mathsf{T}_{22} & \mathsf{T}_{23} \\ \mathsf{T}_{13} & \mathsf{T}_{23} & \mathsf{T}_{33} \end{bmatrix} \tag{C3}$$

$$\overline{\overline{\mathsf{T}}} = \overline{\overline{C}}\overline{\overline{v}} \tag{C4}$$

where T_{ij} are the components of stress tensor. The first subscript refers to the normal of the

face on which the fore acts the second to the direction of the force.

$_{ii}$ are components of a tensile stress (force is normal to the applied face).

$_{ij}$ (i j) are components of a shear stress (force is along to the applied face).

3) Stiffness tensor

The relation between the strain and stress is governed by the well known Hooke's law through

the relation

$$\overline{\overline{\mathsf{T}}} = \overline{\overline{C}}\overline{\overline{v}}$$

where $\overline{\overline{C}}$ the stiffness tensor is a symmetric tensor of the form

$$C_{ij} = \begin{pmatrix} C_{11} & C_{12} & C_{13} & C_{14} & C_{15} & C_{16} \\ C_{21} & C_{22} & C_{23} & C_{24} & C_{25} & C_{26} \\ C_{31} & C_{32} & C_{33} & C_{34} & C_{35} & C_{36} \\ C_{41} & C_{41} & C_{43} & C_{44} & C_{45} & C_{46} \\ C_{51} & C_{51} & C_{53} & C_{54} & C_{55} & C_{56} \\ C_{61} & C_{61} & C_{63} & C_{64} & C_{56} & C_{66} \end{pmatrix}$$

(C5)

For a cubic symmetry as in the zincblende structure the number of C_{ij} reduces to four independent components C_{11}, C_{12}, C_{44} and the matrix is in the form

$$C_{ij} = \begin{pmatrix} C_{11} & C_{12} & C_{12} & 0 & 0 & 0 \\ C_{12} & C_{11} & C_{12} & 0 & 0 & 0 \\ C_{12} & C_{12} & C_{11} & 0 & 0 & 0 \\ 0 & 0 & 0 & C_{44} & 0 & 0 \\ 0 & 0 & 0 & 0 & C_{44} & 0 \\ 0 & 0 & 0 & 0 & 0 & C_{44} \end{pmatrix}$$

(C6)

For a hexagonal symmetry as in the wurtzite structure the number of C_{ij} reduces to four independent components C_{11}, C_{12}, C_{13}, $C_{33,}$ C_{44} and the matrix will take the form

$$C_{ij} = \begin{pmatrix} C_{11} & C_{12} & C_{13} & 0 & 0 & 0 \\ C_{12} & C_{11} & C_{13} & 0 & 0 & 0 \\ C_{13} & C_{13} & C_{33} & 0 & 0 & 0 \\ 0 & 0 & 0 & C_{44} & 0 & 0 \\ 0 & 0 & 0 & 0 & C_{44} & 0 \\ 0 & 0 & 0 & 0 & 0 & \dfrac{C_{11} - C_{12}}{2} \end{pmatrix}$$

(C7)

The values of the elastic constant are all taken from Reference **[104]**

Table C1 Nitrides elastic constants.

Zincblende	AlN	GaN	In
C_{11}	315	291	190
C_{12}	150	148	104
C_{14}	185	158	99
Wurtzite	AlN	GaN	In
C_{11}	410	373	190
C_{12}	140	141	104
C_{13}	100	80	121
C_{33}	390	387	182
C_{44}	120	94	99

BIBLIOGRAPHY

[1] S.Nakamura, M.Senoh, T. Muka, "p-GaN/n-InGaN/n-GaN double heterostructure blue-light-emitting diodes" Jpn. J. Appl. Phys., Part 2, 32 L8 -L11 (1993).

[2] J. Wu, "When group-III nitrides go infrared: New properties and perspectives" J. Appl. Phys. vol. 106 N°1, 011101 (2009).

[3] J. Kuzmik. "Power electronics on InAlN/(In)GaN: Prospect for a record performance" IEEE Electron Device Lett., 22:510,(2001).

[4] R Butté, J. F. Carlin, E. Feltin, M. Gonschorek, S. Nicolay, G. Christmann, D. Simeonov, A. Castiglia, G. Dorsaz and H. J. Buehlmann, "Current status of AlInN layers lattice-matched to GaN for photonics and electronics", J. Phys. D: Appl. Phys. Vol.40, 6328–6344, (2007).

[5] C. J. Humphreys, "Solid State Lighting", MRS Bulletin 33 459 470 (2008)

[6]D. J. As, D. Schikora, and K. Lischka, "Molecular beam epitaxy of cubic III-nitrides on GaAs substrates", Phys. stat. sol. (c), vol. 0, No. 6, pp. 1607–1626, (2003)

[7] N. Li, S. K. Yadav, J. Wang, X. Liu, A. Misra, "Growth and stress-induced transformation of zinc blende AlN layers in Al-AlN-TiN multilayers" Sc. Rep. 5, 18554 (2015).

[8] H. Xia, Q. Xia and A. L. Ruoff, "High-pressure structure of gallium nitride: Wurtzite-to-rocksalt phase transition" Phys. Rev. B 47, 12925 (1993).

[9] C. Pinquier, F. Demangeot, J. Frandon, J. C. Chervin, A. Polian, B. Couzinet, P. Munsch, O. Briot, S. Ruffenach, B. Gil and B. Maleyre, "Raman scattering study of wurtzite and rocksalt InN under high pressure" Phys. Rev. B73, 115211 (2006).

[10] F. Tran, P. Blaha, "Accurate band gaps of semiconductors and insulators with a semilocal exchange-correlation potential", Physical Review Letters 102 226401, (2009).

[11] P. Blaha, K. Schwarz, G.H. Madsen, D. Kvasnicka, J. Luitz, FP-L/APW +lo Program for Calculating Crystal Properties, Vienna University of Technology, Vienna, (2001).

[12]P. O. Löwdin, "On the non-orthogonality problem connected with the use of atomic wave functions in the theory of molecules and crystals" J. Chem. Phys. 18, 365 (1950).

[13] J. C. Slater and G. F. Koster, Phys. Rev. 94, 1498 (1954).

[14] Behnaz G., Khorasani S., " An overview of tight binding method for two dimensional carbon structures, Graphene: Properties, synthesis and application , pp 1-37, (2011).

[15] P. Vogl, H. P. Hjalmarson, and J. D. Dow." A Semi-empirical tight-binding theory of the electronic structure of semiconductors" Journal of Physics and Chemistry of Solids 44, 365 (1983).

[16] David Sholl, Janice A Steckel-"Density functional theory a practical introduction"- Wiley-Interscience (2009).

[17] P. Hohenberg and W. Kohn. "Inhomogeneous electron gas" Phys. Rev. 136, B864 (1964).

[18] W. Kohn and L. J. Sham. "Self-consistent equations including exchange and correlation " . Phys. Rev. 140, A1133 (1965).

[19] J. Perdew, K. Burke, M. Ernzerhof, "Generalized Gradient Approximation Made Simple", Phys. Rev. Lett. 77 3865 (1996).

 [20] J. Heyd, J.E. Peralta, G. E. Scuseria and R. L. Martin, "Energy band gaps and lattice parameters evaluated with the Heyd-Scuseria-Ernzerhof screened hybrid functional" J. Chem. Phys. 123, 174101 (2006).

[21] J. Tao, J. P. Perdew, V. N. Staroverov, G. E. Scuseria, "Climbing the density functional ladder: Nonempirical meta–generalized gradient approximation designed for molecules and solids" Phys. Rev. Lett. 91, 146401 (2003))

[22] L. J. Sham and M. Schluter, "Density-functional theory of the band gap" Phys. Rev. B 32, 3883 (1985).

[23] W. Kohn, "Discontinuity of the exchange-correlation potential from a density-functional viewpoint" Phys. Rev. B 33, 4331 (1986).

[24] John P. Perdew and Mel Levy "Physical Content of the Exact Kohn-Sham Orbital Energies: Band Gaps and Derivative Discontinuities" Phys. Rev. Lett.51, 1884 (1983).

[25] E. Engel, R. M. Dreizler: "Density Functional Theory - An Advanced Course", Springer (2011).

[26] Axel D. Becke and Erin R. Johnson "A simple effective potential for exchange" The Journal of Chemical Physics **124**, 221101 (2006).

[27] G. Kresse and J. Furthmuller," Efficient iterative schemes for ab initio total-energy calculations using a plane-wave basis set", Comput. Mater. Sci. 6, 15 (1996).

[28] J. M. Soler, E. Artacho,J. D. Gale, A. García, J. Junquera, P. Ordejón, and D. Sánchez-Portal "The SIESTA method for ab-initio order-N materials simulation", J. Phys.: Condens. Matt. 14, 2745-2779 (2002).

[29] P. Blaha, K. Schwarz, G. K. H. Madsen, D. Kvasnicka, J. Luitz, "WIEN2k, An Augmented Plane Wave + Local Orbital Program for Calculating Crystal Properties", Karlheinz Schwartz, Techn. Universität Wien, Austria (2001).

[30] X. Gonze, J.-M. Beuken, R. Caracas, F. Detraux, M. Fuchs, G.-M. Rignanese, L. Sindic, M. Verstraete, G. Zerah, F. Jollet, M. Torrent, A. Roy, M. Mikami, Ph. Ghosez, J.-Y. Raty, D.C. Allan, "First-principles computation of material properties : the ABINIT software project", Computational Materials Science 25, 478-492 (2002).

[31] X. Gonze, G.-M. Rignanese, M. Verstraete, J.-M. Beuken, Y. Pouillon, R. Caracas, F. Jollet, M. Torrent, G. Zerah, M. Mikami, et al., "A brief introduction to the ABINIT software package" Zeit. Kristallogr. 220, 558 (2005).

[32] P. Giannozzi, S. Baroni, N. Bonini, M. Calandra, R. Car, C. Cavazzoni, D. Ceresoli, G. L. Chiarotti, M. Cococcioni, I. Dabo, A. Dal Corso, S. Fabris, G. Fratesi, et al," QUANTUM ESPRESSO: a modular and open-source software project for quantum simulations of materials", J. Phys.:Condens.Matter 21, 395502 (2009).

[33] "Planewaves, Pseudopotentials and the LAPW Method" D. J. Singh, L. Nordstrom Springer, (2006).

[34] D. R. Hamann, M. Schlüter, and C. Chiang "Norm-Conserving Pseudopotentials" Phys. Rev. Lett. **43**, 1494 (1979).

[35] N. Troullier and José Luís Martins "Efficient pseudopotentials for plane-wave calculations" Phys. Rev. B**43**, 1993 (1991).

[36] David Vanderbilt "Soft self-consistent pseudopotentials in a generalized eigenvalue formalism" Phys. Rev. B **41**, 7892 (1990).

[37] P. E. Blöchl "Projector augmented-wave method" Phys. Rev. B50, 17953 (1994).

[38] G. Kresse and D. Joubert "From ultrasoft pseudopotentials to the projector augmented-wave method" Phys. Rev. B **59**, 1758 (1999).

[39] Wien2K user guide.

[40] A. Zunger, S.-H. Wei, L. G. Ferreira, J. E. Bernard, "Special quasirandom structures" Phys. Rev. Lett 65 354 (1990).

[41] S.-H. Wei, L. G. Ferreira, J. E. Bernard, A. Zunger, "Electronic properties of random alloys: Special quasirandom structures", Phys. Rev. B 42 9622 (1990).

[42] A.van de Walle, "Multicomponent multisublattice alloys, non configurational entropy and other additions to the Alloy Theoretic Automated Toolkit", Calphad 33, 266 (2009).

[43] F. Bernardini, V. Fiorentini, "Nonlinear behavior of spontaneous and piezoelectric polarization in III–V nitride alloys", Phys. Status Solidi A 190, 65-73 (2002).

[44] D. Shin, A.van de Walle, Y. Wang and Z. Liu, "First-principles study of ternary fcc solution phases from special quasirandom structures", Phys Rev. B 76, 144204 (2007).

[45] P. Perdew, A. Ruzsinszky, G. I. Csonka, O. A. Vydrov, G. E. Scuseria, L. A. Constantin, X. Zhou, and K. Burke, "Restoring the density-gradient expansion for exchange in solids and surfaces." Phys. Rev. Lett. 100, 136406 (2008).

[46] F.D. Murnaghan, " The compressibility of media under extreme pressures", Proc. Natl. Acad. Sci. USA 30 244–247 (1944) .

[47] P. Rinke, M. Winkelnkemper, A. Qteish, D. Bimberg, J. Neugebauer and M. Scheffler, "Consistent set of band parameters for the group-III nitrides AlN, GaN and InN", Phys. Rev. B 77, 075202 (2008).

[48] S. Goumri-Said, M. B. Kanoun, A. E. Merad, G. Merad and H. Aourag, " Zinblende AlN and GaN under pressure : structural, electronic, elastic and piezoelectric properties"Chem. Phys. 302, 135 (2004).

[49] I. Vurgaftman and J.R. Meyer, "Band parameters for nitrogen containing semiconductors", J. Appl. Phys. 36, 3675 (2003).

[50] S. Adachi, "Properties of Group-IV, III-V and II-VI Semiconductors", Wiley Series in Materials for Electronic & Optoelectronic Applications (2005).

[51] R. Nunez-Gonzalez, A. Reyes-Serrato,A. Posada-Amarillas and D. H. Galvan, "First-principles calculation of the band gap of $Al_xGa_{1-x}N$ and $In_xGa_{1-x}N$", Revista Mexicana De Fisica S54 (2), pp. 111-118, (2008).

[52] S. Uehara, T. Masamoto, A. Onodera, M. Ueno, O. Shimomura, and K. Takemura, "Equation of state of the rocksalt phase of III–V nitrides to 72 GPa or higher" J. Phys. Chem. Solids 58, 2093 (1997).

[53] Z. Jiao, S. Ma and J. Yang, ,"A comparison of the electronic and optical properties of zinc-blende, rocksalt and wurtzite AlN: A DFT study", Solid State Sci. 13, 331-336 (2011).

[54] M. B. Kanoun, S. Goumri-Said, A. E. Merad, H. Mariette, "Ab initio study of structural parameters and gap bowing in zinc-blende $Al_xGa_{1\ x}N$ and $Al_x In_{1\ x}N$ alloys", J. Appl. Phys. 98, 63710 (2005).

[55] M.Rezek, S. Katircioglu, " A comparative study of the electronic properties of aluminum nitride compounds", Turk. J. Phys. 40, 219-230 (2016).

[56] C. Persson, A. Ferreira da Silva, R. Ahuya, B. Johansson, "Effective electronic masses in wurtzite and zinc-blende GaN and AlN", J. Cryst. Growth 231, 397-406 (2001).

[57] B.-T. Liou and C.-W.Liu, "Electronic and structural properties of zinc blende $Al_xIn_{1-x}N$", Optics Communications 274, pp. 361-365, (2007).

[58] R. Ahmed, S. J. Hashemifar, H. Akbarzadeh, M. Ahmed and F. e-Aleem, "Ab-initio study of structural and electronic properties of III-arsenide binary compounds", Comput. Mater. Sci. 39, 580-586 (2007).

[59] Q. Yan, P. Rinke, M. Schefflerand, C. G. Van de Walle, "Strain effects in group-III nitrides: Deformation potentials for AlN, GaN and InN", Appl. Phys. Lett. 95, 121111 (2009).

[60] S. Saib, N. Bouarissa, "Structural phase transformations of GaN and InN under high pressure", Physica B 387, 377 (2007).

[61] B. UlHaq, R. Ahmed, A. Shaari, F. ElHaj Hassan, M. B. Kanoun and S. Goumri-Said, "Study of wurtzite and zincblende GaN/InN based solar cells alloys: First-principles

investigation within the improved modified Becke-Johnson potential" Sol. Energy 107, 543-552 (2014).

[62] W. Feng, S. Cui, H. Hu, W. Zhao," High-pressure structural and electronic properties of InN", Phys. Status Solidi B 210, 313 (2010).

[63] M. I. Ziane, Z. Bensaad, T. Ouahrani and H. Bennacer, " First principles study of structural, electronic and optical properties of indium gallium nitride arsenide lattice matched to gallium arsenide", Mater. Sci. Semicond. Process. 30, 181-196 (2015).

[64] J. Serrano, A. Rubio, E. Hernandez, A. Munoz, A. Mujica, "Theoretical study of the relative stability of structural phases in group-III nitrides at high pressures", Phys. Rev. B 62, 16612 (2000).

[65] M. Ueno, M. Yoshida, A. Onodera, O. Shimomura and K. Takemura, " Stability of the wurtzite-type structure under high pressure: GaN and InN", Phys. Rev. B 49, 14 (1994).

[66] L.D. Yao, S. D. Luo, X. Shen and S. G.You," Structural stability and Raman scattering of InN nanowires under high pressure", J. Mat. Res. 25, 2330 (2010).

[67] R. Oliva, A. Segura, J. Ibáñez, T. Yamaguchi, Y. Nanishi and L. Artús, " Pressure dependence of the refractive index in wurtzite and rocksalt indium nitride", Appl. Phys. Lett. 105, 232111 (2014).

[68] Fei Wang, S.F. Li, Qiang Sun, Yu Jia, "First-principles study of structural and electronic properties of zincblende $Al_xIn_{1-x}N$",Solid State Sciences 12, pp. 1641-1644, (2010).

[69] S. Berrah, A. Boukortt and H. Abid, "The composition effect on the bowing parameter in the cubic InGaN, AlGaN and AlInN alloys", Semiconductor Physics, Quantum Electronics &Optoelectronics, V. 11, N1, pp. 59-62, (2008).

[70] M. Ferhat, A. Zaoui, M. Certier and B. Khelifa, "Empirical tight-binding band structure of zinc-blende nitrides GaN, AlN and BN", Phys. stat. sol. (b) 195, 415, (1996).

[71] M. Ferhat, F. Bechstedt, "First principles calculations of gap bowing in $In_xGa_{1-x}N$ and $Al_xIn_{1-x}N$ alloys: Relation to structural and thermodynamic properties", Phys. Rev. B65, 075213,(2002).

[72] I. Petrov, K. Mojab, R. C. Powell, J. E. Greene, "Synthesis of metastable epitaxial zincblende structure AlN by solid state reaction", Appl. Phys. Lett. 60, 2491, (1992).

[73] J. Schörmann, D. J. As, K. Lischka, P. Schley, R. Goldhahn, S.F. Li, W. Löffler,. Hetterich and H. Kalt, "Molecular beam epitaxy of phase pure cubic InN", Appl. Phys. Lett. 89,261903 (2006).

[74] Q. Y. Chen, M. Xu, H. P. Zhou, M. Y. Duan, W. J. Zhu and H. L. He, "First-principles calculation of electronic structures and optical properties of wurtzite $In_xGa_{1-x}N$ alloys", Physica B 403, pp. 1666-1672, (2008).

[75] L. Shi, Y. Duan, X. Yang, G. Tang, L. Qin and L. Qiu, "Structural, electronic and elastic properties of wurtzite-structured $Ti_xAl_{1-x}N$ alloys from first principles", Materials Science in Semconductor Processing 15, pp. 499-504, (2012).

[76] E. Lopez-Apreza, J. Arriaga and D. Olguin "Ab initio calculation of structural and electronic properties of $Al_xGa_{1-x}N$ and $In_xGa_{1-x}N$ alloys", Revista Mexicana De Fisica 56 (3), pp. 183-194, (2010).

[77] S. Kumar, S. Pandey, S.K. Gupta, T. K. Maurya, P. Schley, G. Gobsch and R. Goldhahn; "Band structure and optical properties of hexagonal In-rich $In_xAl_{1-x}N$ alloys", J. Phys. Condens. Matter 23, 475801 (10pp) , (2011).

[78]R. R. Pelà, C. Caetano, M. Marques, L. G. Ferreira, J. Furthmüller and L. K. Teles, "Accurate band gaps of AlGaN, InGaN and AlInN alloys calculations based on LDA-1/2 approach", Appl. Phys. Lett., 98, 151907, (2011).

[79]F. Litimein, B. Bouhafs, G. Nouet and P. Ruterana, " Meta-GGA calculation of the electronic structure of group III–V nitrides", Phys. Status Solidi B 243, 1577 (2006).

[80] T. S. Yeh, J. M. Wu, W. H. Lan, " Nanostructured high-entropy alloys with multiple principal elements: novel alloy design concepts and outcomes", J. Cryst. Growth 310, 5308-5311 (2008).

[81] Iliopoulos E, Adikimenakis A, Giesen C, et al. "Energy bandgap bowing of InAlN alloys studied by spectroscopic ellipsometry." Appl Phys Lett.;92:191907 (2008).

[82] S. Schulz, M. A. Caro, L. Tan, P. J. Parbrook, R. W. Martin, E. P. O'Reilly, " Composition-Dependent Band Gap and Band-Edge Bowing in AlInN: A Combined Theoretical and Experimental Study", Appl. Phys. Express 6, 121001 (2013).

[83] Van de Walle C. G., McCluskey M. D., Master C. P., et al. "Large and composition dependent band gap InGaN alloys", Mat. Sc. Eng. B .;59:274–278 (2009).

[84] Gorczyca I., Lepkowski S., Suski T., et al. "Influence of Indium clustering on the band structure of semiconducting ternary and quaternary alloys" . Phys. Rev.B.;80:75202 (2006).

[85] Androulidaki K, Tsagaraki E, Dimakis E, et al. " Energy gaps and bowing parameters of InAlGaN ternary and quaternary alloys", Phys. Stat. Sol. C 3 1866-1869 (2006).

[86] Bellaiche L, Mattila T, Wang LW, et al. "Resonant hole localization and anomalous optical bowing in InGaN alloys". Appl Phys Lett.;74:1842–1844 (1999).

[87] Kent P.R.C, Zunger A. "Carrier localization and the origin of luminescence in cubic InGaN alloys." Appl Phys Lett.;79:1977–1844 (2001).

[88] Moses PG, Maosheng M, Yan Q, et al. "Hybrid functional investigations of band gaps and band alignments for AlN, GaN, InN, and InGaN." J Chem Phys.;134:084703 (2011).

[89] Schulz S, Caro MA, O'Reilly EP. "Impact of cation-based localized electronic states on the conduction and valence band structure of $Al_{1-x} In_x N$ alloys". Appl Phys Lett.; 104: 172102 (2014).

[90] Schley P, Naprerala C, Goldhahn R, et al. "Band gap and effective electron mass of cubic InN." Phys Status Solidi C.;5:2342–2335 (2008).

[91] W. Paul, J. Appl. Phys. 32 Supplement," Band structure of the intermetallic semiconductors from pressure experiments", 2082 (1961)

[92] A. Breidi, A. V. Postnikov and F. El Haj Hassan. "Cinnabar and SC16 high-pressure phases of ZnSe: An ab initio study." Phys. Rev. B 81 (20), p. 205213 (2010)

[93] A.R. Goñi and K. Syassen, in Semicond. Semimet., edited by T.S. and W. Paul

(Elsevier, 1998), pp. 247–425.

[94] S. Adachi, 'GaAs, AlAs, and Al$_x$Ga$_{1-x}$As: "Material parameters for use in research and device applications", J. Appl. Phys. 58, R1 (1998).

[95] Van Camp PE, Van Doren VF, Devreese JT. "High-pressure properties of wurtzite- and rocksalt-type aluminum nitride." Phys Rev B.;44:9056–9059 (1991).

[96] Duan M, He L, Xu M, et al. "Structural, electronic, and optical properties of wurtzite and rocksalt InN under pressure". Phys Rev B.;81:33102 (2010).

[97] A Munoz, K. Kunc, " Structure and static properties of indium nitride at low and moderate pressures.", J. Phys. Condens. Matter 5, 6015-6022 (1993).

[98] C. Pryor J. Kim, L. W. Wang, A. J. Williamson, and A. Zunger "Comparison of two methods for describing the strain profiles in quantum dots" J. Appl. Phys.83, 2548 (1998).

[99] Zhongqin Yang and Zhizhong Xu "Electronic and optical properties of unstrained and strained wurtzite GaN", Phys. Rev B 15 54 (1996).

[100] W. A. Harrison. "Electronic Structure and the Properties of Solids" (Dover,1989).

[101]C. Priester , D. Bertho and C. Jouanin, "Band-offset determination at strained II-VI heterojunctions within a self-consistent tight-binding model", Physica B 191, 1-15 (1993).

[102] Sverre Froyen, Alex Zunger, and A. Mascarenhas"Polarization fields and band offsets in GaInP/GaAs and ordered/disordered GaInP superlattices" Appl. Phys. Lett. 68, 2852 (1996).

[103] R. D. King-Smith and D. Vanderbilt, Phys.Rev. B 47, 1651 (1993).

[104] Colin Wood, Debdeep Jena 'Polarization Effects in Semiconductors From Ab-Initio Theory to Device Applications' Springer (2008).

[105] Nitride Semiconductor Devices Principles and Simulation Edited by Joachim Piprek WILEY-VCH Verlag (2007).

[106] Y. Park, Carlo Floresca, Uttiya Chowdhury, Jose L. Jimenez, Cathy Lee Physical degradation of GaN HEMT devices under high drain bias reliability testing Microelectronics Reliability 49 478–483 (2009).

[107] Alessandro Chini ; Valerio Di Lecce ; Michele Esposto ; Gaudenzio Meneghesso ; Enrico Zanon Evaluation and Numerical Simulations of GaN HEMTs Electrical Degradation IEEE Electron Device Letters Vol: 30 Issue: 10

[108] F. Medjdoub ; M. Alomari ; J.-F. Carlin ; M. Gonschorek ; E. Feltin ; M. A. Py ; N. Grandjean ; E. Kohn "Barrier-Layer Scaling of InAlN/GaN HEMTs", IEEE Electron Device Letters 29 Issue: 5 (2008).

[109] Gonschorek, M.; Carlin, J.F.; Feltin, E.; Py, M.A.; Grandjean, M.:High electron mobility lattice-matched AlInN/GaN field effect transistor heterostructures. Appl. Phys. Lett., 89 (6),062106-062106 (2006).

[110] Dadgar, A. et al.: "High current AlInN/GaN field effect transistors." Phys. Stat. Sol. (A), 202 (5), 832–836 (2005).

[111] Neuburger, N. et al.: "Unstrained InAlN/GaN HEMT structure." Int. J.High Speed Electron Syst., 14 (3), 785–790 (2004).

[112] O. Ambacher,J. Smart, J. R. Shealy, N. G. Weimann, K. Chu, M. Murphy,W. J. Schaff, and L. F. Eastman "Two-dimensional electron gases induced by spontaneous and piezoelectric polarization charges in N- and Ga-face AlGaN/GaN heterostructures" J. Appl. Phys. 85, 15 (1999).

 [113] J Kuzmık "InAlN / (In)GaN high electron mobility transistors: some aspects of the quantum well heterostructure proposal", Semicond. Sci. Technol. 17 540–544 (2002).

[114] Wang M W, McCaldin J O, Swenberg J F, McGill T C and Hauenstein R J "Schottky-based band lineups for refractory semiconductors" Appl. Phys. Lett. 66 (1974).

 [115]. I. P. Smorchkova, L. Chen, T. Mates, L. Shen, S. Heikman, B. Moran, S Keller, S. P. DenBaars, J. S. Speck, and U. K. Mishra, " AlN/GaN and (Al, Ga) N/AlN/GaN two-dimensional electron gas structures grown by plasma-assisted molecular-beam epitaxy" J. Appl. Phys. 90, 5196 (2001)

 [116]. Y. Cao and D. Jena, "High-mobility window for two-dimensional electron gases at ultrathin heterojunctions" Appl. Phys. Lett. 90, 182112 (2007).

[117] M. Cardona and P. Y. Yu. "Fundamentals of Semiconductors" (Springer-Verlag, 1996).

[118] H. Ünlü, H. H. Gürel, Ö. Akinci, and M. R. Karim, "Modeling of low dimensional Semiconductors: Characterisation, Modeling and Applications", (Eds) H. Ünlü, N. J. M. Horing, Springer (2013).

[119] A. Kobayashi, O. F. Sankey, S. M. Volz, and J. D. Dow. "Semiempirical tight-binding band structures of wurtzite semiconductors AlN, CdS, CdSe, ZnS, and ZnO". Phys. Rev. B 28, 935 (1983).

[120] T. Yang, S. Nakajima, and S. Sakai. "Electronic structures of wurtzite GaN, InN and their alloy $Ga_{1-x}In_xN$ calculated by the tight-binding method." Jpn. J. Appl. Phys. 34, 5912 (1995).

[121] "Physical properties of crystals their representation by tensors and matrices" J. F. Nye, .Oxford University Press (1985)

Propriétés électroniques et structurales de $Al_{1-x}In_xN$ avec application à un composant électronique

Résumé

Le ternaire AlInN est un matériau utilisé dans les composants optiques tels que les diodes électroluminescentes, diodes lasers, fibres à réseau de Bragg ainsi que dans des composants électroniques tel que les HEMT. Il se présente sous deux phases, wurtzite et zincblende, on se propose alors, dans ce travail, en premier lieu de comparer les propriétés structurales et électroniques des deux phases. Cette comparaison serait bénéfique pour le choix de la phase la plus appropriée pour un composant donné.

L'AlInN se présente généralement sous forme d'hétérostructure AlInN/GaN dans les composants électroniques. Sa croissance sur la couche GaN entraine l'apparition de contraintes élastiques résultant en de profonds changements dans ses propriétés structurales et électroniques. La deuxième partie de cette thèse concernera l'étude de l'effet physique de ces contraintes.

Et finalement après un bref rappel sur l'architecture et sur la physique d'un transistor HEMT, on essaiera d'appliquer les concepts précédents aux effets sur les principaux paramètres régissant le fonctionnement de ce composant.

Deux méthodes de calcul ont été utilisées pour les études théoriques :   la première semi empirique la tight binding, et l'autre la théorie de la fonctionnelle de la densité une méthode ab-initio. Un aperçu théorique sur ces deux méthodes ainsi que les paramètres de calcul utilisés sont exposés.

Mots clés: Nitrures, LCAO, théorie de la densité fonctionnelle, propriétés électroniques et structurales.

ئص الإلكترونية و الهيكلية لـ $Al_{1-x}In_xN$ مع التطبيق

الثلاثيوAlInN هو من المواد المستخدمة في المكونات البصرية مثل الثنائيات الباعثة للضوء، الثنائيات الليزر والألياف براج مقضب وكذلك في المكونات الإلكترونية مثل HEMTs. تكون هذه السبيكة في بنيتين، wurtziteوzincblende، يقترح في هذا العمل، أولا لمقارنة الخصائص الهيكلية والإلكترونية للمرحلتين. ان هذه المقارنة تكون مفيدة لاختيار أنسب بنية لمكون معين.

نجد AlInN عموما في شكل AlInN/GaN في المكونات الإلكترونية. نموها على طبقة الجاليوم يتسبب في ظهور ضغوط مرنة مما أدى إلى إحداث تغييرات عميقة في الخصائص الهيكلية والإلكترونية لها. أما الجزء الثاني من هذا العمل ينطوي على دراسة تأثير مادي من هذه القيود.

وأخيرا بعد تقديم موجز عن الهندسة والفيزياء للترانزيستور HEMT،نحاول تطبيق المفاهيم المذكورة أعلاه إلى الآثار المترتبة على المعالم الرئيسية التي تحكم عمل هذا العنصر.

وقد استخدمت طريقتين حساب للدراسات النظرية: أولا الطريقة النصف التجريبية tight binding، و الثانية هي النظرية الوظيفية للكثافة. نعرض لمحة نظرية لهذه الأساليب وكذلك معاملات الحساب المستخدمة.

الكلمات المفتحية: نيتريد النظرية الوظيفية للكثافة، الخصائص الهيكلية والإلكترونية نظرية الربط القوي.

Abstract

The ternary AlInN is a material used in optical components such as light emitting diodes, laser diodes, fiber Bragg grating as well as in electronic components such as HEMTs. It comes in two phases, wurtzite and zinc blende, it is proposed then, in this work, first to compare the structural and electronic properties of the two phases. This comparison would be beneficial to choose the most appropriate phase for a given component. Furthermore we will try to study high pressure effects on the structural and electronic properties of AlInN and its phase transformation into the rocksalt phase.

The AlInN comes generally in the form of heterostructure AlInN/GaN in electronic components. Its growth on the GaN layer causes the appearance of elastic stresses resulting in profound changes in its structural and electronic properties. The second part of this work will involve the study of the physical effect of these constraints.

And finally after a brief introduction on architecture and on the physics of a HEMT, one will attempt to apply the above concepts to the effects on the main parameters governing the operation of this component.

Two calculation methods have been used for theoretical studies: the first semi empirical tight binding method, and the second ab-initio the density functional theory. A theoretical overview of these methods is exposed as well as the calculation parameters used.

Key words: Nitrides alloys, tight binding, density functional theory, electronic and structural properties.